Quadrotor Flight Performance

A thesis submitted to the University of Manchester for the degree of

Doctor of Philosophy

in the Faculty of Engineering and Physical Sciences

2011

David Sebastian Langkamp

School of Mechanical, Aerospace and Civil Engineering

Table of Contents

Final word count including all lists, tables and appendices 47300

List of Figures

List of Tables

9

Nomenclature

A	Amplitude of high angle of attack lift model sine function [-]
a'	Rotational interference factor [-]
a_0	Coning angle (flapping) [rad]
a_1	Longitudinal flapping angle [rad]
A_{disk}	Disk area [m^2]
b_1	Lateral flapping angle [rad]
c	Local chord length [m]
C_{Fx}, C_{Fy}	Rotor drag and side force coefficient [-]
C_l, C_d	Local element lift and drag coefficient [-]
$C_{l\alpha}$	2d lift curve slope [-]
C_{Mx}, C_{My}	Rotor rolling and pitching moment coefficient [-]
c_o, c_n	Mangler-Squire model coefficient [-]
C_T, C_Q, C_P	Rotor thrust, torque, power coefficients [-]
D	Drag [N]
d	Distance from one rotor hub to the adjacent rotor hub [m]
D	Steady offset of the high angle of attack drag model [-]
dA	Area swept out by blade element [m^2]
E	Amplitude of high angle of attack drag model cosine function [-]
E	Young's Modulus [N/m^2]
e_{eqv}	Non-dimensional equivalent flapping hinge offset [-]
f_x, f_y, f_z	Incremental forces on blade element [N]
i	Auxiliary current term in motor model [A]
i_0	Motor no load current [A]
I_b	Total battery load current [A]
I_x	Second moment of area about the blades neutral bending axis [m^4]
I_β	Equivalent blade inertia [kg*m^2]
K	Number of azimuthwise steps [-]
kCF_x, kCF_z	Fuselage model amplitudes for sine and cosine waves [-]
k_{eqv}	Equivalent structural flapping stiffness at equivalent hinge offset [Nm/rad]
Kv	Motor speed constant [rpm/V]
k_x, k_y	Inflow coefficients [-]
k_β	Combined centrifugal and structural flapping stiffness [Nm/rad]
l	Distance from CG (central axis) to the rotor centre [m]
L	Length scale [-]
M	Number of radial elements [-]
$\dot{m}$	Mass flow through the control volume [kg/s]
M_A	Aerodynamic moment term in the flapping equations [Nm]
P	Power [W]
P_{elec}	Electrical Power [W]
P_{mech}, P_{shaft}	Mechanical Power [W]
r	Non-dimensional radius [-]
R	Internal motor resistance [Ω]
R_b	Approximate internal resistance of the battery at design load [Ω]
Re	Reynolds number [-]
R_{max}	Rotor radius [m]
u	Radial swirl velocity [m/s]

U	Total resultant velocity vector onto the blade element [m/s]
U_p	Perpendicular velocity component on the blade element [m/s]
U_r	Radial velocity component on the blade element [m/s]
U_t	Tangential velocity component onto the blade element [m/s]
U_t, U_p, U_r	Local blade element velocities [m/s]
V	Velocity vector onto the disk [m/s]
v	Auxiliary voltage term in motor model [V]
V, V_x, V_z	Free stream, in plane, out of plane velocity [m/s]
$v_i(r)$	Induced velocity [m/s]
V_x	X component of velocity vector onto disk [m/s]
V_z	Z component of the velocity vector, positive if in climb [m/s]
W	Weight [kg]
w	Velocity in the far wake of the momentum theory control volume [m/s]
w	Weighing factor in the SOR scheme [-]
w_1, w_2	Mangler-Squire model weighting coefficients [-]
y	Dimensional term for the radius of the local blade element [m]
α_{shaft}	Shaft angle with with respect to vehicle body coordinate system [rad]
$\alpha_{vehicle}$	Vehicle angle of attack (positive is nose up) [rad]
β	Flapping angle [rad]
γ	Blade Lock number [-]
θ	Vehicle pitch angle [rad]
θ_0	Total blade pitch at ¾ radius [rad]
$\lambda_i(r)$	Non-dimensional induced velocity [-]
λ_β	Flapping frequency ratio [-]
$\lambda_{\beta 0}$	Non-dimensional non-rotating frequency of the blade [-]
μ	Dynamic viscosity [N*s/m^2]
μ_x	Horizontal advance ratio [-]
μ_z	Vertical advance ratio (climb/descent) [-]
ρ	Density (of air) [kg/m^3]
σ	Rotor solidity [-]
ϕ	Vehicle roll angle [rad]
X	Wake skew angle [rad]
ψ	Vehicle yaw angle [rad]
Ω	Rotor rotational speed [rad/s]
ω, Ω	Rotational speed of the rotor [rad/s]
ω_{no}	Non-rotating frequency of the blade [rad/s]
ω_β	Natural flapping frequency in vacuo [rad/s]
F	Tip loss factor [-]
P	Rotor power [W]
Q	Rotor torque [Nm]
T	Rotor thrust [N]
dL, dD	Incremental drag on local element [N]
x, y, z	Blade element coordinates on disk [m]
α	Local blade element angle of attack [rad]
θ	Local blade element pitch angle [rad]
ψ	Azimuth angle on rotor disk [rad]
ϕ	Local blade element inflow angle [rad]

Subscripts

body	In body axes
cg	About the cg
earth	In earth axes
hub	In hub (disk) axes
j	Placeholder for axes x,y,z
k	Number of the current iteration step

Abbreviations

BEMT	Blade Element Momentum Theory
BET	Blade Element Theory
CFD	Computational Fluid Dynamics
CG	Centre of Gravity
CP	Centre of Pressure
DAQ	Data Acquisition
DoF	Degree of Freedom
ESC	Electronic Speed Controller (for Brushless motors)
EVP	Electric Variable Pitch
ISA	International Standard Atmosphere
MAV	Micro Air Vehicle, defined as being a man-portable UAV
MTOW	Maximum Takeoff Weight
PWM	Pulse Width Modulation (Signal)
Re	Reynolds Number
rpm	Rotations per Minute
SL	Sea Level
SOR	Successive Overrelaxation Method
TPP	Tip Path Plane
UAV	Unmanned Aerial Vehicle

Abstract

ABSTRACT OF THESIS submitted by **David Sebastian Langkamp** for the Degree of Doctor of Philosophy and entitled "**Quadrotor Flight Performance**" (Submitted October 2011)

The aim of this thesis is to develop improved understanding of the effects of configuration choice on the forward flight performance of quadrotors, in particular on endurance and maximum flight speed. Configuration choices include rotor arrangement, fixed vs. variable pitch rotors and fuselage geometry. The work is distinct from previous research on large-scale helicopters not only in the rotor arrangement and fuselage geometry, but also because of area-volume scaling laws, lower Reynolds numbers causing a stronger CL/CD variation along the blade radius, trim without cyclic control and variable-speed electric propulsion.

A numerical blade element method using nonlinear aerodynamic models was developed to provide the six components of hub forces/moments for any level flight condition of practical interest. A novel numerical method is presented to stabilise the blade element iteration schemes. A hingeless flapping model is included and several induced velocity models are compared. Wind-tunnel experiments on isolated fixed-pitch and variable-pitch rotors at a broad range of operating conditions were conducted as validation cases. It was found that a local-differential blade element momentum method could provide an acceptable and robust low-order solution over a large range of practical flight conditions.

A simulation model for trimmed level flight was created by combining a semi-empirical fuselage aerodynamic model with the blade element code and a first order electric motor model. Design methods to improve endurance and maximum flight were evaluated through a number of configuration design case studies. Wind tunnel experiments were conducted to measure the aerodynamics of two different fuselages and rotor-rotor interference as a function of spacing and flight speed. A novel closed-loop trim experiment in the wind tunnel was shown to be an effective method to obtain quadrotor forward flight power and trim curves in a controlled environment.

Results show that current quadrotors require large negative vehicle angles of attack for forward flight trim which causes a steep rise in power demand and limits forward flight speed. This is largely driven by the fuselage drag and downforce, which are widely ignored in quadrotor literature. There is also a trim limit due to rear rotor saturation that restricts maximum flight speed and efficiency. This arises due to the need to compensate the strong nose-up pitching moment from the hingeless rotors. Rotor-rotor interference appears to be similar in nature to tandem rotors, but effects for typical rotor spacings are small and mainly fall within the noise of the force measurements.

The design case studies show that the use of collective pitch on quadrotors brings power benefits over a wide range of velocities if both collective and rotor speed are adjusted. However, if approximate mass penalties are taken into account net power benefits could only be shown for speeds above 80% of the top-speed. It is shown that a design optimised for forward flight should be in an x-arrangement to maximise pitch/roll control authority. Teetering rotors and a rearrangement of the vertical centres of gravity and pressure were found to be effective at reducing the net pitching moment and thereby increasing maximum speed in the order of 5-10%. A rotor shaft angle with respect to the fuselage can be used to align the fuselage to practical high speed angles of attack, minimise fuselage forces and reduce forward flight power by up to 20%, depending on the fuselage design.

Declaration

No portion of the work referred to in the thesis has been submitted in support of an application for another degree or qualification of this or any other university or other institute of learning.

David Sebastian Langkamp, October 2011

Copyright Statement

The author of this thesis (including any appendices and/or schedules to this thesis) owns certain copyright or related rights in it (the "Copyright") and he has given The University of Manchester certain rights to use such Copyright, including for administrative purposes.

Copies of this thesis, either in full or in extracts and whether in hard or electronic copy, may be made only in accordance with the Copyright, Designs and Patents Act 1988 (as amended) and regulations issued under it or, where appropriate, in accordance with licensing agreements which the University has from time to time. This page must form part of any such copies made.

The ownership of certain Copyright, patents, designs, trade marks and other intellectual property (the "Intellectual Property") and any reproductions of copyright works in the thesis, for example graphs and tables ("Reproductions"), which may be described in this thesis, may not be owned by the author and may be owned by third parties. Such Intellectual Property and Reproductions cannot and must not be made available for use without the prior written permission of the owner(s) of the relevant Intellectual Property and/or Reproductions.

Further information on the conditions under which disclosure, publication and commercialisation of this thesis, the Copyright and any Intellectual Property and/or Reproductions described in it may take place is available in the University IP Policy (see

http://www.campus.manchester.ac.uk/medialibrary/policies/intellectual-property.pdf), in any relevant Thesis restriction declarations deposited in the University Library, The University Library's regulations (see http://www.manchester.ac.uk/library/aboutus/regulations) and in The University's policy on presentation of Theses.

Acknowledgements

Throughout the years I've always enjoyed my time in Manchester. There are so many people who I'd like to thank for making my life here so special and supporting me along my way. I would like to start by thanking Bill Crowther, my supervisor, for his guidance and thoughtful feedback on my work, and BAE Systems and everyone at the School of MACE for giving me the great opportunity to do this research.

I would have never made it this far without the support from my lovely lady Sarah, who sadly has not seen much of me in the past months, and my family, in particular my parents Linda and Herbert and my grandma Elfriede, who has been following my steps throughout my journey.

I deeply owe Matt Pilmoor, Ian Lunnon, Phil Geoghegan, Andrew Kennaugh, Chris Harley and Neel Shah for their support with my experimental work and their incredible patience. I'd also like to thank Peter Hollingsworth for his insights into the world of Aerospace and Gareth Roberts for his support with the final round of wind tunnel experiments and the joy of co-chairing the unofficial paper plane competition at IMAV 2011. A very big "thank you" goes to Ben, Hossain and Jonny for proofreading large parts of this thesis and to Martin Turner who co-supervised my work.

My life in Manchester wouldn't have been the same without all the other great friends I've made here, like John and Jonny, Gareth, Fazreena and Nalleli, just to name a few. I'll miss contemplating research with Andrew and discussing the depths of the blade element method, inflow and life with Ben, the best office-mate ever.

Thank you for the best time of my life,

David

Chapter 1: Introduction

1.1 Motivation

There is demand for small unmanned aerial vehicles (UAVs) for short-range surveillance tasks in urban environments [1]. This demand is often well matched by rotorcraft vehicles that do not require a minimum flight speed and can hence operate in confined spaces. A type of rotorcraft design that has received considerable research interest over the past decade are quadrotor vehicles which are mechanically simple and lend themselves to automatic control. Up to now the study of quadrotor flight has been primarily considered as a control problem for near hover operations, whereas little analytical and experimental work on forward flight performance has been presented. Many open questions remain on how to model and design quadrotors in forward flight. This thesis aims at improving the understanding of forward flight which is critical to extend the useful endurance and maximum flight speed of quadrotors.

1.2 Distinctive features of quadrotors

After decades of active research into helicopters an extensive body of literature exists and it is important to point out why this work on quadrotors is different from previous work on full-scale single main rotor helicopters. Three key areas of differences are highlighted: the trim mechanism, scaling laws and the effects of electric propulsion.

1.2.1 Implications of the quadrotor trim mechanism

Typical quadrotor designs have got two pairs of clockwise and anti-clockwise rotors and are controlled by varying the rotational speed of the individually fixed-pitch rotors. The differential thrust and torque on the rotors provides control in pitch, roll, yaw and z-force without the need for a swashplate. Translational accelerations can be achieved indirectly through a change in body attitude and total thrust magnitude.

The lack of cyclic control is a key difference compared to conventional helicopters. In the absence of cyclic control a single rotor can only be trimmed for its thrust and reaction torque. Any other hub forces and moments arising in forward flight cannot be compensated on a rotor level. The individual rotor is hence "untrimmed" because it gives rise to undesired forces and moment. This leads to a very different operating environment from conventional helicopter rotors and hence previous data on trimmed helicopter rotors does not necessarily apply to this research.

1.2.2 Size matters: the effects of volumetric scaling laws and Reynolds number

Quadrotors typically weigh a few kilograms. This makes them several orders of magnitude smaller than conventional manned helicopters and scaling effects have to be considered in a flight performance analysis. For the purpose of this work the effects of scaling laws can be roughly broken down into Reynolds number effects and area-volume scaling.

The rotor blades of a quadrotor in the 1 kg class typically operate at Reynolds numbers of around 100000. The lower Reynolds numbers compared to full scale helicopters not only reduce the aerodynamic efficiency, but also lead to a stronger lift and drag coefficient variation with changes in Reynolds number along the blade radius. This implies that Reynolds number based lift and drag models should be used in the analysis of quadrotors.

An effect observed when comparing helicopters of different scales is that gross weight grows faster than the rotor size ([2], p283). This can be explained by the well known square-cube law: If the reference length L for geometrically similar vehicles is increased, the volume and hence mass increase proportionally with L^3, whereas areas only increase with L^2. Assuming a constant density, a constant drag coefficient and ignoring further Reynolds number effects, this means smaller vehicles have a higher drag to weight ratio for a given airspeed compared

to larger vehicles. This is documented in the helicopter literature ([2], p307) and has three main implications for the current work:

- A fuselage drag model has increasing importance for small vehicles.

- Large drag/weight ratios require large vehicle angles of attack for forward flight trim, hence small angle approximations in the rotor angle of attack model are unsuitable.

- For a given power/weight ratio, the maximum vehicle speed reduces with vehicle size.

1.2.3 The effects of electric propulsion

Traditional helicopter literature mainly considers gas turbine engines which operate at constant rotational speed and lead to a reduction in aircraft mass with mission duration due to fuel burn. With electric propulsion, a wider operational range of rpm is feasible and the power-plant efficiency has to be monitored as a function of rotational speed, torque and motor design. Variable-speed operation implies that some conventional ways of non-dimensionalising data, such as advance ratios which normalise the flight speed against the rotor tip speed, are not necessarily practical. Flapping frequency formulations which are expressed with respect to the rotor rotational frequency need careful reformulation to capture rpm changes.

A further minor aspect is that the maximum available battery power decreases with flight time which could have a negative impact on the flight envelope as a mission progresses.

1.3 Aim of this work and thesis structure

1.3.1 Aim of this work

The aim of this thesis is to develop an improved understanding of the effects of configuration choice and operational strategy on the forward flight performance of quadrotors, in particular on endurance and maximum flight speed. Configuration choices include rotor

arrangement, fixed vs. variable pitch rotors and fuselage geometry. The operational strategy includes the choice of airspeed and the combination of collective pitch and variable rpm.

To understand quadrotor forward flight performance requires an understanding of rotor performance, rotor-rotor interference, fuselage aerodynamics and forward flight trim. These aspects will be studied through the development of low order rotor and vehicle models and through wind tunnel experiment.

1.3.2 Objectives and thesis outline

The objectives of this work are broken down by Chapter:

Chapter 2: *To review the state of the art in quadrotor modelling, design and flight performance.*

Chapter 3: *Combine, adapt and apply well know rotor aerodynamics and electric models to quadrotors in hover and forward flight and to introduce a simple method to stabilise the iteration process of a numerical blade element model.*

Chapter 4: *Obtain repeatable and accurate time-averaged, steady state measurement data on the hover and forward flight performance of electric-driven small scale rotors and quadrotor vehicles. To document a method for quadrotor forward flight trim and interference analysis as well as the creation of a dataset on quadrotor body drag and variable pitch/variable rpm rotor performance.*

Chapter 5: *Understand the forces and moments created by a single hingeless, variable-speed, variable-pitch quadrotor rotor in hover, climb and forward flight and to evaluate the performance of the proposed simulation model using wind-tunnel data.*

Chapter 6: *Understand the limits to the flight performance of current quadrotors and investigate ways to reduce forward flight power requirements and extend the maximum flight*

speed through configuration design changes and the introduction of collective pitch capabilities.

1.3.3 Scope and limitations

The focus of this work is on low order models that can capture the key characteristics required for the study of quadrotor forward flight performance. The limitation is made that only steady-state conditions are discussed. Furthermore no contribution is made to quadrotor control, dynamic response or the optimization of quadrotor rotor blades.

1.4 Contributions

1.4.1 Contributions

The main contributions of this thesis are:

1. It presents low-order simulation methods and experimental methods suitable for the study of quadrotor forward flight performance. In particular it presents a numerical blade element method with a novel multi-step iteration scheme and an experimental method to rapidly obtain quadrotor trim and power curves through closed-loop force sensor feedback.

2. It presents unique experimental datasets useful for further research on quadrotor dynamics and performance. In particular it presents data on the aerodynamics of small, hingeless, variable-pitch/variable-rpm rotors in hover and forward flight. Furthermore, it presents experimental data on quadrotor airframe aerodynamics and rotor-rotor interference which were not available previously.

3. It analyses the performance of current quadrotors, establishes the limits to their flight performance and analyses the effects of configuration design on the forward flight performance. Design choices are discussed that can help to reduce forward flight power demands and increase maximum flight speed.

21

4. It evaluates the introduction of variable pitch rotors on quadrotor vehicles from a flight performance perspective and presents a balanced analysis of power benefits vs. increases in system mass.

1.4.2 Published papers

During the course of this PhD research contributions to the following papers were made:

- Langkamp, D., Crowther W.J*., A low order rotor aerodynamics model for UAVs in wind*, in 2010 RAeS Aerodynamics Conference - Applied Aerodynamics: Capabilities and Future Requirements. 2010, RAeS: Bristol.

- Langkamp, D., Crowther W.J., *The role of collective pitch in multi rotor UAV aerodynamics*, in 36th European Rotorcraft Forum. 2010: Paris.

- Langkamp, D., Crowther W.J., *Simulation methods for MAVs in Urban Operations*, in 4th International UAV World Conference 2010: Frankfurt.

- Langkamp, D., Roberts, G. , Scillitoe, A. , Lunnon, I., Llopis-Pascual, A., Zamecnik, J., Proctor, S., Rodriguez-Frias, M., Turner, M. , Lanzon, A. and Crowther, W.J, *An engineering development of a novel hexrotor vehicle for 3D applications*, IMAV 2011: t'Harde Netherlands.

- Crowther, W.J., Lanzon, A., Maya-Gonzalez, M., Langkamp, D., *Kinematic Analysis and Control Design for a Non Planar Multirotor Vehicle*, Journal of Guidance, Control, and Dynamics vol.34 no.4 (1157-1171), 2011.

Chapter 2: State of the Art

The objectives of this Chapter are:

To review the state of the art in quadrotor modelling, design and quadrotor flight performance. To present an overview of performance data for current quadrotor designs.

2.1 Scope and limitations of the literature review

The focus of this literature review is on the design, modelling and performance aspects of quadrotor UAVs. The fields of control and autonomy are therefore not further considered and the reader is referred to work by Hoffmann [3], Cowling [4] and Bresciani [5] for a comprehensive overview of quadrotor autonomy and control strategies.

There is an extensive body of excellent literature on rotorcraft aerodynamics and performance [2, 6-12]. These sources were used and referenced for some modelling and experimental strategies, but are not further discussed in this literature review. Furthermore literature specific to some modelling and experimental aspects, for example inflow modelling and wind tunnel correction procedures, will be discussed in the theory and experimental methods sections and therefore is not included in this literature review.

2.2 Previous work on quadrotor design and modelling

2.2.1 The evolution of modern quadrotor UAVs

At the beginning of the last century there were initial attempts to build a manned quadrotor, like the Oehmichen quadrotor in 1921, which were later abandoned with the advent of single main rotor designs. It was not until the 1990s that advances in micro-electronics and battery technology provided the enabling technologies for the design of small unmanned quadrotor vehicles around radio-controlled toys, like the predecessors of the early

"Draganflyer" quadrotors. An early project on quadrotor UAVs was the 1999-2001 "Mesicopter" project [13] at Stanford aiming to design a quadrotor at a centimetre scale. Due to limitations with miniaturization the project never achieved untethered flight. For an excellent review of the historic evolution of quadrotor UAVs the reader is referred to work by Pounds [14].

Most modern quadrotor UAVs have a very similar configuration based on four electric motors with variable-speed rotors. A wide range of university, commercial and hobbyist quadrotors based on this design have been built and only key research relevant to this study is presented in this review.

2.2.2 Defining the importance of hingeless flapping

At Stanford University, Hoffmann et al published work [3, 15, 16] on the STARMAC quadrotor, which is based on the commercial off the shelf "Draganflyer" vehicle. Their work on quadrotor flight dynamics [16] claims that previous simple analytical models are inadequate for control at forward flight. They present a basic momentum theory model from helicopter literature to relate forward flight thrust and disk angle of attack assuming constant power. Axial descent cases are modelled with a standard semi-empirical model for the induced velocity in the vortex ring state. For simple experiments the rotor was mounted on a test rig and a free stream velocity was applied with an open fan whilst thrust and torque were measured. The trend of the experimental thrust for axial climb was shown to agree with momentum theory, although no direct comparison of like-for-like data is presented. No comprehensive data on forces in forward flight is presented, but the importance of flapping is shown using the horizontal hub forces. The paper applies Newman's hingeless flapping model [11] and demonstrates its suitability for typical quadrotor rotors. The flapping frequency ratio is estimated using an effective hinge offset and by treating the blade as a torsional spring. The stiffness of the blade is estimated by measuring the tip deflection to an applied tip load.

In another paper [17] the Stanford group describes destabilizing interaction effects between the rotors and a loss of thrust in descent. This is a clear indication of the influence of the vortex ring state but detailed flight test data and performance data is not presented.

Overall, the aerodynamic modelling of the STARMAC appears overly simplified for a broad flight performance analysis, since it does not represent effects of the physical blade geometry nor any induced or profile losses. Furthermore, it does not consider any side forces or rolling and pitching moments at the hub, fuselage aerodynamics or rotor-rotor interference effects.

2.2.3 An analytical blade element simulation

Bouabdallah and Siegwart [18, 19] presented work on the modelling and design of the "OS4", a 0.5 kg custom quadrotor designed for maximum hover endurance and a 100 % thrust margin. The aerodynamic model is based on a simple analytical solution of the blade element momentum theory (BEMT) in forward flight that was taken from unpublished work on the Stanford Mesicopter project [20]. This BEMT solution considers the 6-DoF forces and moments on the rotor disk and employs linear aerodynamics in the form of a constant lift curve slope, which does not capture any stall effects on the blade elements. Gyroscopic effects on the rotor are considered but the inflow modelling is unclear and no provisions seem to have been made for flapping or the variation of inflow in forward flight. By using an analytical solution the effects of a reversed flow are also ignored. Furthermore, body drag and rotor-rotor interference are ignored and no forward flight power and trim results are presented.

2.2.4 An improved analytical blade element simulation

One of the most comprehensive analyses of quadrotor aerodynamics up to date has been presented by Martinez's [21] work on the flight dynamics of a Draganflyer Xpro quadrotor. Martinez presents single rotor wind tunnel testing and derives an analytical solution to the BEMT in forward flight. The vortex ring state and induced velocity variation with flight speed are modelled with a simple uniform induced velocity function based on semi-empirical data

25

and momentum theory. Flapping is modelled using standard literature solutions for hingeless flapping. Martinez's work presents a noticeable improvement compared to previous work in the field, however the nature of the analytical model implies some important simplifications. The geometry of the blades is modelled as constant twist and constant chord, a linear lift curve slope is applied and no provisions are made for stall, Reynolds number effects, the reverse flow region or the inflow distribution in forward flight. Furthermore, no iterations are performed to ensure a better correlation between mean induced velocity and rotor thrust. Airframe aerodynamics are ignored based on the absence of experimental data in the literature. No forward flight power and trim results are presented.

2.2.5 The importance of CG and the choice of flapping mechanism

Pounds [9, 22, 23] studied the enabling technologies necessary for quadrotors over 2 kg, which he defined as sufficiently large to carry payloads for "practical commercial applications". His work presents the design of avionics, airframe and rotors. Pounds [9, 23] presents a holistic design approach for a fixed-pitch small scale rotor that is based on a balance of aerodynamic performance, rigidity and manufacturability. He makes an important contribution by recognizing the importance of the relative CG-rotor plane positioning and flapping hinge design: whilst most quadrotor designs use hingeless rotors, his X-4 uses teetering rotors to improve the vehicle dynamics in forward flight. He also claims that aligning the rotor planes close to the horizontal plane of the centre of mass "produces favorable dynamic behaviour". This thesis will show that both arguments are also beneficial for forward flight performance.

Another key aspect raised by Pounds are the rotor dynamics associated with heavier rotor blades. Pounds was the first author to explicitly mention scaling issues with variable speed rotor operations. He argues that as rotors become heavier their inertia, and hence control delays associated with variable speed operations, increase. He was the first author to mention

26

collective pitch rotors as a possible solution to this problem, but decides against using them because of increased mechanical complexity.

As with all previous quadrotor work, body drag, rotor-rotor interference and forward flight power and trim curves are not considered by Pounds.

2.2.6 A contribution to electric subsystem modelling

Stepaniak [24, 25] presents the design of a large 12 kg quadrotor vehicle designed primarily from off-the-shelf components. Driven by the need for a high payload platform to carry a LIDAR sensor, he developed a quadrotor capable of carrying a payload of about 5 kg – the largest unmanned quadrotor that has successfully flown without tethers to date. Stepaniak focuses on the vehicle design and subsystem modelling rather than control. The key contributions of his work are that he is considering brushless motor, speed controller and basic battery characteristics [26] in the simulation model. By including these subsystem models he is accounting for several sources of efficiency losses and presents a graphical method for determining endurance in hover. Key conclusions from the subsystem modelling are that first order motor losses and battery pack power dissipation had a significant effect on endurance, whilst higher order brushless motor models for rotational losses presented no significant modelling advantages under typical operating conditions.

Like much of the previous work his modelling is based around hover conditions and does not take into account any effects from forward flight on vehicle performance and endurance. The key influence his work has on this thesis lies in the selection and validation of suitable subsystem models for brushless motors and battery systems.

2.2.7 Further low order modelling work on quadrotors

Sudiyanto et al. [27] present work on the first principles modelling of quadrotors and use a simple analytical blade element method without any flapping model. They include a rudimentary fuselage model based on the effective wetted area in every axis, but no assumption or validations are presented on how this wetted area is obtained. An analytical derivation of stability derivatives is presented, but no validation data is presented and it remains open how well the highly simplified model captures forward flight behaviour.

Bristaeu [28] analyses "the Role of Propeller Aerodynamics in the Model of a Quadrotor UAV". The work uses an analytical blade element model for thrust, torque and rotor drag force and is based on the assumption of constant local angle of attack and uniform inflow. No provisions of the changing inflow in forward flight are made and no validation against experimental rotor data is made. In line with the current state of the art rotor flapping is included in the simulation. The paper furthermore highlights that there is still considerable ambiguity on basic quadrotor design parameters, like CG position. It is claimed that a CG below the rotor plane was beneficial for longitudinal stability, but a CG above the rotor plane was beneficial for better disturbance rejection by preventing the vehicle to follow the direction of the gust.

2.2.8 Performance limits of quadrotors

Work by Berry [29] studies quadrotor path planning and includes quadrotor "performance limits", defined as maximum speeds and accelerations. It is not shown how these limits were obtained and no experimental validation is presented.

2.2.9 Unusual configurations and variable pitch quadrotors

The standard configuration for most quadrotors is based on four electric motors with fixed-pitch rotors. An exception to this "standard" configuration is work by Bluteau et al. [30], who designed a quadrotor based on a single four stroke engine with the aim of increasing

endurance compared to electric quadrotors. The design of the vehicle and the variable speed transmission is presented but no experimental data, rotor/motor performance results or flight tests are reported.

Very recent work by Cutler at MIT (August 2011) [31] demonstrates the design of a variable pitch quadrotor with the motivation to increase quadrotor manoeuvrability. The propulsion system design is similar to the experimental setup used in the current research and the setup on the Manchester variable pitch Hexrotor project [32]. Four brushless AXI "electric variable pitch units" are used. A pitch linkage rod is actuated using an RC servo and driven, through the hollow main rotor shaft, by a pitch actuation mechanism. Simulations on rotor thrust response and vehicle response near hover are presented and no further forward flight simulations are included. Quadrotor roll response experiments are presented for a single-degree of freedom quadrotor test rig but no single rotor experiments for variable pitch/rpm are included. It is concluded that variable pitch makes little difference to "non-agile manoeuvres", but is worth the mass and complexity penalties for agile manoeuvres because it can expand control bandwidth and the "envelope of attainable agile manoeuvres".

Whilst the work by Cutler is the first modern quadrotor UAV to be documented in the literature, it is worth mentioning early unpublished work on the Hoverbot project [33] from 1992. This work followed a similar strategy of having four variable speed/variable pitch rotors but the vehicle never achieved untethered flight and no further progress on the project has been published.

2.2.10 Simple endurance models

Roberts et al. [34] address the issue of quadrotor endurance for a conventional fixed-pitch quadrotor. A simple endurance estimation method based on mass fractions, battery energy density and an experimental thrust to power curve is presented. The method is only valid for hover and does not include any forward flight effects. A ceiling attachment strategy is

introduced to improve the time at station whilst in "perch and stare" mode, but no further strategies to improve endurance are presented.

2.3 Relevant work on miniature rotorcraft modelling and testing

Small scale rotors are known to have a reduced efficiency compared to large scale rotors [2]. This problem is not unique to quadrotors and this section reviews other work relevant to the modelling and experiments outside the field of quadrotor research.

2.3.1 Classical work on model rotors

First a selection of classical work at NACA and NASA on model scale rotors is reviewed, in particular the work by Althoff et al. [35], Caradonna et al. [36] and Meyers et al. [37].

Althoff and Noonan [35] conducted hover tests on a rotor with 0.82 m radius for which a maximum Figure of Merit of 0.75 was obtained. The rotor is significantly larger than current quadrotor rotors and operates at a different Reynolds number range than quadrotor rotors. Furthermore the data is not presented against collective pitch and therefore cannot be used as a comparison case.

Caradonna et al. [36] conducted hover tests and hot wire measurements on a rotor with a 1.15 m radius. The work was aimed at surveying the tip vortices and presents detailed data on the chordwise pressure variation but unfortunately no global thrust and torque correlations against collective pitch and rpm are presented.

Meyers et al. [37] presents work on a 1.52 m (5 ft) diameter rotor with and without hinge offset. Chord and spanwise pressure distributions are presented for hover and forward flight at a single disk angle and advance ratios above 0.22. However, no breakdown of the 3-DoF hub forces and moments is given.

Based on the above cases it becomes apparent that work on model scale rotors is not representative of quadrotor rotors in terms of scale and Reynolds numbers. Furthermore there is a lack of a relevant comprehensive dataset in terms of forward flight speeds, disk angles, collective pitch and rpm variations.

2.3.2 Optimisation of small rotors for hover

Several attempts have been made to optimize the rotor design for small rotorcraft vehicles, most notably by Bohorquez [38] who worked on coaxial helicopter UAVs. He argues that at the scale of micro air vehicles viscous effects become dominant and conventional airfoils and rotor configurations offer a poor rotor performance. His work aims to explore rotor design effects on the hover performance of small-scale rotors of about 0.11 m radius. He presents the design of a computerised hover test-stand for single and coaxial rotors and carries out an extensive parametric study of the blade geometry at different collective pitch and rotational speed settings. The study included circular arc and NACA 0012 airfoils used in rectangular and tapered blades. The highest figure of merit of 0.65 was measured for rotors using thin curved plate airfoils of 6% and 9% camber and a 2:1 linear taper. Bohorquez furthermore presents a thorough hover blade element momentum theory approach, which addresses the issue of low Reynolds number lift and drag modelling using 2D CFD data. Furthermore, a novel inverse method to approximate 2D airfoil characteristics from rotor tests is presented and some of Bohorquez NACA 0012 results are considered in Chapter 3.3.2.5 of this thesis.

Young et al. [39] assessed the hover performance of low Reynolds numbers using experiments on a range of commercial off the shelf circular-arc rotor blades from around 0.22-0.29 m radius. The maximum figure of merit measured was 0.53 and no significant differences in maximum figure of merit were observed for tapered and rectangular blades.

2.3.2 Comparison of modelling methods from coaxial helicopters

At ETH Zurich, the design and hover performance of small coaxial helicopters of about 0.06 m rotor radius was studied by Bermes [40] and Schafroth [41]. Bermes' [40] contribution relevant to the current work is that he analysed the sensitivity of the hingeless rotor steering moment to blade stiffness and confirmed that steering moments were dominated by the stiffness effects. Schafroth's [41] contribution relevant to the current work is that he compared hover thrust and power results from a collective-pitch test-rig against three different modelling methods: Blade element momentum theory, vortex theory and higher order commercial CFD solutions. No noticeable improvement in thrust and torque predictions could be achieved using vortex theory or CFD as opposed to the blade element momentum theory model.

2.4 An overview of current quadrotor performance

Detailed technical performance data from manufacturers is difficult to obtain and marketing material does not follow universal standards for the definition of performance. In this section an attempt is made to review available quadrotor performance information and design aspects relevant to this study. The information was compiled from the literature [42] , manufacturer websites and quadrotor research projects   [14, 24, 43]. Both commercially available systems and selected research projects are presented. Planar multirotors, such as the Asctec Falcon with eight rotors, are based on very similar operational principles as quadrotors and were not included in the review.

Quadrotors can be found both in "X" and "+" configuration in which they have got either two or one rotors pointing in the preferred flying direction. The majority of the quadrotors presented are in "+" configuration but some key designs, such as the Draganflyer X4 operate in "x" configuration. The rotor spacing between rotor pairs is defined as the d/D ratio (illustrated later on in Figure 28) and is an important parameter for the rotor-interference study. Neither

the effects of rotor spacing nor the effects of quadrotor configurations appear to have been discussed in literature.

Most commercial quadrotors, with the exception of the Microdrones MD4-1000, are designed for small payloads of several hundred grams, whereas some academic quadrotors (Pounds and Stepaniak) were specifically designed for larger payloads. For most commercial quadrotors the payload fraction of the maximum takeoff weight appears to be around 15 to 27%.

Low endurance is often seen as one of the key limitations of small UAVs [44] and the platforms discussed in Table 1 show a strong variation in endurance between 10-30 minutes for most designs, whilst an endurance of 70 minutes for the md4-1000 is claimed by the manufacturer. From manufacturer websites it is, however, unclear under what conditions this endurance can be achieved. It is not specified if this means hover endurance and whether payload was reduced to accommodate further batteries.

Most published information leaves the forward flight performance and maximum wind speeds almost completely undefined. A selection of maximum "wind-loads" from [42] is included in the table, but from manufacturer data it is unclear what criteria were used for this definition. Some manufacturers claim a cruise speed (15 m/s for the Microdrones md4-1000) or a maximum speed (14 m/s for the Asctec Pelican). However, manufacturers generally do not provide clear indications of the conditions for these speeds (mass, payload, battery) nor do they typically provide any data on minimum power speed, maximum range speed or top speed. This leaves the forward flight performance of quadrotors largely undefined.
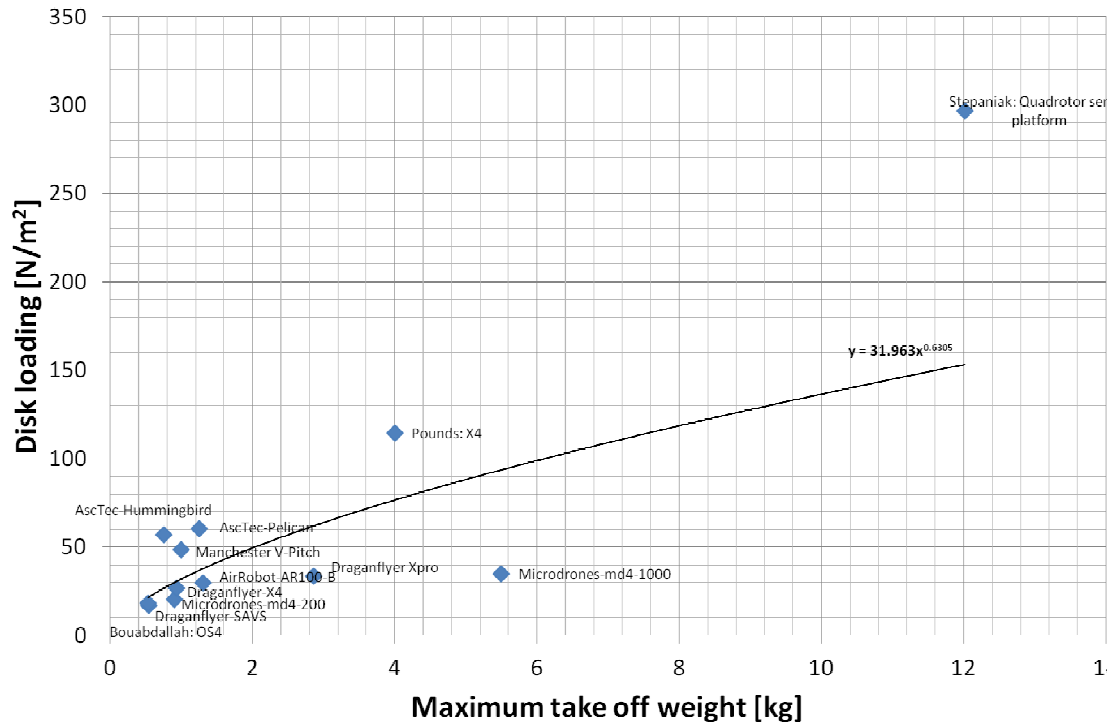
Figure 1: Disk loading for commercial and research quadrotor vehicles (based on Table 1).

A) Commercially available quadrotors

Name	Config.	MTOW [kg]	Payload [kg]	Payload fraction [%]	Endurance [min] *	Wind load [42] [m/s]	Range [42] [m]	Rotor Ø [m]	d/D	Disk loading [N/m²]	Battery Capacity [mAh]
AscTec-Hummingbird	+	0.75	0.2	27	12	10	500	0.203	1.18	56.83	3cell, 2100
AscTec-Pelican	+	1.25			11	10	1000	0.254	1.18	60.50	3cell, 6000
AirRobot-AR100-B	x	1.3	0.2	15	25	8	750	0.37	1.06	29.65	
Microdrones-md4-200	+	0.9	0.2	22	30	4	500-2000	0.37	1.03	20.53	4cell, 2300
Microdrones-md4-1000	+	5.5	1.2	22	70	5	500-2000	0.7	1.04	35.05	6 cell, 12000
Draganflyer-SAVS	+	0.54	0.085	16	12	4	250	0.313	1.21	17.21	3cell, 1300
Draganflyer-X4	x	0.93	0.25	27	20	4.5	500	0.3302	1.06	26.63	4 cell, 1920
Draganflyer Xpro	+	2.86	0.5	17	15			0.516	1.24	33.54	

B) Quadrotor designs from academia

Name	Config.	MTOW [kg]	Payload [kg]	Payload fraction [%]	Endurance [min] *	Wind load [m/s]	Range [m]	Rotor Ø [m]	d/D	Disk loading [N/m²]	Battery Capacity [mAh]
Bouabdallah: OS4	+	0.53	n/a		20 - 25			0.3	1.09	18.39	3cell, 3300
Pounds: X4	+	4.00	1	25	11	n/a		0.33	1.35	114.70	6x 4cell, 2000
Stepaniak	+	12.02	4.8	40	10			0.3556	1.41	296.83	4x 5cell, 8000

Table 1: Design and performance parameters for selected commercial and academic quadrotors (Based on manufacturer datasheets, a review by Prior [42] and research papers [14, 24, 43]), * not clear if with zero or full payload.

2.5 Conclusions on the state of the art

The literature review implies that the hover performance of quadrotors appears to be largely understood and that promising progress is reported in the area of blade optimization for micro air vehicles in hover. A range of low order models for motor and battery performance has been successfully applied to quadrotors. A consensus is emerging that flapping plays an important role in quadrotor forward flight and hingeless flapping models from the literature have successfully been applied and could be used for this thesis.

The performance and design of current quadrotors was reviewed. It was found that endurance data is difficult to compare due to open questions regarding the test conditions and that the forward flight performance of quadrotors is largely undefined. Furthermore, not a single forward flight power curve or discussion on minimum power, maximum range and top speed conditions could be found from manufacturer data or published work.

From the literature review it emerges that there is a lack of understanding on quadrotor forward flight performance and how it is affected by vehicle design. Many basic design questions, such as the effect of rotor spacing, fixed verses variable pitch rotors, flight configuration and CG position, remain unanswered. There is a lack of experimental data on rotor-rotor interference, quadrotor fuselage aerodynamics and the 3-DoF rotor forces/moments in forward flight. Furthermore, no experimental data on forward flight trim and power curves is available. On the modelling side no comprehensive model for quadrotor forward flight performance has been presented and limits to quadrotor maximum flight speeds have not been explored. All of the above presents a clear niche in which a contribution towards understanding quadrotor flight performance will be made in the present work.

Chapter 3: Theory and Simulation Model

The objectives of this chapter are to:

Combine, adapt and apply existing rotor aerodynamics and electric motor models to the particular situation of quadrotors in hover and forward flight and to introduce a simple method to stabilise the iteration process of a numerical blade element model.

3.1 Choice of modelling method and overview of modelling strategy

3.1.1 First principles vs. system identification strategies

There are two different modelling strategies commonly used for the modelling of miniature rotorcraft: systems identification techniques and first principles modelling [45]. Systems identification techniques use experimental data to relate the input and output of a "plant" around a typical operating point. First principles modelling uses the fundamental laws of mechanics and aerodynamics [45] to define a model, but requires detailed knowledge of the phenomena involved in rotorcraft flight [45] and potentially requires extensive validation and refinement [46].

A large part of the previous work on miniature rotorcraft modelling focused on control aspects and for control design simple linear models were often considered sufficient [45]. For these applications linear models, typically around hover, could be obtained from system identification strategies. Whilst this strategy is attractive for the control design of existing vehicles, it is not suitable for conceptual vehicle design or performance studies in which a large number of design parameters has to be covered over many points in the flight-velocity

envelope. Hence a first principles strategy was selected for the present research. The requirements for the detailed modelling choices were set as:

- Ability to readily cover a large parameter space of configuration designs and flight conditions.

- Work without the need for significant a priori knowledge beyond readily available data.

The modelling scope is set to the steady state hover, climb and level flight. This enables model validation using static hover tests and static wind tunnel experiments (see Chapter 4) without the need for experimental data on quadrotor dynamics.

3.1.2 Choice of rotor modelling method

The rotor model is the key element of the modelling work presented in this thesis. Six degree of freedom rotor forces and moments are required to model all realisable flight orientations.

Extensive literature exists on helicopter rotor modelling. Figure 2 shows a conceptual overview of the modelling choices available and orders the methods in terms of their complexity and computational effort. For flexible rotors further challenges arise in integrating the structural blade dynamics into simulations.

Modern higher order CFD methods, based on Euler/Navier-Stokes equations and often containing blade-vortex-interaction simulations, are on the far end of the spectrum and an area of active research. Those methods can model higher order effects such as rotor-rotor and rotor-fuselage interaction, but are computationally expensive and need an appropriate mesh representation of the actual vehicle geometry. Hence those higher order CFD methods are, at the time of writing, usually not practical for applications at early design stages or where a large range of parameters has to be studied.

At the other extreme are very low order analytical models, which have been typically used in past quadrotor research [16, 43]. Methods based on the actuator disk use basic momentum theory to describe the fundamental relationships between thrust, power and velocity at the disk. Actuator disk methods on their own cannot capture the effects of rotor geometry on the forces generated without a priori estimates of rotor performance. Analytical blade element solutions [18, 20] express relationships in simple closed-form equations and can give some appreciation of the effects of rudimentary design changes and operating conditions. However, they do not lend themselves to the integration of further models for inflow, flapping models or non-uniform blade geometry.

Numerical blade element models and vortex models are in the middle of the complexity range. Both methods are capable of providing the six degrees of freedom rotor forces and moments, but the numerical blade element model needs an inflow model. Vortex based models are often used in commercial comprehensive rotorcraft codes, such as Camrad II, and are computationally more expensive than blade element momentum codes. Schafroth [41] compared a vortex theory method with a blade element method, higher order CFD and experimental hover data, but no striking benefits of the vortex method over the blade element method were reported.

Of the methods compared, a numerical blade element was selected as most suitable for the aims and scope of the current study. A detailed description of the numerical blade element modelling is presented in Chapter 3.3 where the integration of the rotor geometry, flapping and inflow models are also discussed. At this stage, it is important to point out that a numerical blade element method is a relatively low-order method and limitations should be expected, which are further discussed in Chapter 3.3 and Chapter 5, where a comparison against wind tunnel data is presented.
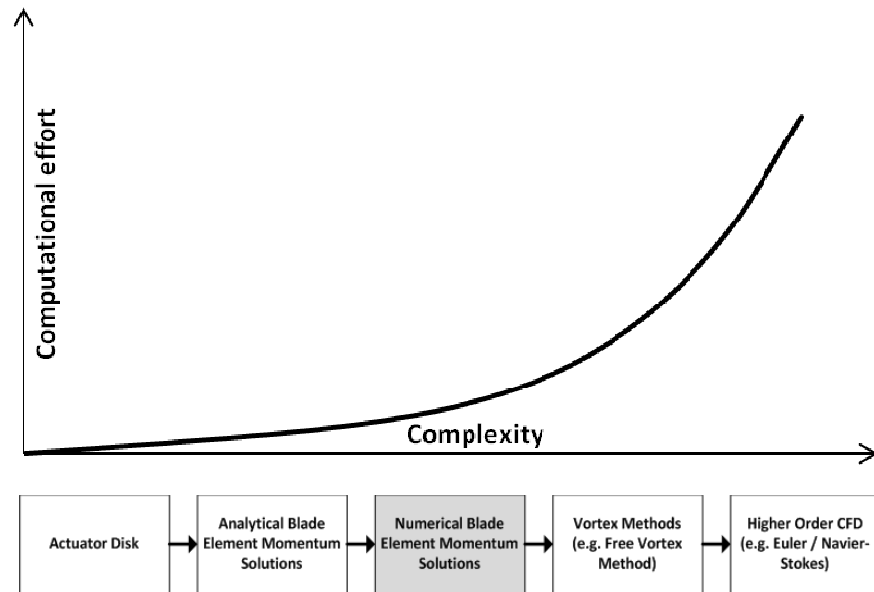
Figure 2: Conceptual overview of rotor modelling complexity and effort.

3.1.3 Overview of vehicle modelling concept

The proposed numerical blade element model forms the key element of a wider vehicle modelling concept, as presented in Figure 3, which was designed for the aim of quadrotor flight performance studies.

The vehicle simulation model uses a trim iteration loop to determine the vehicle trim curves (vehicle angle of attack, rotor pitch and rpm) as well as power conditions (total and individual motor power, torques, and efficiency) for a given user input. The user input consists of clearly defined operating conditions (desired flight speed, air density) and vehicle configuration (rotor positions, rotor geometry and material properties, airframe and payload mass properties, centre of gravity and centre of pressure) and basic electrical systems parameters (motor and battery constants).

An outer trim loop uses proportional control on the vehicle angle of attack and rotor demands (rpm, collective pitch) to reach zero net forces and moments about the centre of gravity of the particular vehicle configuration. To speed up convergence, the fuselage angle of attack is first approximated in an inner loop using the computationally inexpensive fuselage model, thereby reducing the number of iterations of the outer control loop which involve the

computationally more expensive rotor code. To reduce the computational effort no sideslip conditions were considered.

Within the outer trim loop, the rotor aerodynamics model is called at each iteration and provides an estimate of the forces and moments on each rotor, given the current flight conditions and rotor demand. Rotor torque and rpm are then used in the electric systems model to estimate electric power requirements. The trim routine ensures no saturation is reached and that the flight condition is physically possible, and breaks the loop once the residual forces and moments have reached a certain threshold value (typically 0.005 N and 0.005 Nm were used).

For the power optimisation of variable-pitch/variable-speed vehicles the vehicle simulation model was used in a batch processing mode, using fine steps for collective pitch and a simple minimum power search function.
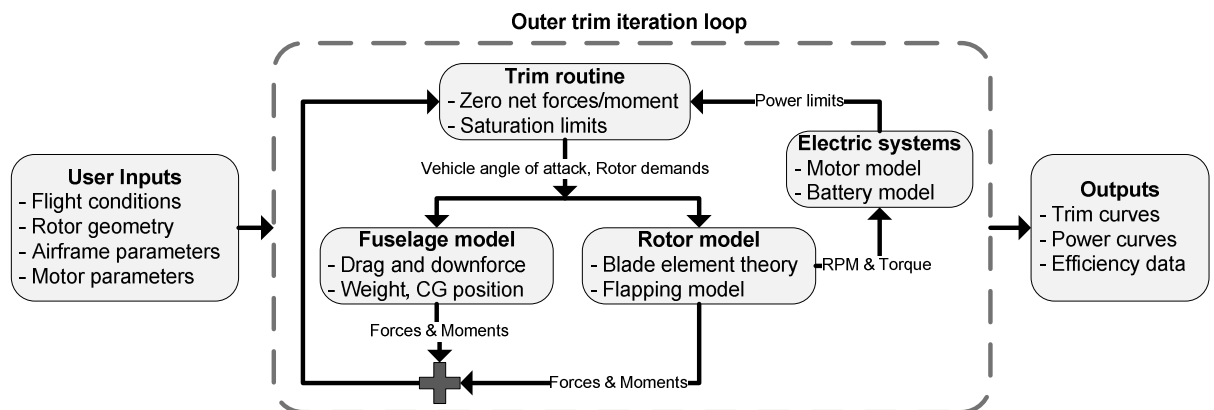
Figure 3: Conceptual diagram of the vehicle simulation model.

3.2 Coordinate Systems

3.2.1 Earth axes and the vehicle body coordinate system

A standard NED coordinate is used as an inertial, earth-fixed references system: The x-axis points north, the y-axis points east and the z-axis points down and normal to the ground which is considered flat.
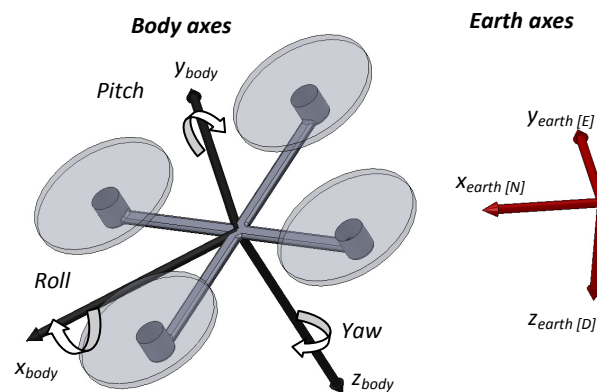
Figure 4: Quadrotor earth axes and body fixed coordinate system: Showing a negative vehicle angle of attack (nose down pitch) in forward flight.

For the vehicle body coordinate system a conventional helicopter notation is used. To keep the reference system independent of the actual position of the CG, a reference point at the centre of rotor plane (this is the intersection of the diagonals connecting the rotor hubs) is used. An orthogonal body-fixed coordinate system is established at this reference point and follows a right-hand rule.

- the z-axis points straight down when the vehicle is level (zero pitch and roll).

- the x-axis points forward in the preferred direction of flight, lies in the plane of symmetry and is perpendicular to the z-axis.

- the y-axis is perpendicular to the plane of symmetry and points starboard to complete the right-handed coordinate system.

The sign convention for the velocities follows the sign convention of the coordinate system. A positive forward velocity in body coordinates (u) is when the vehicle moves in its x-direction.

The attitude angles relating earth to body axes are defined as:

- ϕ, the roll angle about the x-axis, positive when disk tilts starboard.

- θ, the pitch angle about the y-axis, positive when the front of the disk pitches up.

- ψ, the yaw angle about the z-axis, positive when the nose rotates towards starboard.

The CG position with respect to the body axes system is represented by a position vector:

$$CG_{position} = (\Delta x_{cg}, \Delta y_{cg}, \Delta z_{cg}) \qquad\qquad \text{Eq. 1)}$$

3.2.2 Rotor numbering and position convention

Rotors are numbered consecutively in a clockwise manner (viewed from the top) starting from the front rotor (plus-configuration) or the front left rotor (x-configuration). The position and orientation of each rotor with respect to the reference point is expressed in a rotor position matrix M_{rotor_map} and a matrix of rotor shaft angles $M_{alpha\_rotor\_shaft}$. The direction of rotation of each rotor is defined in a rotation vector where a positive rotation is defined as counter-clockwise rotation when viewed from above.

For a typical quadrotor without any difference in vertical rotor position and a distance l between the rotor centre and the centre of the body reference frame the rotor position matrix is given as:

For a plus configuration: $\qquad M_{rotor\_map} = \begin{bmatrix} 1 & 0 & -1 & 0 \\ 0 & 1 & 0 & -1 \\ 0 & 0 & 0 & 0 \end{bmatrix} l$ $\qquad\qquad$ Eq. 2)

For an x configuration:
$$M_{rotor\_map} = \begin{bmatrix} 1 & 1 & -1 & -1 \\ -1 & 1 & 1 & -1 \\ 0 & 0 & 0 & 0 \end{bmatrix} \frac{\sqrt{2}}{2} l \qquad \text{Eq. 3)}$$

3.2.3 Rotor coordinate systems

For each rotor disk, a disk coordinate system is defined in the rotor hub plane. This disk coordinate system is used as a reference for all single rotor force and moment comparisons. The origin of the disk coordinate system is defined at the geometrical centre of the hub at a z-position of the rotor blades in rest (zero coning angle). The disk coordinate system is used with a sign convention as presented by Leishman [2] (see Figure 5). Body axes can be transferred to rotor disk axes by a $(180\ deg\ ^{+}/\!-\alpha_{shaft})$ rotation about the y-body-axis. A positive z-force in the disk coordinate system now points upwards and a positive x-force points backwards. The positive direction of the rotor rotation is defined as counter-clockwise as viewed from the top. The position of the blade is expressed by the azimuth angle ψ originating from the x-axis of the disk: For a positive direction of rotation the advancing blade is located at 90 deg and the retreating blade at 270 deg. To simplify computational procedures exactly the same disk coordinate system is maintained for negative directions of rotation (clockwise) in which case the advance side would be at 270 deg and the retreating blade at 90 deg. Sideslip cases could be considered by rotating the disk coordinate system in wind-axes, but no sideslip cases were considered in the performance study.

$\psi = 180^0$ Relative

windspeed V

Retreating side   Advancing side

$\psi = 270^0$ $\psi = 90^0$

$\psi = 0^0$
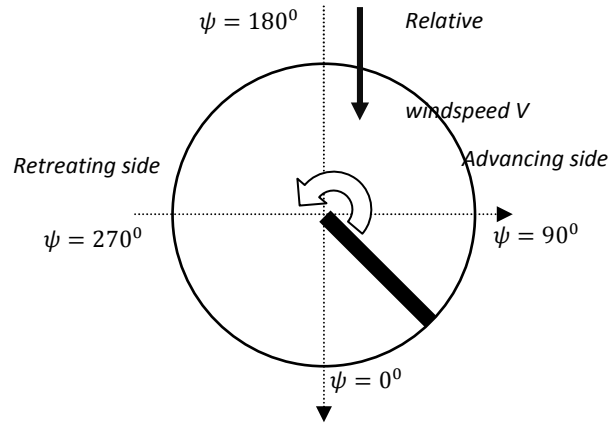
Figure 5: Rotor disk coordinate system shown for positive (counter-clockwise) and negative direction of rotation (based on [2]).

In addition to the body axes, several standard ([2], p190) rotor coordinate systems are defined to simplify analysis at a disk level as shown in Figure 6:

Tip Path Plane

Hub   fixed   system:

Disk axes

Reference   plane:

body x-y plane

Rotor shaft
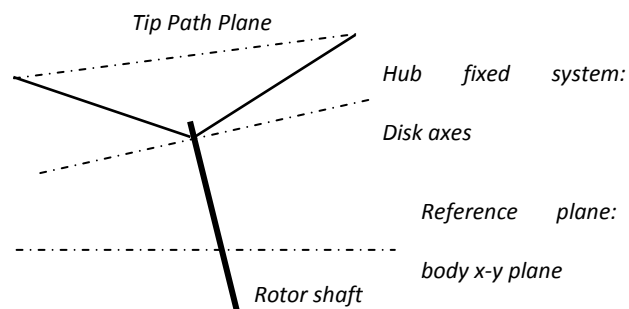
Figure 6: Rotor references systems used (based on [2]).

The Tip Path Plane (TPP) is described by the blade tips as these pass around the rotor hub. An observer on the TPP would not see any variation in flapping.

The Hub Plane (HP) is perpendicular to the rotor shaft and the HP is physically fixed to the body reference coordinate system and aligned with a rotor shaft angle α_{shaft}. The hub plane is used as a reference for the disk coordinate system described above into which all resultant disk forces are expressed and in which external velocity inputs are handed over to the blade element code.

3.2.4 Local blade coordinate system

For each blade element, a blade element coordinate system is defined that travels with the azimuth angle as well as the flapping angle of the blade element. The origin of the blade element coordinate system is the ¼ chord point in the spanwise centre of the blade element. From this origin the z-axis is defined perpendicular to the chord line and radial direction of the blade-element, the x-axis is parallel to the hub plane as shown in Figure 7 and the y-axis (not shown) forms a right-handed coordinate system.
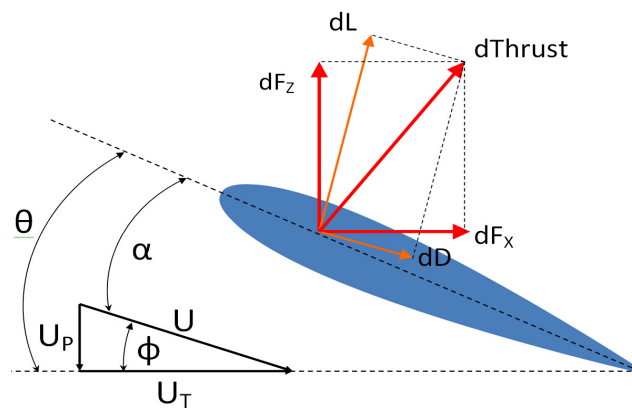
Figure 7: Local blade element coordinate system.

3.3 A numerical blade element model for hover and forward flight

3.3.1 Fundamentals of the BET method and disk discretization

In this section the fundamental principles of the numerical blade element model are discussed.

The blade element method is a well-established method [2], first envisaged by Froude, for rotor studies that works by breaking the rotor blade down into small elements. The local velocities and aerodynamic forces are analysed on every blade element and typically each element is treated as independent. Simple analytical expressions exist for hover, but complexity rises very quickly for forward flight cases in which the flow is no longer axisymmetric. The numerical method presented is different from analytical expressions because rotor blade element parameters are calculated one step at a time in a predefined order and then used in an iterative process. This eliminates the need to express all relationships in closed form equations.

A flow chart for the numerical blade element method developed for this research is shown in Figure 8. Before the code can be run the following models have to be defined:

- A rotor geometry model showing local blade pitch (twist) and chord as function of the radius.

- Flapping parameters (Lock number, blade inertia and flapping frequency ratios at typical hover rpm), further described in Chapter 3.3.3.

- 2d airfoil lookup tables (C_l,C_d) for the local blade airfoil section as a function of AoA and Reynolds number (Chapter 3.3.2).

The primary input parameters for the blade element code are rpm, collective pitch and the velocity vector onto the disk. Model settings also have to be defined at this stage (choice of inflow model, tip-loss model, convergence criteria and maximum number of iterations).
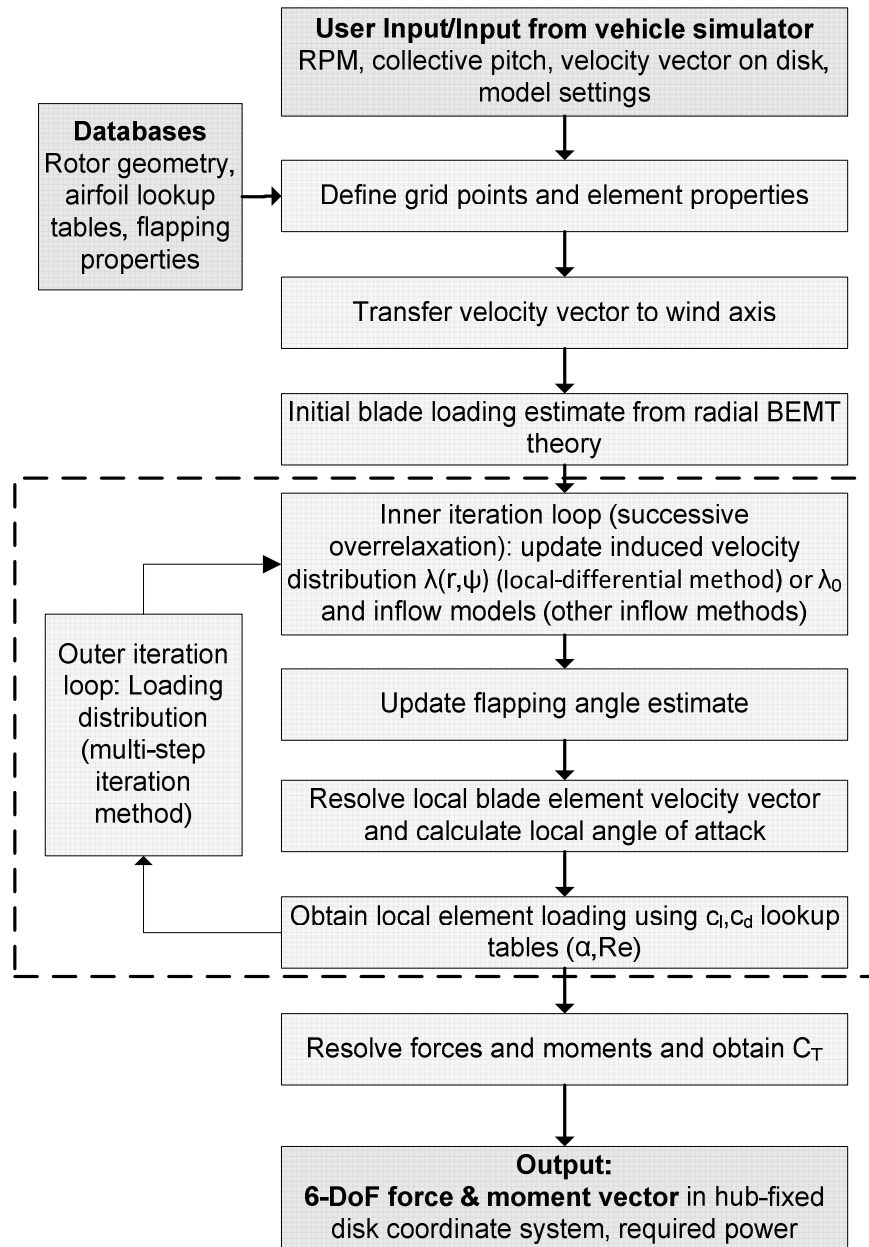
Figure 8: Flow chart of the numerical blade element model used in this study.

In the first simulation step the rotor disk in the hub reference plane is broken down into (M) radial elements and (K) azimuthal stations as shown in Figure 9. The blade position and each blade element property (local velocities, angle of attack, CL, etc) are stored in a matrix of the size (MxK) which is updated every iteration step.

The grid is defined based on the non-dimensional radial station r (0-1) at the spanwise centre of each blade element and equally spaced azimuth angles psi (0-360 deg) at the

element ¼ chord points. The coordinate system is based on the hub plane reference system in wind-axes and the absolute position of each blade element in Cartesian coordinates (assuming small flapping angles) is expressed as:

$$x_{hub} = \cos(\psi)rR_{max}$$ Eq. 4)
$$y_{hub} = \sin(\psi)rR_{max}$$ Eq. 5)
$$z_{hub} = \sin(\beta)rR_{max}$$ Eq. 6)

Two different methods for distributing the elements are studied: Equal-radius spacing, which eases the formulation of numerical solutions, and equal-area spacing which ensures each blade element covers an equal area and hence ensures a finer grid resolution towards the tips. Results for the comparison are presented in the "Numerical setup and sensitivity study" later on in Chapter 3.3.10.
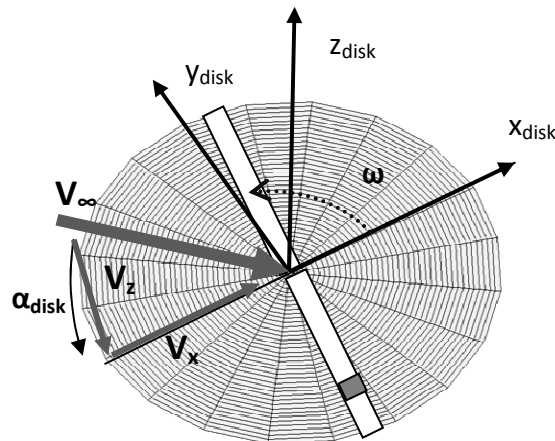
Figure 9: Blade element breakdown of the disk into local blade elements (equal-radius approach).

The velocity vector V onto the disk is broken down into components perpendicular to the disk V_z (positive downwards) and parallel to the disk V_x. For simplicity sideslip is ignored, but could be modelled with a rotation about the y-axis.

Before the start of the simulation the rotor loading is initially unknown and an initial estimate of induced velocity and loading are required. For moderate estimates that match the sign and approximate order of magnitude of the "true" solution, the iteration scheme appears

independent of the initial guess. A "good" initial guess can, however, lead to faster convergence and for most practical flight conditions and a radial inflow model [2] for hover was found to provide a good initial guess:

$$v_i(r) = \lambda(r)\Omega R = \frac{\sigma C_{l\alpha}}{16}\left(\sqrt{1 + \frac{32}{\sigma C_{l\alpha}}\theta(r)r} - 1\right)\Omega R \qquad \text{Eq. 7)}$$

, where σ is the rotor solidity, $\lambda(r)$ is the non-dimensional induced velocity and $C_{l\alpha}$ the 2d lift curve slope.

From the initial induced velocity estimate, the blade loading could be obtained numerically to start the iteration loops for induced velocity and blade loading. An optional tip-loss model for the 3d effects near the blade tips can be introduced and applied to the induced velocity at this stage (see Chapter 3.3.8)

Given the induced velocity vi as a function of the radial and azimuth position the mean inflow ratio is calculated and used to update the flapping estimate (detailed discussion in Chapter 3.3.3) which is expressed using the first harmonic flapping terms:

$$\beta = a_0 - a_1 cos(\psi) - sign(\Omega)b_1 sin(\psi) \qquad \text{Eq. 8)}$$

where a_0 represents the coning angle and a_1 and b_1 the longitudinal and lateral flapping angles in forward flight. The sign convention is such that the front of the disk flaps up and the advancing side flaps down. The periodic change in flapping angle with azimuth position can be expressed as:

$$\dot{\beta} = sign(\Omega)a_1 sin(\psi) - b_1 cos(\psi) \qquad \text{Eq. 9)}$$

Given the estimate of induced velocity, flapping, rpm and rotor airspeed the velocity elements at each blade element can be broken down as shown in Figure 10:

$$U_t = rR_{max}\Omega + sign(\Omega)V_x\sin(\psi) - u(r) \qquad \text{Eq. 10)}$$
$$U_p = v_i + V_z + rR_{max}\dot{\beta} + V_x\sin(\beta)\cos(\psi) \qquad \text{Eq. 11)}$$
$$U_r = V_x\cos(\psi) \qquad \text{Eq. 12)}$$

Which includes the effects of flapping from two perspectives: a) coning angle effects on the airflow, b) the flapping induced to the perpendicular velocity.

Given the independence principle of sweep [2], only U_t and U_p are considered for the calculation of lift:

$$U_{total} = \sqrt{U_t{}^2 + U_p{}^2} \qquad \text{Eq. 13)}$$

whereas the radial velocity U_r is only added for drag estimates.

The local Reynolds number at the blade element is defined using the local chord length and airspeed U:

$$Re = \frac{\rho U_{total}c}{\mu} \qquad \text{Eq. 14)}$$

where μ is the dynamic viscosity of air (at ISA Sea Level) and not the advance ratio of the blade.

On the retreating side, the resultant of forward flight velocity and rotational speed can lead to an area of negative tangential velocity: the "reverse flow" area. The code considers this by switching the direction of drag to allow a correct sign of the flow and by making modelling provisions for large local angles of attack (see Chapter 3.3.2).

Next, the velocity components are used to determine the inflow angle for each blade element:

$$\phi = \tan^{-1}\left(\frac{U_p}{U_t}\right)$$

<div align="right">Eq. 15)</div>

Each element has a local pitch angle θ which is defined as the angle between the chord line and the hub plane. It is a result of collective pitch and the twist distribution along the blade radius. Knowing both local pitch and inflow angle the local angle of attack is determined as:

$$\alpha = \theta - \phi$$

<div align="right">Eq. 16)</div>

Given the local angle of attack and Reynolds number the 2-d lift and drag coefficients C_l and C_d at every blade element are obtained from a lookup-model that uses 2-d interpolation (α,Re) on a +/- 180 deg airfoil dataset. The dataset can be either based on experimental data or synthetic airfoil data which is discussed in more detail in Chapter 3.3.2. The element lift and drag are now calculated as:

$$L = \frac{1}{2}\rho U_{total}{}^2 C_l c dy$$

<div align="right">Eq. 17)</div>

$$D = (sign(U_t))\frac{1}{2}\rho\left(\sqrt{U_{total}{}^2 + U_r{}^2}\right)^2 C_d c dy$$

<div align="right">Eq. 18)</div>

These blade element lift and drag force components are in the local blade element coordinate system and have to be resolved to disk coordinates to give the incremental disk coordinate forces f_x, f_y, f_z by considering the effects of flapping and azimuth angle on the position of the blade element:

$$f_x = \sin(\psi)\, sign(\Omega)[L\sin(\phi) + D\cos(\phi)] \\ - \cos(\psi)\sin(\beta)[L\cos(\phi) - D\sin(\phi)]$$

Eq. 19)

$$f_y = -\cos(\psi)\, sign(\Omega)[L\sin(\phi) + D\cos(\phi)] \\ - \sin(\psi)\sin(\beta)[L\cos(\phi) - D\sin(\phi)]$$

Eq. 20)

$$f_z = \cos(\beta)[L\cos(\phi) - D\sin(\phi)]$$

Eq. 21)

The time-averaged total thrust on the rotor can now be calculated by summing up f_z over all blade elements and averaging it for one rotor revolution:

$$F_Z = T = \frac{N_b \sum f_z}{K}$$

Eq. 22)

At this stage the local (local-differential model) or global (other inflow models) loading estimate is used in the outer iteration loop to provide a revised estimate of the induced velocity and new blade loading.

Once the loading iteration loop has converged to a stable local loading (local-differential method) or stable total thrust (other inflow methods), defined as within 0.05% of the previous loading estimate, the outer iteration loop is stopped. The total time-averaged rotor forces F at disk level can now be calculated from the local loading distribution:

$$F_j = \frac{N_b \sum f_j}{K}$$

Eq. 23)

where the subscript j represents the individual axes x,y,z.

The reaction torque at every blade element is:

$$m_z = -sign(\Omega)rR_{max}[L\sin(\phi) + D\cos(\phi)]$$

<div align="right">Eq. 24)</div>

So that the total reaction torque can be expressed as:

$$M_Z = \frac{N_b \sum m_z}{K}$$

<div align="right">Eq. 25)</div>

Rolling and pitching moments arise from the aerodynamic moments (unequal lift distribution on the disk) and, for hingeless rotors, the transfer of flapping moments to the rotor hub [7, 16]. For relatively "stiff" rotors typically used on quadrotors the flapping-induced rolling and pitching moments due to the combined stiffness term k_β appear dominant. k_β is dependent of the blade flapping characteristics as well as the rotational speed Ω as discussed in Chapter 3.3.3. The total rolling and pitching moment are approximated in the disk coordinate system as:

$$M_x = \frac{N_b \sum y_{hub} f_z}{K} - \frac{N_b}{2} k_\beta b_1$$

<div align="right">Eq. 26)</div>

$$M_y = \frac{N_b \sum -x_{hub} f_z}{K} + \frac{N_b}{2} k_\beta a_1$$

<div align="right">Eq. 27)</div>

Forces and moments are expressed as non-dimensional coefficients:

$$C_{Fj} = \frac{F_j}{\rho A_{disk}(\Omega R_{max})^2}$$

<div align="right">Eq. 28)</div>

$$C_{Mj} = \frac{M_j}{\rho A_{disk} R_{max}(\Omega R_{max})^2}$$

<div align="right">Eq. 29)</div>

where the thrust coefficient C_T in disk coordinates is defined to be identical to C_{Fz}

The mechanical shaft power for the given operating conditions is now calculated as:

$$P_{mech} = M_z \Omega$$

Eq. 30)

and can be expressed in a non-dimensional power coefficient C_P:

$$C_P = \frac{P_{mech}}{\rho A_{disk}(\Omega R_{max})^3}$$

Eq. 31)

which has the same magnitude as the torque coefficient C_{Mz}. The aerodynamic efficiency "Figure of Merit" can be calculated based on :

$$FoM = \frac{P_{ideal}}{P_{mech}} = \frac{C_T^{3/2}}{\sqrt{2}C_P}$$

Eq. 32)

The formulation based on the thrust and power coefficients simplified obtaining the Figure of Merit from experimental hover tests.
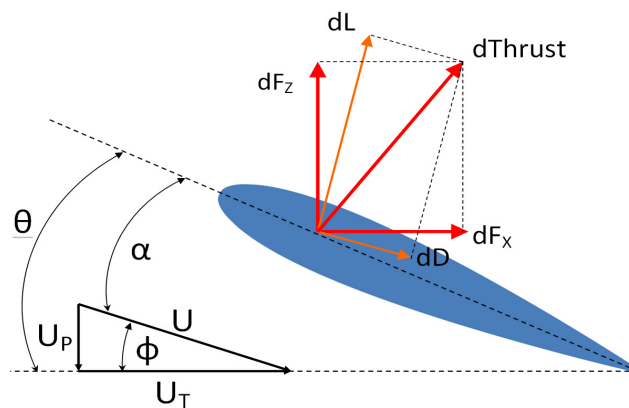
Figure 10: Breakdown of velocity and force components at each blade element.

3.3.2 Blade section airfoil properties

3.3.2.1 Section identification

A problem regularly faced when working with small-scale commercial off-the-shelf rotors is the identification of the airfoil section and the subsequent prediction of lift and drag characteristics. For the purpose of this work the thickness/chord ratio and manufacturer information were used to estimate the blade airfoils to the nearest known standard profile. The variable-pitch rotor was matched to a NACA0012, although a slightly increased leading edge thickness was noted. The fixed-pitch APC rotor was closest matched by a Clark-Y airfoil.

3.3.2.2 Reynolds and angle of attack range

The test rotors used in this study typically operate at small Reynolds numbers below 200k and the variation of the Reynolds number along the blade was found to cause strong variations in lift/drag coefficients making it advisable to include the Reynolds number as a dimension in the lookup tables. To restrict the range of the lookup table, practical limits to minimum and maximum Reynolds numbers were defined based on the mean chord and typical operation conditions: The minimum (Re_{min} = 7k for the variable-pitch rotor) was fixed by considering the local velocity at ¼ radius at the minimum motor rotational speed. The maximum was fixed by the maximum rpm and advance ratio at the blade tip (Re_{max} = 190k).

To cover all possible blade element conditions, like the reverse flow region, a +/- 180 deg angle of attack lookup table is required for a robust blade element model. However, for most practical purposes the key focus is on moderate local angles of attack of between 0-15 deg. Practical model extensions for off-design conditions beyond this range will be discussed later.

3.3.2.3 Xfoil integration

2d airfoil datasets were created using the well-known xfoil software [47] which is based on an extended panel method and was originally designed for low Reynolds number applications. The transition prediction in XFOIL is based on a simple e^n method [47], and a suitable ncrit

parameter had to be selected to "represent the background disturbance level". The manual suggests ncrit values of between 12 and 14 for sailplanes (clean configuration) and smaller values of between 4-8 for "dirty windtunnels". During a numerical investigation a slightly smaller value of ncrit=3 was found most suitable for the rotating environment, because it ensures numerical convergence for the Reynolds number range studied.

Open-source Matlab scripts [48] were used to integrate Xfoil into Matlab and batch process the Reynolds number and angle of attack range. Low angles of attack between 0 and 15 deg were evaluated in 0.1 deg increments using a high number of iterations and checking each data point for convergence. Symmetric airfoil data was mirrored to give data for negative angles of attack. Xfoil was used in "viscous mode" for each Reynolds number. For the Mach number range (<0.3) low compressibility was expected, but Xfoil includes a Karman-Tsien compressibility correction and some test cases appeared to show slight sensitivity to the highest tip Mach number (0.25). To limit the number of parameters to two (AoA,Re) and ensure consistency, the local Mach number was coupled to each Reynolds number using the mean chord and sea level hover conditions.

3.3.2.4 A quasi-steady model for high angles of attack

In some extreme flow conditions local blade elements can experience off-design angles of attack beyond the 0-15 deg range studied with Xfoil. A standard high angle of attack model based on Leishman [2] is used to approximate the quasi-steady lift and drag coefficients at high angles of attack beyond stall:

$$C_l = A \sin[2(\alpha - \alpha_0)] \qquad\qquad \text{Eq. 33)}$$

$$C_d = D + E \cos[2(\alpha - \alpha_0)] \qquad\qquad \text{Eq. 34)}$$

where the coefficients A,D and E were slightly modified from literature values (1.1, 1.135 and -1.05) to match up with the lower angle of attack Xfoil results for each Reynolds number curve. Using this model the lookup table was extended to angles up to 180 deg. The process was repeated for negative angles of attack. The simplified model was considered acceptable, because high local angles of attack typically occur in areas of low dynamic pressures and hence low total forces are expected. Structural blade twisting and the effects of high angles of attack on the centre of pressure were not considered.

3.3.2.5 Limitations of the xfoil model

There are few reliable sources in literature to validate the 2d airfoil results over the full angle of attack and Reynolds number range used in this study. However, the following methods and sources can be used for partial comparison and are shown in Figure 11:

- One research report [49] presents selected NACA0012 cases at low Reynolds numbers relevant to this research, but its validity is uncertain, because data was extrapolated from tests at higher Reynolds numbers and shows an unexpected stall behaviour and strong fluctuations in the drag coefficient.

- An inverse method to obtain C_{D0} from thrust and power coefficients, as presented in Chapter 5, allows for a basic blade-average profile drag comparison.

- Literature results for drag obtained using an inverse method on a geometrically similar rectangular NACA0012 blade [38].

- A polynomial drag curve fitted using collective pitch experimental data and the blade element method.
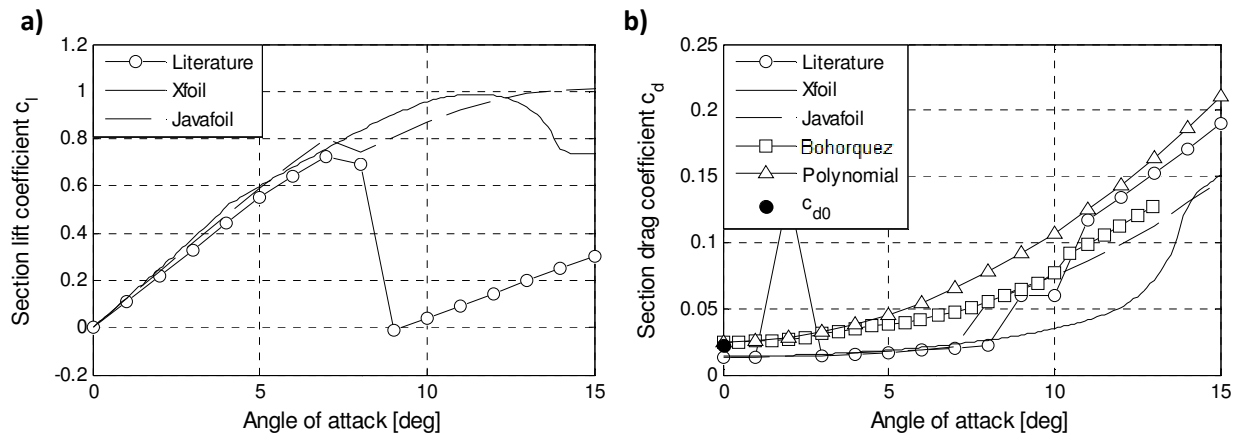
Figure 11: Comparison of sectional airfoil characteristics at Re=80k. "Literature" results from [49], further experimental results are shown from Bohorquez [38], and data extrapolated from experiments (Chapter 5).

The comparison of data and the study of literature lead to the following conclusions and limitations on the Xfoil modelling:

- The very low angle of attack lift coefficient prediction shows acceptable agreement for all models up to about 7.5 deg.

- C_{Lmax} prediction is difficult, the post-stall behaviour is especially difficult if there is a kink in the lift curve [50]; experimental post-stall lift results [49] show an unexpected behaviour.

- The c_{d0} appears to be significantly underpredicted when compared to c_{d0} values obtained from experimental thrust and power coefficients (which could be affected by swirl)

- Literature suggests that "*XFOIL maintains attached flow until a higher angle of attack and hence underestimates drag at higher angles of attack*" [51] this is supported if the simulated drag coefficient is compared against inverse experimental results from Bohorquez [38] and a polynomial extrapolated from experimental power and collective pitch data.

- The high angle of attack model extension is a crude approximation, but its limited fidelity is acceptable because of the low dynamic pressures and hence total forces [2] in typical areas of high local angles of attack.

58

Given the lack of suitable alternatives the Xfoil model is considered acceptable, but strong limitations are expected for high angle of attack cases near or beyond stall. Finally, it has to be considered that the actual airfoil section might deviate from its nearest approximate section due to small-scale manufacturing tolerances and design issues, especially with the leading edge radius. This could explain why the simulated drag results are lower than experimental fits and makes it important to use the variable-pitch rotor hover experiments as a calibration case.

3.3.3 Flapping modelling

3.3.3.1 Flapping effects in forward flight

The rotor aerodynamic forces can lead to three main effects on the motion of the rotating blade: Flapping, feathering and lead-lag motion. For the rotors analysed in this study feathering is ignored and lead-lag is typically ignored for the purpose of flight mechanics, because it *"contributes little to the overall response [...] of the helicopter"* ([7], p134). Flapping which is the up or down movement of the rotor blades, however, can have profound effects on flight mechanics and has to be considered for quadrotor studies [16, 28].

In hover, the aerodynamic loading can cause the blade to deflect up by the coning angle a_0. In forward flight the imbalance of lift on the advancing and retreating side causes an upwards flapping velocity on the advancing and a downwards flapping velocity on the retreating side. The highest value of longitudinal flapping is normally reached at the front of the rotor disk, close to 90 deg shifted from the advancing side due to gyroscopic effects. This results in an increasing backwards tilt of the rotor tip-path plane with increasing flight speed. The longitudinal thrust variation due to coning and inflow distribution normally causes the advancing side to flap down [2, 11, 52]. The significance of flapping for this work is that it adds local velocity components to the blade elements, deflects thrust away from the shaft axis and contributes towards the hub moments.

For the aims of this study a steady-state flapping model is required that describes *"the steady motion in forward flight corresponding to a given collective pitch angle, tip speed ratio and inflow ratio – these conditions completely define the operating state of the rotor" ([10], p 106).*

3.3.3.2 Types of flapping mechanisms

Three main types of rotor flapping mechanisms commonly used on helicopters are illustrated in Figure 12:

- Articulated rotors have mechanical flapping hinges to allow free flapping motion, the hinge is offset from the shaft centre by a distance e (normalised to the rotor radius).

- Teetering rotors connect two blades together and are mechanically simple.

- Hingeless rotors do not have flapping hinges, but achieve blade articulation through the elastic bending of the blade or specially design structural beams; they are typically used for their simple hub design and because they can generate greater hub moments ([10], p107).
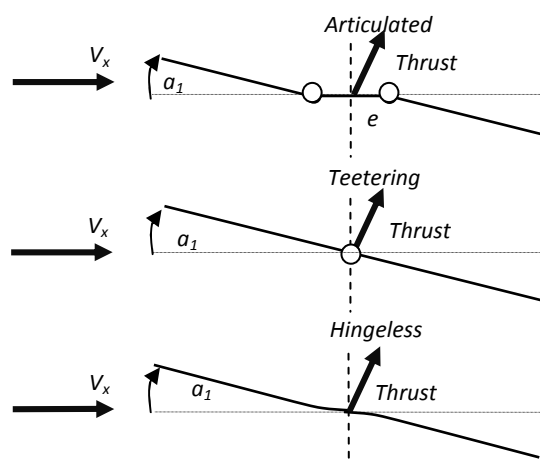
Figure 12: Main types of flapping mechanisms.

With the exception of the teetering rotor design by Pounds [14] virtually all quadrotors use hingeless rotors. Unlike modern helicopter rotors most quadrotor rotors do not include a specifically designed flexure in the root design and hence literature data on the rotor flapping stiffness and frequency ratios do not necessarily apply to quadrotors.

3.3.3.3 A simplified forward flight hingeless flapping model

The main strategies to approximate the flapping of a hingeless rotor are shown in Figure 13: A flexible hingeless rotor can be approximated using an equivalent flapping hinge offset e_{eqv} and an equivalent torsional spring at the equivalent flapping hinge, a strategy previously applied to small-scale hingeless rotors [40] and in classic helicopter literature [2, 11]. A second method is to use an equivalent centre spring to match the flapping frequency ratio. For this work Newman's [11] hingeless flapping model with an equivalent centre spring approach is used. The flapping frequency ratio for the centre spring model is obtained by first using the equivalent hinge offset and equivalent spring stiffness, and then transferring them into a combined centre spring stiffness (see Chapter 3.3.3).
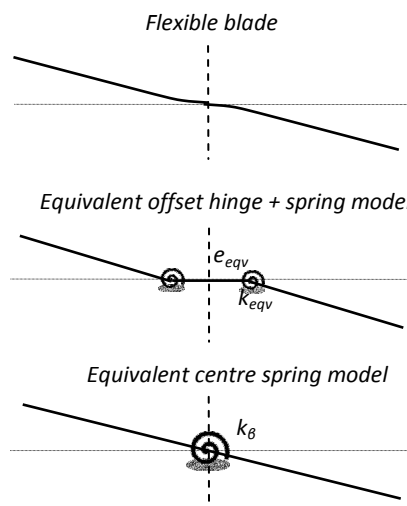
Figure 13: Equivalent model for a hingeless blade.

The steady-state flapping motion can be described as:

$$\beta = a_0 - a_1 cos(\psi) - b_1 sin(\psi) \qquad \text{Eq. 35)}$$

Only first order harmonic terms are considered, because literature suggests that the magnitude of higher order coefficients decreases rapidly by about a factor of 10 per order [10]. The first two azimuthwise derivatives for an anti-clockwise rotor are expressed as

$$\beta' = a_1 sin(\psi) - b_1 cos(\psi) \qquad \text{Eq. 36)}$$

$$\beta'' = a_1 cos(\psi) + b_1 sin(\psi) \qquad \text{Eq. 37)}$$

Rather than obtaining the flapping coefficients a_0, a_1 and b_1 from a computationally-expensive dynamic solution, a first order steady-state hingeless flapping model from literature is used. The method presented by Newman ([11], p109) gives a_0, a_1 and b_1 as a function of horizontal and vertical advance ratio, pitch, inflow ratio and blade properties and has successfully been applied to quadrotor research by Hofmann [16]. Only the key steps of the derivation from [11] and its adaptation to the numerical code are discussed here.

Newman's flapping model is based on a series of assumptions:

- The blade is rigid, which implies that all bending is assumed to happen in the root region and the blade is considered straight for any point outboard of $e_{eqv.}$

- There is no flap hinge offset considered on aerodynamic moments (the effects of the equivalent hinge offset are modelled using a combined equivalent spring stiffness).

- Terms of order $O(\mu^2)$ can be neglected.

- The lift curve slope for the determination of aerodynamic moments is constant.

Like in most flapping derivations the balance of moments at the equivalent flapping hinge is used as a starting point:

$$I_\beta \ddot{\beta} = M_A - k_\beta \beta \qquad \text{Eq. 38)}$$

Where I_β is the inertia about the equivalent flapping hinge, M_A is the aerodynamic moment and k_β is an equivalent stiffness that combines the centrifugal force term and any flexural stiffness.

Next the flapping frequency ratio λ_β is defined as the ratio of natural flapping frequency *in vacuo* and rotor rotational speed:

$$\lambda_\beta = \frac{\omega_\beta}{\Omega} \qquad \text{Eq. 39)}$$

The determination of λ_β is not straightforward and a first-principles approximation method is presented later on in Chapter 4.5.3.4. The flapping frequency ratio is now used to express the combined stiffness k_β as:

$$k_\beta = I_\beta \Omega^2 \lambda_\beta^2 \qquad \text{Eq. 40)}$$

Equation 38 can now be re-expressed using the second azimuth flapping derivative β'' and the flapping frequency ratio from equation 40:

$$\Omega^2 I_\beta \beta'' + \Omega^2 I_\beta \lambda_\beta^2 \beta = M_A \qquad \text{Eq. 41)}$$

which can be simplified as:

$$\beta'' + \lambda_\beta^2 \beta = \frac{M_A}{\Omega^2 I_\beta} \qquad \text{Eq. 42)}$$

Using the azimuth derivatives from Eq 36 and Eq 37 the left hand side can be expressed as:

$$\beta'' + \lambda_\beta^2 \beta = a_1 cos(\psi) - b_1 sin(\psi)$$
$$+ \lambda_\beta^2 \big(a_0 - a_1 cos(\psi) - b_1 sin(\psi)\big) \qquad \text{Eq. 43)}$$

Next the aerodynamic contribution of the flapping moment is given by:

$$M_A = \int_0^1 dLrR = \int_0^1 \frac{1}{2}\rho U_T^2 cdrRC_{l\alpha}\alpha Rr$$

Eq. 44)

Analytical approximations for the velocity terms and angle of attack (see Chapter 3.3.1) can now be inserted into Equation 44 and integration can be performed. Using trigonometric identities the resulting equation can be simplified and rearranged into a Fourier series. The detailed analytical process is shown in (Newman [11], p111) and is not repeated here. If only coefficients of 1, $cos\psi$ and $sin\psi$ are considered M_A can be expressed as:

$$M_A = \frac{1}{2}I_\beta\gamma\Omega^2 \left[1\left(\frac{1}{4}\theta_0 - \frac{1}{3}\mu_x B_1 - \frac{\mu_{zD}}{3}\right) \right.$$
$$+ cos\psi\left(\frac{b_1 - A_1}{4} - \frac{\mu_x}{3}a_0\right)$$
$$\left. + sin\psi\left(\frac{2}{3}\mu_x\theta_0 - \frac{a_1 + B_1}{4}\right)\right]$$

Eq. 45)

Where A_1 and B_1 are the cyclic control inputs (both zero for quadrotors), θ_0 is the collective pitch setting (for blades with twist the pitch at ¾ radius is used), μ_{zD} is the vertical advance ratio including the inflow ratio and γ is the Lock number that expresses the relationship of aerodynamic to inertial forces:

$$\gamma = \frac{\rho C_{l\alpha}cR^4}{I_\beta}$$

Eq. 46)

Equation 43 and 45 can now be combined and equated by the coefficients of 1, $cos\psi$ and $sin\psi$ as shown in [11]. For the purpose of this research the resulting relationship is expressed in matrix form and both cyclic pitch inputs A_1 and B_1 are set to zero:

$$\begin{bmatrix} \lambda_\beta^2 & 0 & 0 \\ \dfrac{\gamma}{6}\mu_x & (1-\lambda_\beta^2) & -\dfrac{\gamma}{8} \\ 0 & \dfrac{\gamma}{8} & (1-\lambda_\beta^2) \end{bmatrix} \begin{pmatrix} a_0 \\ a_1 \\ b_1 \end{pmatrix} = \frac{\gamma}{2} \begin{pmatrix} \left[\dfrac{\theta_0}{4} - \dfrac{\mu_{zD}}{3}\right] \\ [0] \\ \left[\dfrac{2}{3}\mu_x\theta_0\right] \end{pmatrix} \qquad \text{Eq. 47)}$$

This matrix equation lends itself to integration into a numerical blade element code. The solution for the flapping angles depends on the blade flapping parameters λ_β and γ (which are derived in the next section), the operating conditions (advance ratio, collective pitch) and the induced velocity contained in the μ_{zD} term. The induced velocity term is obtained by integrating Eq 47 into the numerical blade element code where the flapping estimate is updated with a disk-average induced velocity estimate at every iteration step.

By setting the flapping frequency λ_β to 1, the above model could also be applied to approximate teetering rotors.

3.3.3.4 Determination of the blade flapping properties

Whilst research on conventional helicopters can often draw on flapping frequency ratios from literature and experience, typical values for quadrotor rotors are initially unknown. For the aim of this work a simple first-principles approach is required to approximate the blade flapping frequency ratio. The method presented here is largely based on classic work by Young [53] and other rotorcraft literature ([2], p201). It is updated by using simple Euler-Bernoulli beam equations and numerical integration solutions to blade properties (second moment of area).

To approximate the blade flapping frequency the semi-rigid rotor is initially assumed to have an equivalent spring stiffness k_{eqv} at an equivalent hinge offset e_{eqv}. The non-dimensional flapping frequency ratio λ_β consists out of the contribution of centrifugal forces (given the equivalent hinge offset) and the non-rotating frequency $\lambda_{\beta 0}$ ([11], p96, Leishman [2], p201):

$$\lambda_\beta^2 = \left(1 + \frac{3}{2}e_{eqv}\right) + \lambda_{\beta 0}^2 \qquad \text{Eq. 48)}$$

The non-dimensional non-rotating frequency is obtained by considering the blade as a cantilever beam and normalising the natural bending frequency against the rotor speed:

$$\lambda_{\beta 0} = \frac{\omega_{no}}{\Omega} = \frac{1}{\Omega} 1.875^2 \sqrt{\frac{EI_x}{R^4 \frac{M_{blade}}{R}}} \qquad \text{Eq. 49)}$$

Where E is the Young's modulus for the blade material and I_x is the second moment of area about the neutral axis of the spanwise beam bending.

I_x is identified by breaking down the airfoil section into small chordwise elements as shown in Figure 14 and summing up the I_x contributions from all elements. The rotor blade is idealised as having a constant chord (mean chord), constant airfoil and constant mass distribution along the radius. Given the uncertainty in material properties and the simplified blade model the estimates of the product EI_x were validated against the experimental tip-deflections of the blades used in this study.

The equivalent hinge offset is approximated using the beam shape found from the Euler-Bernoulli beam bending theory. The blade is approximated as a cantilever ([9], p234) with an arbitrary load concentrated at ¾ radius. The equation of a straight line is fitted using the slope around the ¾ radius point as shown in Figure 14 and used to define the equivalent hinge offset e_{eqv}.

a)   b)
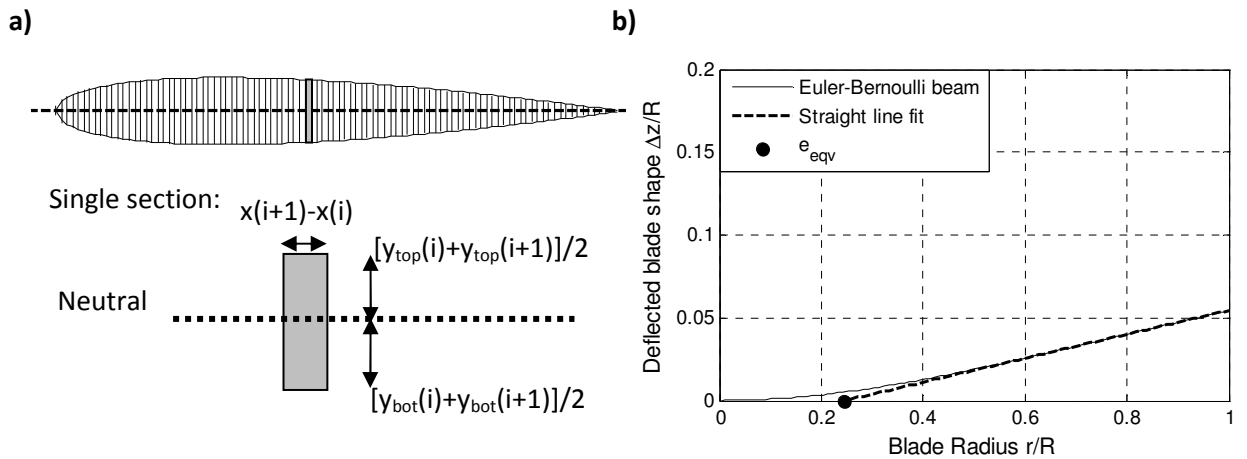
Figure 14: a) numerical identification of second moment of area and b) Euler-Bernoulli beam bending model
to identify the equivalent hinge offset.

The method was used to obtain the blade properties for the two main rotors used in this
research (see Table 2). The flapping frequency values obtained are slightly larger than
literature results for typical hingeless rotorcraft (1.1-1.2), but indicate that the structural
stiffness is still relatively small compared to the centrifugal stiffness ([9], p315). The stiffness
value k_β represents the combined equivalent centre stiffness (see Eq 38) to be used in the
transfer of moments to the hub as shown in Chapter 3.3.1. I_β was measured from $e_{eqv.}$

Rotor	Base RPM	M_{blade} [kg]	R [m]	e_{eqv} [-]	I_β [kg*m^2]	λ_β [-]	Υ [-]	k_β [Nm/rad]
Vpitch	5000	0.003	0.1270	0.245	6.93e-6	1.3510	6.6554	1.5683
APC	7000	0.0029	0.1016	0.245	4.29e-6	1.2024	2.8086	1.0273

Table 2: Blade properties for the flapping model.

3.3.4 Uniform inflow and linear harmonic inflow models for forward flight

3.3.4.1 Introduction

As a result of the conservation of mass, momentum and energy the thrust produced
on a rotor disk gives rise to an induced velocity v_i. The induced velocity forms an important
part of the velocity vector on every blade element and strongly influences the local blade
element angle of attack as shown in Equation 11. In this section several well-known [2, 54]

momentum theory based solutions for the induced velocity and their implementation into the blade element code are discussed. An extended local-differential model and the alternative Mangler-Squire inflow model are then presented later on in Chapters 3.3.5 and 3.3.6. Common assumptions for the models presented in this section are that the induced velocity is considered 1d and incompressible through the slipstream.

3.3.4.2 Induced velocity in hover

In the most basic form of the momentum theory as presented by Rankine in 1865 [2] the rotor is modelled as an actuator disk, based on the following assumptions:

• Infinitely thin disk with area $A_{disk.}$

• A one dimensional, azimuthally axisymmetric flow ignoring rotational effects.

• Uniform disk loading.

• Steady, inviscid, incompressible conditions.

• Free stream static pressure in the far upstream and downstream region.
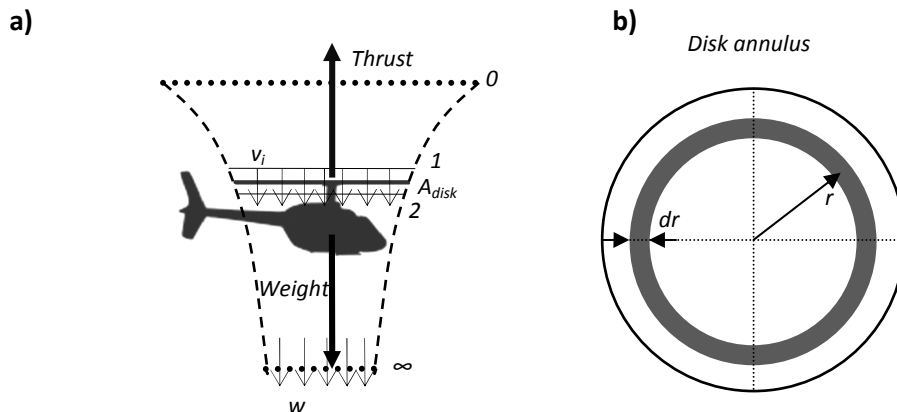
Figure 15: Conservation of momentum on a disk level (a); disk annulus (b).

A control volume is defined surrounding the rotor and its wake as shown in Figure 15 a. The upper "0" and lower "∞" boundaries are defined far upstream and far downstream, where the pressure is assumed to be the ambient pressure. Positions 1 and 2 mark the boundaries just above and below the rotor disk plane.

The mass flow through the control volume can be defined as:

$$\dot{m} = \rho A_\infty w = \rho A_1 v_i = \rho A_2 v_i$$

Eq. 50)

The conservation of momentum is used to relate the thrust produced to the change of momentum across the control volume. In hover the air above the rotor has a velocity of zero and the conservation of momentum is expressed as:

$$T = \dot{m}w$$

Eq. 51)

Next, the conservation of energy is used to relate the rotor power to the time-wise gain in energy of the fluid in the control volume:

$$P = Tv_i = \frac{1}{2}\dot{m}w^2$$

Eq. 52)

Combining the last two equations the relationship between v_i and w can be established as

$$v_i = \frac{1}{2}w$$

Eq. 53)

and the induced velocity at the disk is expressed as a function of thrust:

$$v_i = \sqrt{\frac{T}{2\rho A}}$$

Eq. 54)

This simple relationship can be used in a first-order iterative blade element analysis to estimate the uniform disk-average induced velocity in hover which is then updated with every new thrust estimate until convergence is reached.

Whilst the method presented above ensures a global convergence on the disk level it over-simplifies the local flow conditions by predicting a constant induced velocity along the blade radius. This can be overcome by the work of Froude and Finsterwalder as shown in [2]. The Froude-Finsterwalder equation reformulates the momentum theory presented above for each disk annulus as shown in Figure 15 b). The incremental thrust on the annulus can be related to the induced velocity on the annulus:

$$dT = 4\pi\rho(V_c + v_i)v_i y dy \qquad\qquad \text{Eq. 55)}$$

where V_c presents the climb velocity of the rotor. The method assumes that disk annuli are strictly independent, so that the local loading and induced velocity can be coupled. Whilst this can greatly improve the prediction of the inflow distribution in hover the model does not capture forward flight effects.

3.3.4.3 Uniform induced velocity in forward flight

The momentum theory can be extended to forward flight cases by redefining the control volume as shown in Figure 16. This takes into account the fact that the rotor in forward flight will require a nose-down pitch angle to provide a propulsive forward force. The method presented here is based on Leishman [2].
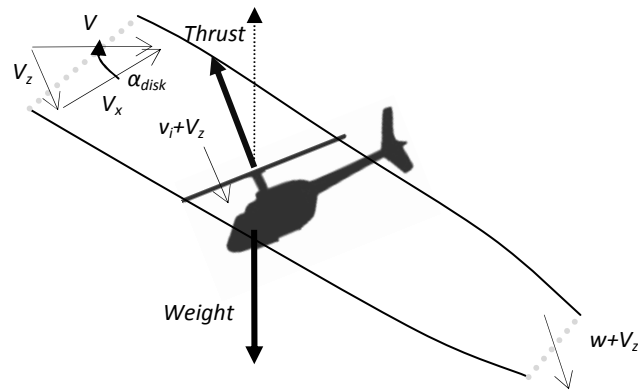
Figure 16: Control volume and Glauert flow model for the momentum theory in forward flight (based on Leishman [2])

Glauert (as shown in [2]) defines the resultant velocity at the disk as:

$$U_{disk} = \sqrt{(V_x)^2 + (V_z + v_i)^2}$$ Eq. 56)

Which leads to the mass flow through the disk as:

$$\dot{m} = \rho A_{disk} U_{disk}$$ Eq. 57)

The conservation of momentum can be applied in a direction normal to the rotor disk:

$$T = \dot{m}(w + V_z) - \dot{m}V_z = \dot{m}w$$ Eq. 58)

The conservation of energy yields:

$$P = T(v_i + V_z) = \frac{1}{2}\dot{m}(V_z + w)^2 - \frac{1}{2}\dot{m}V_z{}^2 = \frac{1}{2}\dot{m}(2V_z + w^2)$$ Eq. 59)

If conservation of momentum and energy are combined the relationship $v_i = {}^w/_2$ is the same as in hover [2]. Therefore the thrust can be expressed as:

$$T = 2\dot{m}v_i = 2\rho A_{disk} U_{disk} v_i = 2\rho A_{disk} v_i \sqrt{(V_x)^2 + (V_z + v_i)^2}$$ Eq. 60)

and rearranged for the induced velocity:

$$v_i = \frac{T/2\rho A_{disk}}{\sqrt{(V_x)^2 + (V_z + v_i)^2}}$$

Eq. 61)

For hover ($V_x = V_z = 0$) the above equation collapses to the same form as the induced velocity-thrust relationship for hover (presented in Eq 54). If used in an iterative loading-inflow ("outer loop") loop (Chapter 3.3.9) the equation above (Eq 61) provides a very useful relationship to obtain the induced velocity: The blade element method is used to calculate a new thrust estimate. For every new thrust estimate a new induced velocity is calculated.

Eq 61 itself is best solved using an iterative process ("inner iteration loop"). For this purpose the "successive overrelaxation method" [55] is used. It forms a weighted average between the previous and current estimate $\bar{v}_i^k$:

$$v_i^k = w\bar{v}_i^k + (1-w)v_i^{k-1}$$

Eq. 62)

Where *w* is the weighting factor which was set to 0.2 for the present study. The induced velocity in hover is used as an initial guess and can help to reduce the number of iterations required.

The forward flight momentum theory suffers from the same limitation as the simple hover momentum theory: It provides the disk-average uniform induced velocity, but does not capture any induced velocity variations along the radius. Furthermore, it does not capture any inflow distribution effects resulting from the shape of the rotor wake.

3.3.4.4 First harmonic inflow models for forward flight

The induced velocity distribution in forward flight is no longer axisymmetric, the blade loading is affected by the geometry of the rotor wake and the local inflow conditions can be difficult to predict. The performance of the rotor can, however, be approximated by a range of "first harmonic" (also called linear) inflow models [54] for the time-averaged induced velocity.

There is ambiguity in literature whether these models apply to low advance ratios from 0 to 0.15. Leishman [2] argues that the induced velocity was most non-uniform in this transition from hover to forward flight, strongly affected by the presence of discrete tip vortices and linear inflow models would hence only be valid for $\mu > 0.15$. Chen [56] provides an extensive review of first harmonic inflow models and shows satisfactory performance for advance ratio of 0.1 and lower.

The common basis for first harmonic inflow models is a simple relationship of the longitudinal and lateral inflow variation:

$$v_i = v_o\big(1 + k_x r cos\psi + k_y r sin\psi\big)$$

Eq. 63)

where v_o represents the disk average induced velocity from momentum theory and k_x and k_y are the gradients of the inflow in the longitudinal and lateral orientation. The inclusion of the radius term "r" introduces a variation along the radius, but in practice this is very small and not comparable to the radial inflow variation predicted by the Froude-Finsterwalder equation for hover.

First order inflow models are integrated into the blade element code as follows: First the disk average induced velocity v_o is obtained using inflow forward flight momentum theory and then the first harmonic model is used to obtain the inflow distribution on the disk. This inflow distribution is then used to obtain a new thrust estimate and this iterative process is repeated

until the thrust value has converged. Whilst this satisfies the conservation laws at a disk level it does not necessarily ensure that conservation laws are met on a blade element level.

Several first harmonic inflow models exist for k_x and k_y. An excellent survey and review of these models is given by Chen [54]. Three models were selected based on their good agreement with experimental data for advance ratios <0.1 and are presented in Table 3. For all values the inflow gains are 0 in hover and increase with flight speed.

χ in Table 3 describes the wake skew angle(using the mean inflow across disk) defined as:

$$\chi = tan^{-1}\left(\frac{\mu_x}{\mu_z + \lambda_i}\right)$$

Eq. 64)

which arises as the rotor wake is swept more rearwards with increasing forward flight speeds. The wake skew angle increases quickly from 0 to almost 90deg "in edgewise flight" [54].

Model name	K_x	K_y
Pitt-Peters (1981)*	$\left(\frac{15\pi}{32}\right)tan\left(\frac{\chi}{2}\right)$	0
Drees (1949)	$\frac{4}{3}(1 - 1.8\mu^2)tan\left(\frac{\chi}{2}\right)$	-2μ
Payne (1959)	$\dfrac{\left(^4/_3\right)tan\chi}{1.2 + tan\chi}$	0

Table 3: Overview of first harmonic inflow models selected for best low-speed performance according to [54], *only the static term is considered, there is also ambiguity about the /32 term which Leishman describes as /23.

Attention has to be drawn to the fact that literature suggests research on determining the parameters of the first harmonic inflow models was often done for a trimmed rotor in forward flight ([2], p159). Individual quadrotor rotors without cyclic pitch will, however, always be in an "untrimmed" state in forward flight. It is therefore unclear how well first order

harmonic models could capture typical quadrotor rotors and a comparison against experimental results is presented in Chapter 5.

3.3.5 A local-differential inflow model for hover and forward flight

3.3.5.1 Background

In the previous section two inflow models were discussed: The Froude-Finsterwalder formulation that captures the radial inflow variation in hover and provides a good radial distribution of hover blade loads, and first harmonic inflow models for forward flight which provide little inflow variation along the radius. A modelling challenge arises due to the discontinuity between the two models at low advance ratios. But it is exactly this low advance ratio regime that is most important to quadrotor operations. Furthermore, quadrotor rotors typically operate at high thrust coefficient, do not have ideal twist, and hence have a non-uniform radial inflow distribution, and are "untrimmed" in forward flight. In this section a simple local-differential inflow model is presented to approximate the inflow at low advance ratios and the limitations of the model are clearly highlighted.

3.3.5.2 Principles of the local-differential inflow model

A simple local-differential momentum theory is featured in Padfield ([7], p124) which applies the forward flight conservation laws at the blade element level rather than on a disk level. The present work applies this local-differential method to an iterative numerical blade element implementation, so that a nonlinear lift model and models for the rotor chord and pitch distribution can be used.

As shown in Figure 17 each blade element sweeps an area dA, which represents the 1/K (number of azimuth steps) slice of a disk annulus at radius r:

$$dA = \frac{2\pi r R_{max} dy}{K}$$

Eq. 65)

so that the $\sum dA = A_{disk}$. For the conservation of momentum the mass flow through dA is:

$$\dot{m}_{local} = \rho U_{local} dA \qquad\qquad \text{Eq. 66)}$$

where U_{local} represents the resultant velocity at each disk element given as:

$$U_{local} = \sqrt{V^2_{x\_local} + \left(V_{z\_local} + v_i\right)^2} \qquad\qquad \text{Eq. 67)}$$

and v_i is given as the local induced velocity on the blade element $v_i(r, \psi)$.

The forward flight momentum theory presented previously (Eq 61) can now be rewritten to express the relationship between the time-averaged total thrust dT produced on the local element and the local induced velocity:

$$v_i = \frac{dT/2\rho dA}{\sqrt{\left(V_{x\_local}\right)^2 + \left(V_{z\_local} + v_i\right)^2}} \qquad\qquad \text{Eq. 68)}$$

This equation is then solved iteratively for each blade element using the successive overrelaxation method ("Inner iteration loop") described previously. In hover the flow is axisymmetric and the formulation leads to the same results as the Froude-Finsterwalder radial inflow distribution.

Care has to be taken to correctly represent the time-averaged thrust produced by each blade element: The instantaneous thrust force dFz at each blade element has to be multiplied by the number of blades and averaged by the total number of azimuthal elements K:

$$dT = \frac{N_b dF_z}{K} \qquad\qquad \text{Eq. 69)}$$

Once the inner iteration loop has converged to a new v_i estimate this updated induced velocity is used to obtain a new estimate of the blade loading. This process is repeated until

the LOCAL blade element loading has converged. There can be strong oscillations in the outer

iteration loop and a method to stabilise the outer iteration scheme is introduced later on in

Chapter 3.3.9.
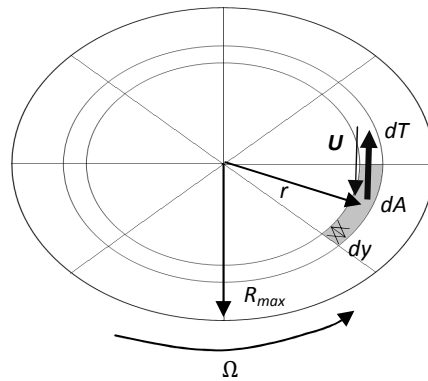
Figure 17: Control volume and annulus segment used in the local-differential momentum theory.

3.3.5.3 Assumptions and limitations of the local-differential inflow model

The local-differential blade element momentum theory makes the *"gross assumption that*

the relationship between the change in momentum and the work by the load across the

element applies locally as well as globally" ([7], p124). In doing so it assumes that all elements

are strictly independent. The induced velocity, acting perpendicular to the rotor plane is

assumed strictly 1-d and arises solely due to the time-averaged (1/rev) local thrust produced

over dA. All inflow effects due to a more complex wake structure and 3d effects are ignored

(with the exception of root and tip loss models discussed later).

The local-differential method presented here does, by no means, represent a complete

solution to the complex inflow problem in forward flight, but can be considered as a crude

low-order approximation which strength lies in providing a numerically continuous transition

from hover (Froude-Finsterwalder) to low-advance ratio (>0.15) cases in which other models

do not necessarily apply. It lends itself to a simple numerical (iterative) solution. Furthermore,

it is attractive for cases of highly loaded untrimmed rotors in which the radial inflow variation

has a stronger effect on local angles of attack (and hence thrust) than the longitudinal variation due to the wake shape.

3.3.6 The Mangler-Squire inflow model for forward flight

The Mangler-Squire model as presented in Leishman [2] is based on incompressible, linearized Euler equations and is hence a fundamentally different approach to the momentum-theory based solutions presented earlier on in this chapter. It allows a linear combination of two different types of loading:

- Type-1: elliptical loading.

- Type-3: loading that vanishes at the edges and centre of the disk.

The loadings can be combined using the weighting coefficients $w_1 + w_2 = 1$:

$$\Delta p = w_1 \Delta p_1 + w_2 \Delta p_2 \qquad \text{Eq. 70)}$$

A Fourier series is used to describe the inflow:

$$\lambda_i = \left(\frac{2C_T}{\mu}\right)\left[\frac{c_0}{2} + \sum_{n=1}^{\infty}(-1)^n c_n(r,\alpha)\cos(n\psi)\right] \qquad \text{Eq. 71)}$$

where the coefficients c depend on the type of loading, r and α (See *Appendix 1* for coefficients).

In the blade element method the Mangler-Squire method is used in an iterative process about the thrust coefficient C_T. An initial guess based on the hover C_T is used to obtain the Mangler-Squire inflow distribution. Using this distribution a new C_T is calculated and the process is repeated until the thrust coefficient has converged.

The main disadvantage of the Mangler-Squire method is that it contains high speed approximations [2] and that the model is therefore unsuitable (and numerically unstable) for advance ratios less than 0.1.

3.3.7 Induced rotational velocity (swirl)

Traditionally, momentum theory considers only the conservation of energy in one axis, whereas in practice the rotor torque adds rotational kinetic energy to the flow and gives rise to a "swirl" induced velocity. For typical helicopter rotors the swirl energy is considered small compared to the axial downwash energy ([9], p41) and is often "neglected as contributor to rotor power requirements" ([2], p69). Swirl is, however, reported to increase with thrust coefficient [2, 9] and could be more pronounced on quadrotor rotors operating at a higher C_T and a lower FoM than typical helicopter rotors. To decide whether swirl should be included two literature models for hover were used.

Johnson [9] presents an approximate model that considers the induced swirl in hover resulting from induced and profile torque due to the viscous drag of the blades:

$$u(r) = v_h \left[\frac{2v_h \Omega r}{(\Omega r)^2 + v_h{}^2} + 2\frac{C_d}{C_l} \right]$$

Eq. 72)

where the model is based on a uniform hover induced velocity vh and the Cd/Cl term is an effect of considering the profile drag. The function in Eq 72 peaks near the root at $u = v_h$ and then rapidly decays towards the tips. Leishman [2] presents a standard model for the wake rotational interference factor a' based on the generalized differential momentum theory:

$$(1 - a')a'r^2 = \lambda_i{}^2$$

Eq. 73)

Which can be solved analytically to obtain a' and hence the swirl velocity u(r):

$$a' = 0.5 - 0.5\sqrt{1 - 4\left(\frac{\lambda_i}{r}\right)^2}$$

<div align="right">Eq. 74)</div>

$$u(r) = a'r(\Omega R_{max})$$

<div align="right">Eq. 75)</div>

It has to be noted that this numerical solution only applies to radial stations sufficiently far away from the root to ensure a positive term in the square root of Equation 74. Both models appear to be only valid for hover cases and cannot be readily applied to forward flight studies in which the flow is no longer axisymmetric.

The simple swirl model from Leishman was used to study the effects on a variable-pitch rotor operating at constant disk loading (thrust T=2.5 N). For each pitch angle the rotational speed was updated to ensure constant disk loading. Swirl was found to be most pronounced near the root which has only a limited aerodynamic contribution. The addition of swirl adds around 1% of total power for typical operating conditions (10 deg collective) and effects appear to remain below 3% for high C_T cases. Given the limited impact of swirl on power and the modelling uncertainties and difficulties in forward flight it was decided not to include swirl into the baseline blade element model.

3.3.8 Tip and root loss model

The blade element method treats every blade element as an independent 2d airfoil. Whilst this assumption appears valid for large parts of the blade it breaks down near the root and especially near the tips where 3d effects ("tip losses") take place. Those effects cannot be captured by simple blade element momentum theory and additional models for root and tip losses are required.

The tip losses are modelled using the well known Prandtl tip loss model [2, 57]:

$$F_{TIP\_LOSS} = \frac{2}{\pi} cos^{-1} e^{-f}$$

Eq. 76)

$$f = \frac{N_b}{2} \frac{1-r}{rsin\phi}$$

Eq. 77)

which approximates the tip loss effects along the radius. The tip loss correction F_{TIP_LOSS} is then applied to increase the local induced velocity as:

$$v_i = \frac{v_i}{F_{TIP\_LOSS}}$$

Eq. 78)

This is included in every iteration step and was shown to converge rapidly.

Whilst a similar model exists for the root losses it was found that the low lift loadings and extreme numerical fluctuations in the inflow angle often made root loss models unstable. Root losses are hence modelled using a simple root cut out (10% of the radius for the blades used in this study). Within the root cutout region it is assumed that a blade element cannot produce any lift, but is capable of producing drag.

3.3.9 An iteration scheme to stabilise the inflow iteration loops

3.3.9.1 The problem of oscillations in the inflow angle

The relationship between local induced velocity, angle of attack and thrust was discussed previously in this thesis. The numerical (iterative) solution process can often be unstable, because a large angle of attack can lead to high local loading which results in a large local induced velocity. This large induced velocity subsequently causes a large inflow angle and results in a negative angle of attack. The outer-loop iterations can become unstable and diverge.

There are well-known iteration schemes to damp strong numerical fluctuations in the iteration values that work by taken a weighted average between the current and previous

iterations, such as the successive over-relaxation discussed previously. But in many cases, especially in hover and for regions near the root, either the previous or the current estimate could be extreme and lead to non-converging oscillations which cannot be stabilised by a universal weighting factor w. To overcome this convergence problem a multi-step iteration scheme is proposed as a novel contribution to the local-differential blade element method.

3.3.9.2 A multi-step iteration scheme

The key idea of the multi-step iteration scheme is that it uses up to $k - n_{multistep}$ previous iteration steps to stabilise the iterations, rather than just using the current and previous iteration step.

The local blade loading distribution $dF_z(\psi, r)$ is stored in a 2d matrix of radial and azimuthal position. In the multi-step method a 3rd dimension for the history of iterations is added to represent the $dF_z(\psi, r)$ 2d matrix for each iteration step k. The maximum length of the 3rd dimension is defined as $n_{multistep}$. As long as the number of the current iteration is $k < n_{multistep}$ the 3d matrix keeps growing in the 3rd direction. Once $k > n_{multistep}$ all iterations "older" than $n_{multistep}$ are truncated.

The local induced velocity $v_i(\psi, r)$ is now calculated based on the average of $dF_z(\psi, r)$ over the previous n_multistep (or k if $k < n_{multistep}$) steps using the inner iteration loop and the successive overrelaxation method described in Chapter 3.3.4.3. The revised inflow estimate results in a new $dF_z(\psi, r)$ estimate. The multi-step method stabilises the iteration loop, because extreme oscillations are initially averaged to more moderate loading cases which can stop the initial divergence and improve convergence at later iteration steps.

The convergence of the multi-step ("outer loop") iteration scheme is defined as follows: If the loading estimate produces an induced velocity field which then then, after applying all blade element calculation steps, results in a loading estimate within a certain tolerance of the

previous loading estimate. The converged result presents a unique solution for the given flight conditions and blade model and satisfies the local conservation of momentum, energy and mass at the local blade elements. In numerical tests the solution appeared independent of the initial guess, providing the initial guess was of the right sign and within similar orders of magnitude to the solution.

Whilst the multi-step method appears to improve convergence by damping extreme loading and inflow fluctuations, the convergence at every local element cannot be guaranteed universally. To avoid infinite loops a maximum number of outer-loop iterations is set at which the loop is broken. In this case the global thrust and power convergence is checked. It was found that convergence could further be improved if infinitesimally small forward flight speeds were added or a root-cut out are used.

It is acknowledged that no theoretical framework yet exists for proving universal convergence criteria for the multi-step method and that this multi-step method increases computational effort. However, it was found to be a useful addition to the local-differential blade element theory. The performance of the method was studied using numerical experiments and force and moment results are then compared against experimental thrust results in Chapter 5.

3.3.10 Numerical setup and sensitivity

A numerical study was conducted to determine the convergence of the different modelling choices as well as the optimum element distribution, number of element and length $n_{multistep}$ of the multi-step iteration scheme.

First, the number of radial elements M is studied for the axisymmetric hover case. The variable pitch rotor (Chapter 4.2.4) was used as baseline case and both equal radius and equal area approaches were studied for the local-differential inflow model (Figure 18) as well as the

uniform inflow model (Figure 19). Given the simplicity of the inflow model, no significant benefits could be obtained from the equal area approach and hence the equal-radius approach was used for the rest of the study. As expected, the uniform inflow model requires significantly fewer elements to achieve grid-independent results. From about 30 elements both solutions become independent of the element number and M=30 was fixed for all flight cases.

Next the sensitivity to the number azimuthal stations K is studied for a rotor in forward flight. Results are presented for three different inflow models and at two advance ratios. A value of K=16 was found to allow grid-independent results for all inflow models and ensure elements are positioned on the advancing and retreating side of the blade. It has to be noted that results for $\mu = 0.1$ are strongly affected by the poor low-speed performance of the Mangler & Squire method.

Results for the multi-step iteration methods are presented for hover (Figure 21 a)) and forward flight (Figure 22). In hover it appears that results can be unstable below a certain number of steps and $n_{multistep}$ was set to 30 to ensure convergence in hover and forward flight. The number of iterations required for convergence is larger than for the Mangler&Squire method (Figure 21b).

A study of the radial thrust distribution (Figure 23) shows little thrust is produced near the root region and that a root cut-out of 10% would have a negligible effect on thrust.

All relevant blade element settings from this study are summarised in Table 4.

a)

b)
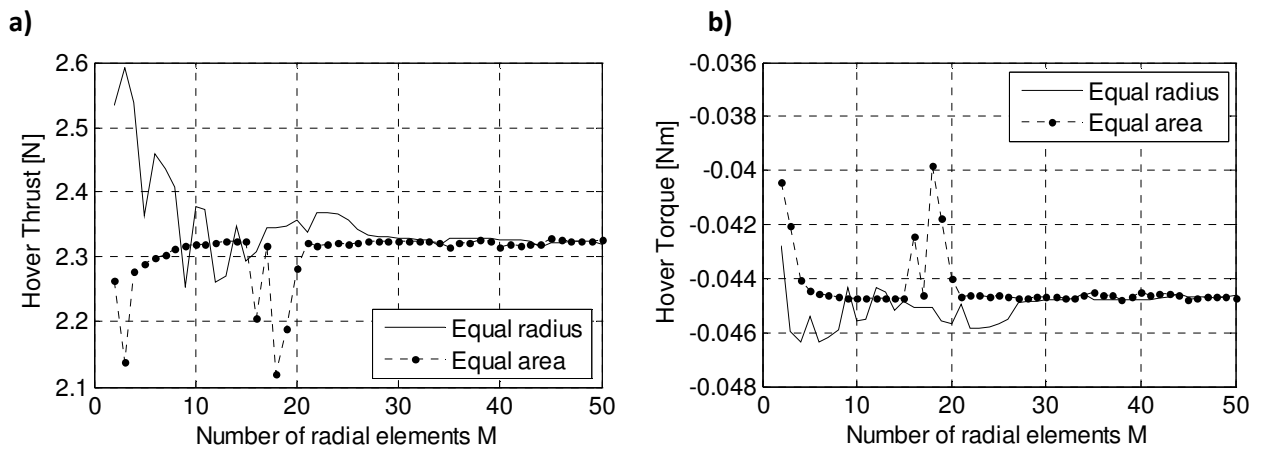
Figure 18: Effect of the number of radial elements on thrust and torque convergence in hover – local-differential inflow model.

a)

b)
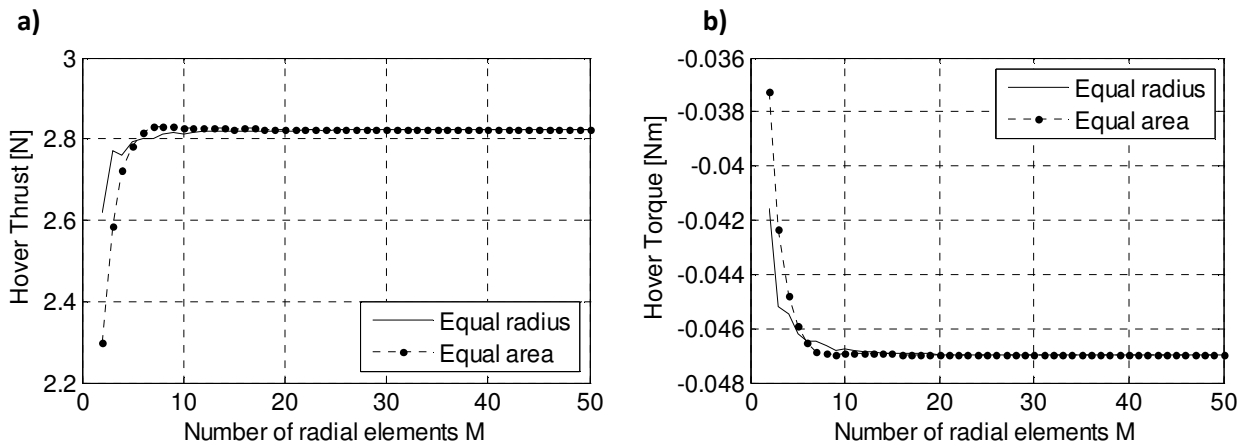
Figure 19: Effect of the number of radial elements on thrust and torque convergence in hover – uniform inflow model.

a)

b)
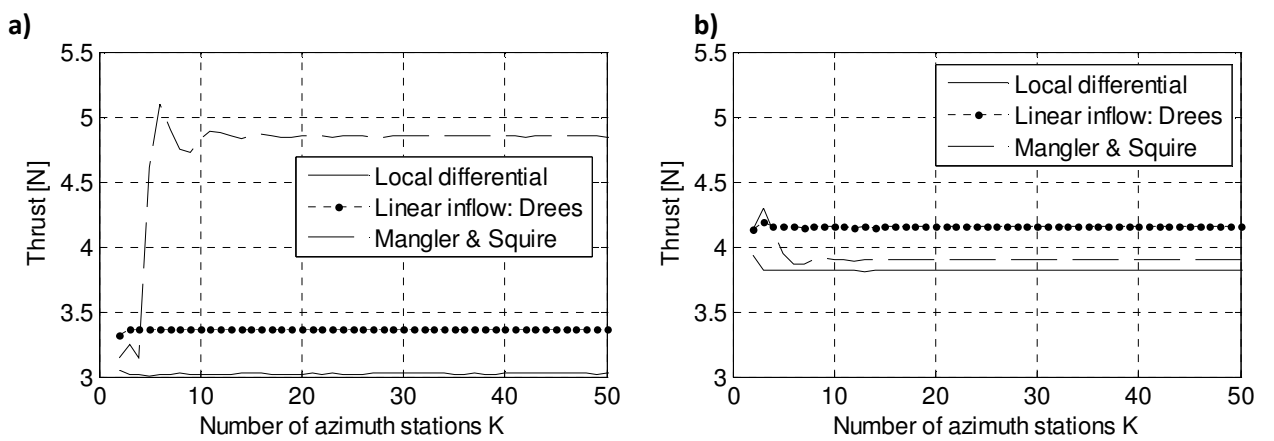
Figure 20: Effect of the number of azimuth stations on thrust a) mu = 0.1, b) mu = 0.2 (both at -5 deg disk angle of attack).

85
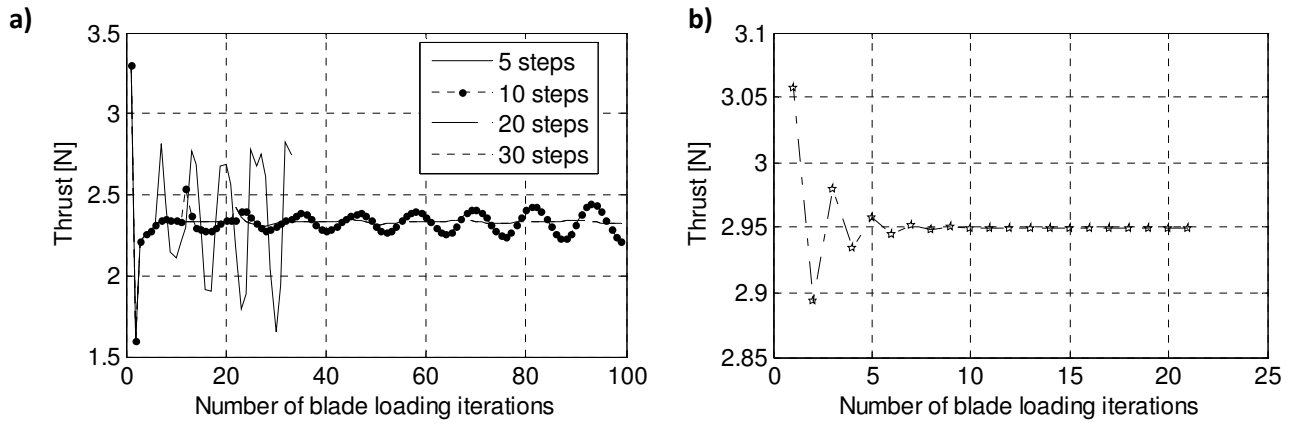
Figure 21: a) Effect of the number of stabilisation steps in the dt loading and convergence with number of blade loading iterations (with root cut out) b) convergence of the Mangler-Squire model at μ=0.2, AoA 15 deg, 5000 rpm, 10 deg pitch
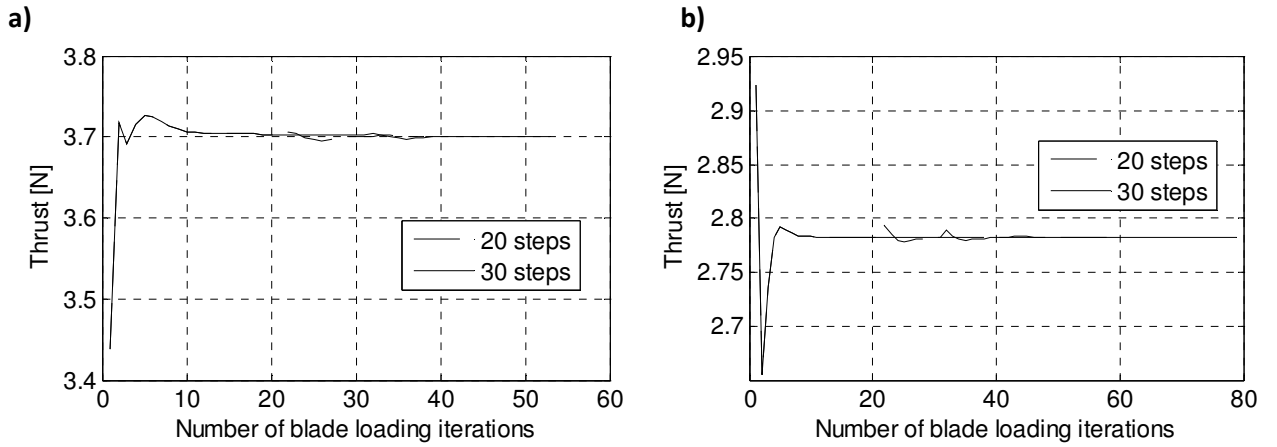
Figure 22: Effect of the number of stabilisation steps on the local-differential model in forward flight (with root cutout), a) mu 0.2, disk AOA 5 deg, b) mu 0.2, disk AoA 15 deg.
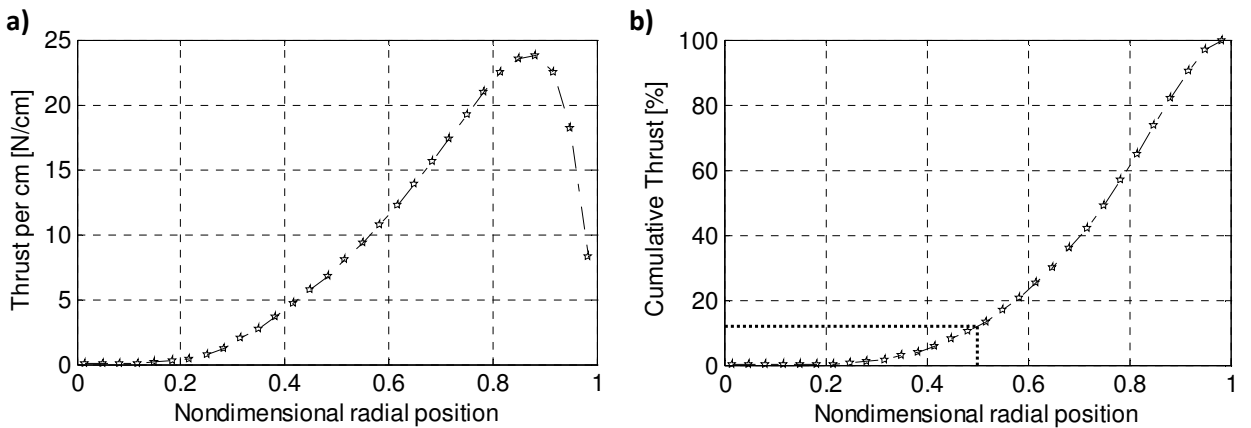
Figure 23: Spanwise loading distribution on a blade in hover (10 deg pitch, 5000 rpm) a) thrust per unit, b) cumulative thrust produced up to the radius specified.

Parameter	Value
Number of radial elements M	30
Number of azimuth stations K	16
Inflow convergence criterion	0.05%
Blade loading convergence criterion	0.05%
dt-history matrix length (Local-differential BEMT)	30
Root cut out region	0.1 R
Swirl velocity	Off
Tip loss model	Prandtl tip loss – modelled on induced velocity

Table 4: Table of blade element simulation parameters.

3.4 Airframe aerodynamic model

In previous literature on quadrotors and other miniature rotorcraft, the fuselage aerodynamics are largely ignored and the full characterisation of fuselage aerodynamics is, in fact, a formidable undertaking that requires extensive wind-tunnel or computational CFD study beyond the scope of this study. In this research a simple semi-empirical model for the purpose of performance analysis and flight mechanics is presented.

Given the large vehicle angles of attack experienced by quadrotors in forward flight an aerodynamic model based on forward "drag" alone is not sufficient. A distinction is made between "fuselage frontal drag area" and "fuselage vertical drag area" [12] and a model has to be formulated to capture arbitrary vehicle angle of attack, so that the model could find application in future gust response studies of quadrotors. The fuselage is assumed symmetric (no side force, rolling or yawing moments) and the pitching moment is considered negligible.

To avoid ambiguities about the definition of reference areas the standard helicopter convention of expressing data as equivalent flat plate areas in m^2 (with $C_D = 1$) is used. From geometry it is hypothesised that fuselage axial and normal force coefficients in body axes can be expressed by sine and cosine functions of the vehicle angle of attack:

$$CF_{x\_body} = kCF_x \cos(\alpha_{vehicle})$$

Eq. 79)

$$CF_{z\_body} = kCF_z \sin(\alpha_{vehicle})$$

Eq. 80)

Where kCF_x and kCF_z are design-dependent coefficients identified from windtunnel experiments at 0 and 90 deg vehicle angle of attack. For the first order model the fuselage forces are assumed to act at the geometric centre of the vehicle and experimental results for the centre of pressure location are presented later on in Chapter 6.2.3. The force coefficients can be expressed in absolute forces by multiplying the coefficients with the dynamic pressure $\frac{1}{2}\rho U^2$ and can be expressed in wind or earth axes using Euler rotations about the y_{body} axis.

Windtunnel experiments to determine the coefficients kCF_x and kCF_z for different quadrotor fuselages are presented in Chapter 4 and the performance of the model is evaluated in Chapter 6.2.3. Given the lack of models and data available in literature this semi-empirical model, despite being highly simplified, presents a useful addition to future research quadrotor flight.

3.5 First order electric motor and battery models

With electric propulsion broader rpm changes become feasible and the power-plant efficiency has to be monitored as a function of rotational speed, torque and motor design. In this section the key aspects of low-order models for electric motor and battery losses [24, 58] from literature are presented. This is largely based on Mark Drela's qprop model [58]. Parts of the following section have been included in one of the author's previous publication [59].

3.5.1 DC Motor modelling

It is proposed to model the motor system using a standard 1st order DC motor model, such as the one presented by Drela [58] and in previous quadrotor design projects [24], including slight modifications to account for the particular nature of brushless motors.

The key argument for using a first order model was that only three rotor parameters are necessary to provide an initial model for electric power consumption, current draw and electric efficiency. Since the three required parameters are generally available for different motors the method can be used without the need for extensive experimental motor characterization and is hence well suited for a generic simulation environment.

The three required rotor parameters are:

- K_V: motor speed constant relating rotational speed to applied voltage [rpm/V]

- i_0:   no load current [A]

- R: internal motor resistance [Ω]

Using a set of simple equations these parameters can be related to the motor torque, rotational speed, power and efficiency:

Motor torque

$$Q_m(i) = \frac{(i - i_0)}{K_V}$$

Eq. 81)

Rotational speed

$$\Omega(i, v) = (v - iR)K_V$$

Eq. 82)

Shaft power

$$P_{shaft}(i, v) = Q_m\Omega = (i - i_0)(v - iR)$$

Eq. 83)

Electric power

$$P_{elec}(i, v) = vi$$

Eq. 84)

Electric efficiency

$$\eta_{elec}(i,v) = \frac{P_{shaft}}{P_{elec}} = \frac{1 - \frac{i_0}{i}}{1 - \frac{iR}{v}}$$

Eq. 85)

The above equations can then be used to obtain the electric power and efficiency for a given rotational speed and torque from the blade element model. Since brushless motors vary the signal on/off timing rather than the voltage magnitude the v and i terms in equations 81-85 have to be classed as auxiliary terms and do not represent the actual, instantaneous voltage and current applied. Their product, however, is assumed to remain valid, so that the model still applies to the prediction of electric power and mechanical-to-electrical efficiency η_{elec}.

The performance of this simple model is compared against experimental data in Chapter 6, where practical solutions for modelling improvements are presented.

3.5.2 Rudimentary battery modelling

Most electric UAVs use lithium based batteries as their power supply for their high energy density and low cost. Five aspects have to be considered in a first order model for the battery system: The voltage drop for an applied load current, the voltage drop with battery discharge, the losses for a given load, the energy density of the system and the maximum discharge rate.

The battery voltage drop ΔV for a given current draw I_b can be approximated using the battery's internal resistance R_b [24] as provided by the manufacturer:

$$R_b = \frac{\Delta V}{I_b}$$

Eq. 86)

The power losses due to battery losses for a given load I_b can be approximated as:

$$P_{LOSS_{BATTERY}} = R_b I_b^2$$

Eq. 87)

Where the crude approximation is made that R_b remains constant for a particular battery. In practice R_b varies with battery current as shown in [24], but requires additional modelling parameters beyond readily available manufacturer data.

The battery voltage drop with battery discharge is either taken from published battery data or approximated using the lithium-ion battery model in Matlab's simulink toolbox [60]. In practice the voltage drop is expected to have limited effects on quadrotor flight performance, providing the battery is suitably sized for the expected maximum loads.

The energy density of the power storage system plays a critical role in the preliminary design process, because it allows for the optimum battery sizing for performance optimization. Further to the battery capacity the maximum discharge rate for the power storage solution has to be considered at an early stage. Both energy density and discharge rate, are implemented into the simulation by using lookup-tables based on commercially available systems.

Chapter 4: Experimental Methods

The objectives of this chapter are to:

Obtain repeatable and accurate time-averaged, steady-state measurement data on the hover and forward flight performance of electrically-driven small scale-rotors and quadrotor vehicles. The contribution presented in this chapter is a method for quadrotor forward flight trim and interference analysis.

4.1 Chapter overview

Understanding quadrotor forward flight requires data on single rotor performance, rotor-rotor interference, fuselage aerodynamics and forward flight trim settings. Experimental data on this has previously not been available for quadrotor vehicles and experiments from helicopter literature often do not apply for reasons discussed in Chapter 1. The focus of the experimental methods and procedures described in this chapter is to provide a broad range of data to improve the understanding of quadrotor flight performance:

- Single rotor experiments on fixed and variable pitch rotors are described first. A large range of airspeeds, disk angles of attack, rotor speeds and collective pitch settings was studied and the three components of forces/moments and power demands were measured.

- To study previously unknown rotor-rotor interference effects, an adjustable rotor-spacing test-rig was designed. Interference effects for different rotor spacings and vehicle flight configurations ("x" and "+") were studied along the previously defined forward flight trim-conditions.

- Fuselage aerodynamics are measured on two different quadrotor airframes, typical for many operational quadrotors in the 1 kg class. Forces and moments were measured for a 180 deg range of angles of attack to provide a useful dataset

for the creation of airframe models and further research into quadrotor gust response.

- Forward flight trim and power curves are a key element of understanding maximum speed and energy efficient flight conditions. No literature values were available at the time of writing and obtaining reliable data from flight testing is difficult because even small ambient wind speeds can be significant compared to the vehicle flight speed. A solution is presented in the form of a closed-loop trim method using force balance feedback.

4.2 Experimental Apparatus

4.2.1 The Project wind tunnel

All wind tunnel experiments were conducted in the University of Manchester's "Project Tunnel", an open circuit blow down wind tunnel with a 0.9 m by 1.1 m test section and a turbulence level of 0.5 % [61]. All test subjects were mounted vertically on an L-shaped support strut coming from the ceiling of the tunnel (Figure 26) and could be rotated with respect to the freestream flow by using the tunnel's 360deg overhead yaw turntable. The strut was sized and orientated to keep the model centred in the test section.

The maximum velocity of the project tunnel is 50 m/s, but for these research experiments a range of velocities from 3 to 25 m/s were used. The tunnel velocity was measured using pressure tapings at the beginning and end of the contracting cone. For calibration cases a pitot-static probe in the test section upstream of the model was also used.

At the time of writing the project tunnel was the largest wind tunnel available at Manchester University and the test specimen had to be chosen considering the ratio of the rotor disk area to the cross sectional area of the tunnel test section. This was a trade off

between a sufficiently small ratio to reduce potential tunnel interference effects, and sufficiently large rotors to allow for forces within a measurable range for the available force balances and to capture representative Reynolds numbers.

Table 5 shows the rotor size and tunnel cross sectional area for classic tandem rotor experiments [62, 63]. It also shows that the quadrotor test arrangement used in this study has a significantly smaller total disk area to tunnel area ratio.

Experiment	Rotor radius [m]	Test section size	A_{disks}/A_{tunnel}
Dingeldein,1954	2 x 2.286	18.2 x 9.1 m(60x30 ft)	0.20
Halliday & Cox, 1961	2 x 0.645	2.7 x 2.1 m(9x7 ft)	0.45
Langkamp, 2011	4 x 0.102	0.9 x 1.1 m	0.13

Table 5: Comparison of rotor disk and tunnel area ratios from classic tandem rotor experiments [62, 63] and the present quadrotor study.

Based on these sizing considerations all multi-rotor experiments were conducted on full-sized 8 inch diameter rotors, and single rotor tests were carried out on 8 and 10 inch diameter rotors.

4.2.2 Sensors, DAQ system and electronics

The data acquisition (DAQ), electronics and sensor setup is illustrated in Figure 24 and shows the system's four key features: Power supply, sensor inputs, signal processing and command outputs.

A "Lambda Gen 30-50" adjustable voltage regulated desk power supply is used to provide up to 64 Amps of DC current to test specimen motors. The power supply can be current limited and the RMS current is displayed on a digital indicator. Separate 5V and 15V DC power supply units were used for the sensors and model actuators. All power supplies and data acquisition grounds were connected to prevent ground loops.
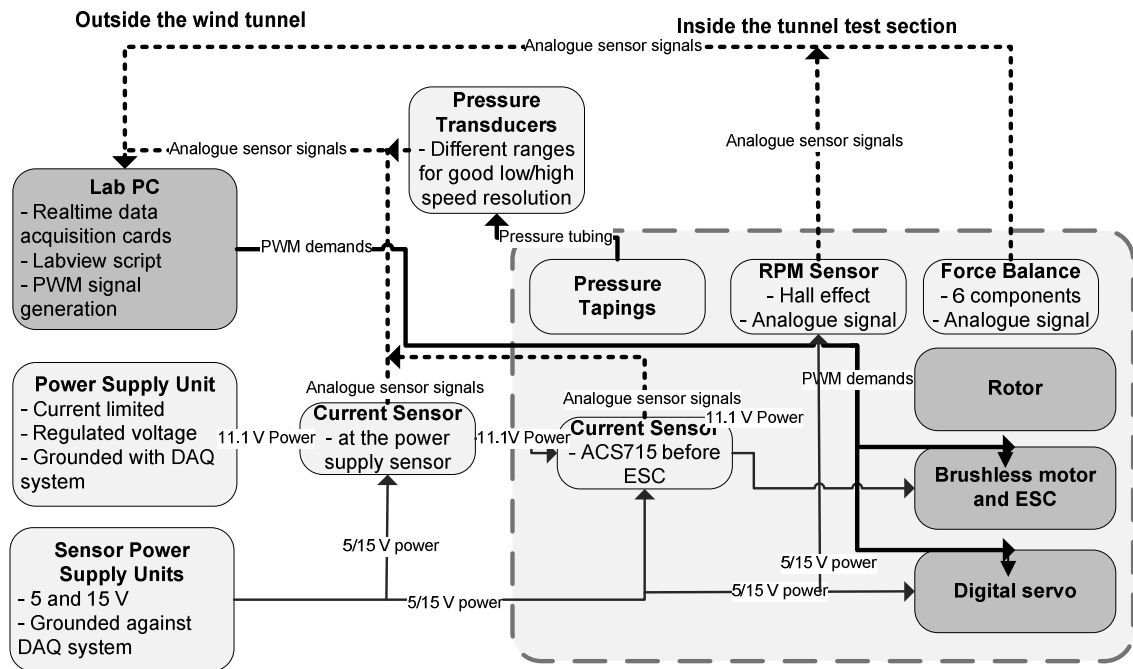
Figure 24: Data aquisition and control setup used for the experiments.

Three pressure transducers were used for the tunnel speed measurements. The standard low speed wind tunnel practice of measuring the pressure change across the tunnel contraction was used [64] as the primary tunnel speed measurement. One static pressure port was located in the settling chamber downwind of the honeycomb arrangement and another static pressure port was located downstream of the contraction in front of the test section. At low speeds a low range SENSIRION - SDP1000-L05 (up to about 150 Pa) was used to reduce uncertainty, whilst a higher range HCXM020D6V sensor (2000 Pa range) was used to provide the required range at higher speeds. A factory calibrated "Furness Control" transducer was used for an additional Pitot-static tube at the beginning of the test section about 1 m upstream of the model. All pressure tapings were connecting to the transducers using pressure tubing which was sealed and checked for leaks.

Hamlin 55100 (3M02A) hall effect sensors were used as the primary rotor RPM sensors. They were mounted in close proximity to the rotating part of the outrunner brushless motors within 2-3 mm of a 0.1 g magnet attached on the outside of the rotating motor casing. A

potential-divider circuit was used to flip the sensor voltage between 0 and 5 V every time the

magnet passed the sensor in the correct polarity (a typical signal is shown in Figure 35). The

signal was time stamped and could be used to reconstruct the rpm through post-processing or

the internal counter/time function of the DAQ system.

Electric current was measured using two different sensors: one non-invasive LEM LA 55-P

for a 70 A current range was placed near the power supply unit outside the test section, and

for multi-rotor experiments, one ACS715 current sensor with a 0-30 A range was in the power

supply line of each individual motor. The ACS715 sensors were placed in the tunnel test

section and aligned as to reduce mutual electrical interference as well as the total blockage.

All force measurements were conducted with a small-scale 6-component ATI-mini force

balance inside the tunnel test section. The balance had a diameter of 40 mm and was mounted

between the support strut and the model centre. For quadrotor interference studies the

balance was mounted underneath individual rotors. The balance was positioned to minimize

blockage effects and aligned so that the hover thrust vector runs through the balance moment

centre. The selection of a suitably sized multi-axes force balance measurement range was a

trade-off between handling significant moments in the quadrotor trim studies and the

measurement uncertainty for smaller side forces, such as rotor drag, in single rotor

experiments. The ATI-mini was found to be an acceptable compromise and the implications of

the measurement range on uncertainty are discussed in Chapter 4.5.

Balance range				Balance resolution			
F_x,F_y [N]	F_z [N]	T_x,T_y [Nm]	T_z [Nm]	F_x,F_y [N]	F_z [N]	T_x,T_y [Nm]	T_z [Nm]
20	60	1	1	1/200	1/100	1/8000	1/8000

Table 6: Force balance range and resolution (at the finest calibration).

All signals were read into National Instruments PCI data acquisition cards and processed in the Labview environment where scripts were created for the timing, scheduling and recording of measurements and motor/rotor command signals.

Output signals to change collective pitch and motor rpm were sent in the form of pulse width modulated (PWM) signals created using the internal counter/timers on the DAQ cards or a Pololu serial to PWM converter. The PWM signal was then interpreted by the brushless electric speed controllers (mainly Align RCE-BL25g, max current 25 A) to change the rotational speed and by digital servos to affect a change in collective pitch.

4.2.3 Fixed pitch single rotor setup

For single rotor wind tunnel tests a brushless motor was mounted onto to the force-balance using a small motor bracket. Using an L-shaped support strut from the top of the wind-tunnel the assembly was positioned to align the centre of the rotor plane with the centre of the test-section.

An Axi 2208/20 EVP brushless motor was used in direct drive mode eliminating the need for a gearbox. The motor was chosen for its low variability in motor properties and its large practical rpm range (up to about 10000 rpm with the APC 8x3.8 propellers) that enabled the author to study a wider advance ratio range.

A "propeller adaptor" was used to securely clamp the propeller onto the rotor main shaft and create a hingeless rotor system. Commercial off-the-shelf APC 8x3.8 propellers, such as typically found on open source quadrotors (Aeroquad) and commercial (AscTec), were used as test-specimen. The propeller tests were conducted with clockwise and anticlockwise APC 8x3.8 propellers of 0.1016 m radius and 0.1044 solidity (total blade area over disk area).
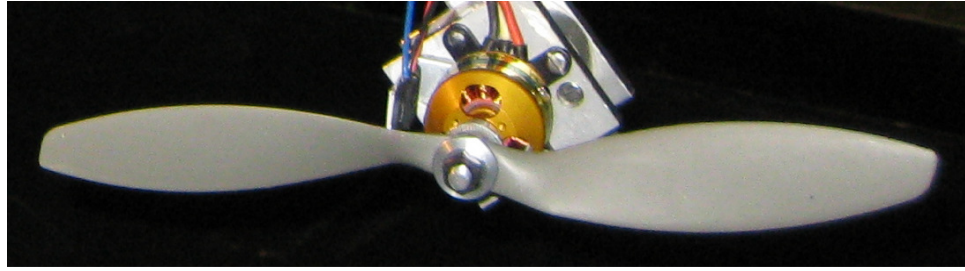
Figure 25: An APC 8x3.8 rotor on a AXI 2208/20 EVP motor, attached to the shaft using a propeller adaptor.

4.2.4 Variable pitch single rotor setup

The variable pitch single rotor setup was mounted in the tunnel in a similar way to the fixed-pitch setup. A channel-section bracket was designed to accommodate the pitch actuation mechanism on the measurement side of the force balance. The drag created on the assembly was corrected for in the measurement results (see Chapter 5).
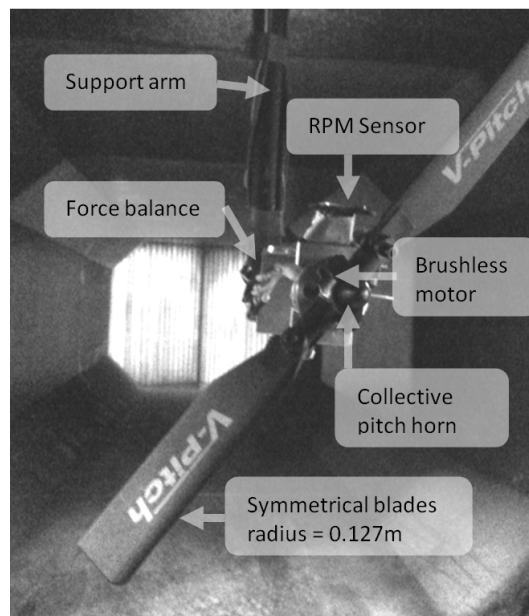
Figure 26: Variable pitch wind tunnel test rig with force balance and rpm sensor (rotor diameter = 254 mm).

A commercial off-the-shelf variable pitch system, as typically found on fixed wing 'shock' flyer model aircraft, was used as the test article. The system was driven by a "Rimfire" brushless motor with a hollow main shaft. The collective pitch mechanism was based on a simple pitch linkage rod run through the hollow main shaft, thus avoiding the need for a swashplate. A digital servo underneath the brushless motor was used to drive the mechanism.
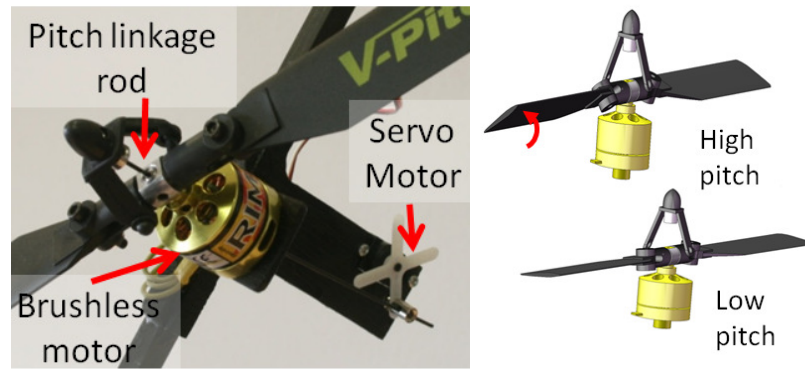
Figure 27: Close up view on the EVP collective pitch mechanism

A hingeless rotor with a 0.127 m radius and solidity of 0.099 was used. The blades were symmetrical and untwisted with a constant chord between 40-100% radius. The Reynolds number at ¾ radius varied between 20000 – 130000. The thickness to chord ratio was measured as 12%.

4.2.5 An adjustable quadrotor test-rig

To study the effect of rotor spacing and vehicle configuration ("x" or "+") on quadrotor forward flight performance a dedicated test-rig was constructed. As for the single rotor tests the model was mounted vertically and the vehicle's angle of attack could be changed using the tunnel overhead yaw turntable.

The quadrotor test-rig as shown in Figure 29 allowed mounting the motors at four different positions from the centre of the frame, equivalent to rotor-rotor spacings of d/D = 1.03, 1.1, 1.2 and 1.3. The test-rig also allowed changing between an "x" and "+" flight orientation.
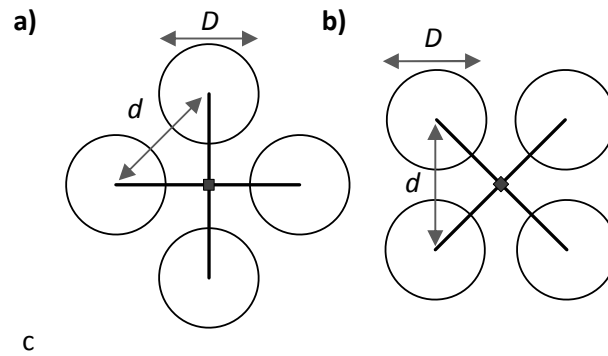
Figure 28: Definition of the rotor spacing d/D in the "+" and "x" configuration.

The rotors were arranged in pairs of clockwise and anticlockwise rotors and in one rotor plane parallel to the airframe, as it would be the case on a flying quadrotor. To reduce the number of measurement parameters and calibrations the same fixed-pitch APC 8x3.8 inch rotors and Axi 2208/20 EVP motor combination as in the single fixed-pitch rotor testing were used. The selected motors are not a typical selection for quadrotor vehicle that is optimized for hover efficiency; instead they were selected for their good manufacturing repeatability and a large practical rpm range that allowed extending the range of advance ratios studied. The motor speed controllers were mounted on the support strut behind the force balance to reduce additional drag and interference on the measurement side of the force balance

All motors were equipped with current and rpm sensors as described in Chapter 4.2.2. The force balance could be placed in two ways:

- Underneath the centre of the test-rig frame, between the model and the support strut, in order to measure the total vehicle forces and moments and obtain the forward flight trim curves.
- Underneath one of these individual rotor mounts to measure the individual rotor forces and moments and interference effects.

The motor mounts and the central plate were designed to accommodate the required sensors and mounting points for changing the flight orientations. It is appreciated that the

frame itself could lead to substantial parasite body drag and this is being considered in the experimental procedure and the analysis of the results.
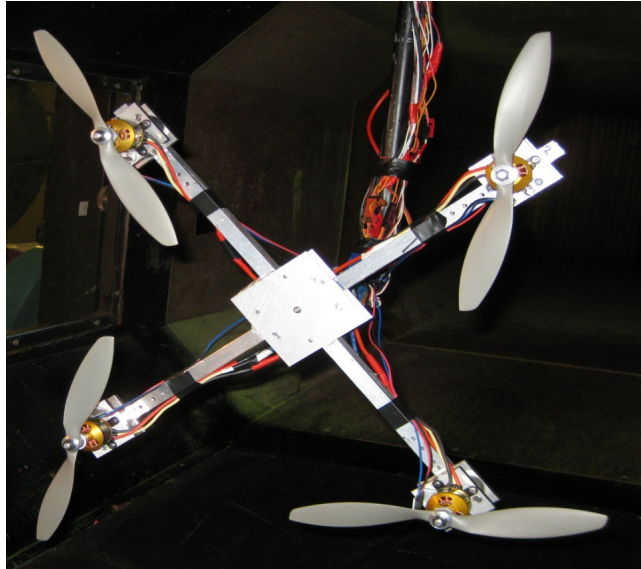
Figure 29: Quadrotor test-rig with adjustable rotor spacing, flight orientation and force balance position.

4.2.6 Body drag measurement setup

The body drag of two different quadrotor platforms was measured: A Draganflyer V and an Aeroquad ("Kinjal Carbon Fiber Frame"). These frames were chosen because they are suitably sized for the project tunnel and because they represent two contrasting airframe designs typical for quadrotors:

- The Draganflyer is a streamlined design and relatively clean configuration with a canopy above the electronics bay and without exposed wires.

- The Aeroquad design is typical for quadrotors used in many research projects: the electronics bay, speed controllers and wires are exposed; there is no streamlined preferred flight direction and the frame booms are arranged in flat plates as opposed to circular rods.

Both quadrotors were mounted in the tunnel in a vertical orientation (see Figure 30) using an L-shaped support strut from the overhead yaw turn table. To allow for attaching the models

directly to the ATI-mini force balance without modifying the vehicle geometry, reinforced battery trays for each vehicle were constructed that were geometrically identical to the original battery trays. For both quadrotors the body drag measurements were conducted without rotor blades.

Given the complex geometry it was decided to take force measurements only from the internal force balance and not to use any additional wake pressure data.

a)   b)
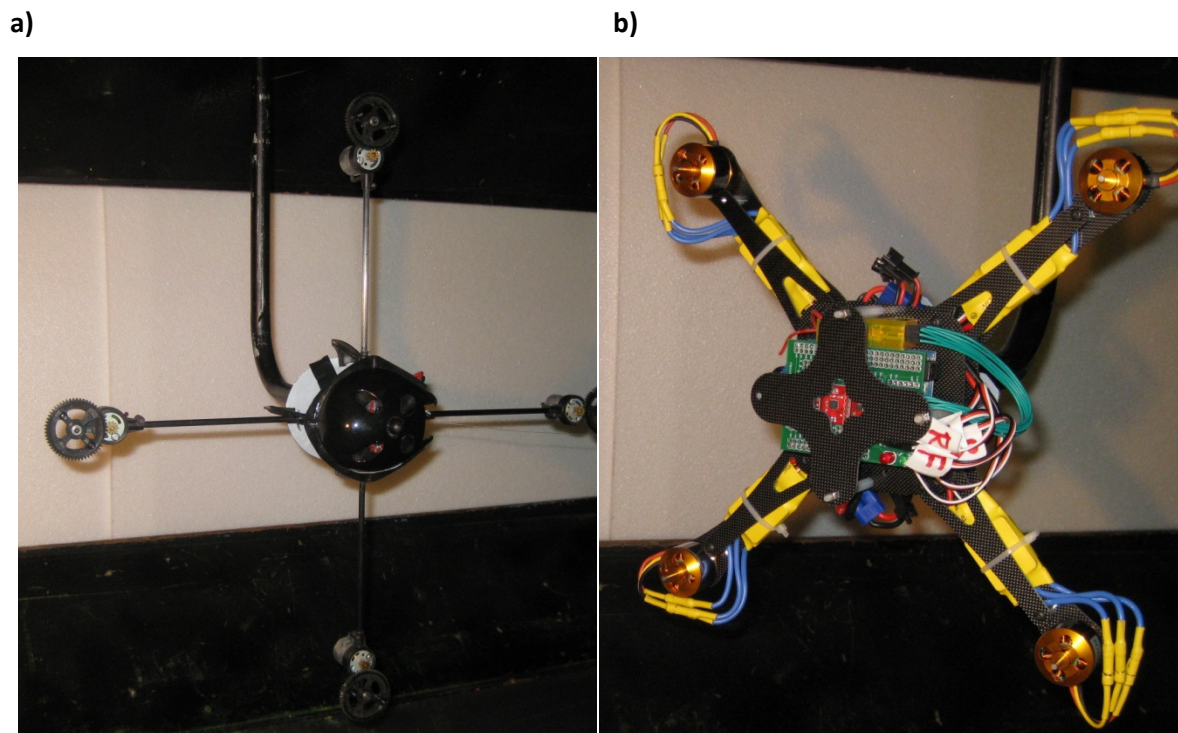
Figure 30: Quadrotor body drag measurement setup. Draganflyer (a) with 46.5 cm rotor-rotor distance and Aeroquad (b) with 31.5 cm rotor-rotor distance.

Single rotor setup *0.25 m rotor diameter*	*Adjustable test-rig in + configuration* *d/D = 1.2, 0.2 m rotor diameter*
Front view: Rotor in pure climb (α_{disk} = -90°)	**Front view: Vehicle in pure climb (α_{disk} = -90°)**

Side view: Rotor in pure climb (α_{disk} = -90°)	**Side view: Vehicle in pure climb (α_{disk} = -90°)** **(only "top" and "bottom" rotor shown for clarity)**

Top view: Rotor in forward flight (α_{disk} = 0°)	**Top view: Vehicle in forward flight (α_{disk} = 0°)**

Top view: Rotor in forward flight (α_{disk} = -45°)	**Top view: Vehicle in forward flight (α_{disk} = -45°)**

Figure 31: Schematic sketch of single rotor and adjustable test-rig setup in the wind tunnel test section.

4.3 Experimental Procedure

4.3.1 Calibrations and biasing

For the purpose of this study the factory calibration and biasing of current, rpm and force

sensors had to be validated and new calibrations had to be created for the collective pitch

angle and the tunnel speed.

For the hall-effect current sensors a linear calibration of sensor output to sensed current

was supplied by the manufacturer. Sensor biasing and a validation for experimental setup

were conducted against the RMS current sensed by the factory calibrated power supply unit.

The indicated rotational speed is calculated from the hall-effect sensor picking up the

passes of a magnet and a timer signal from the factory-calibrated DAQ counter-time system

giving the time between the passes. Results were validated against optical rpm sensors and

fast fourier transform analysis of the force balance data.

The six-component ATI-mini force balance was calibrated by the manufacturer against

loading on multiple axes. This calibration was validated using single axes forces and moments

applied close the measurement centre of the balance and no recalibration was necessary. The

static loading following the integration of the force balance was compensated through biasing

the sensor.

The collective pitch angle calibration was based on the linear relationship between the

blade pitch angle and the distance travelled by the pitch-linkage rod. A series of static

measurements of the blade pitch was taken with a pitch gauge and by measuring the leading

and trailing edge height above a reference plane. Each measured pitch angle was then

correlated to the corresponding actuator demand. An actuator with integrated potentiometer

and closed-loop position control loop was used, so that the position demands could be

reached under load.

The tunnel speed was calibrated using the standard wind tunnel practice [64] of using the pressure change across the tunnel contraction with the setup described in Chapter 4.2.2. The pressure transducers produced a voltage signal linearly proportional to the pressure change across the tunnel contraction. This voltage signal was directly calibrated against the measured Pitot static pressure close to the centre of an empty test-section. The Pitot static pressure itself was obtained using a factory calibrated anemometer. Calibrations were performed at a range of tunnel speeds up to 25 m/s and a clear linear relationship could be established for speeds above 5 m/s. In the regime from 2.5 – 5 m/s only the low-range transducer produced a linear response, but significantly increased measurement uncertainty is expected in this region.
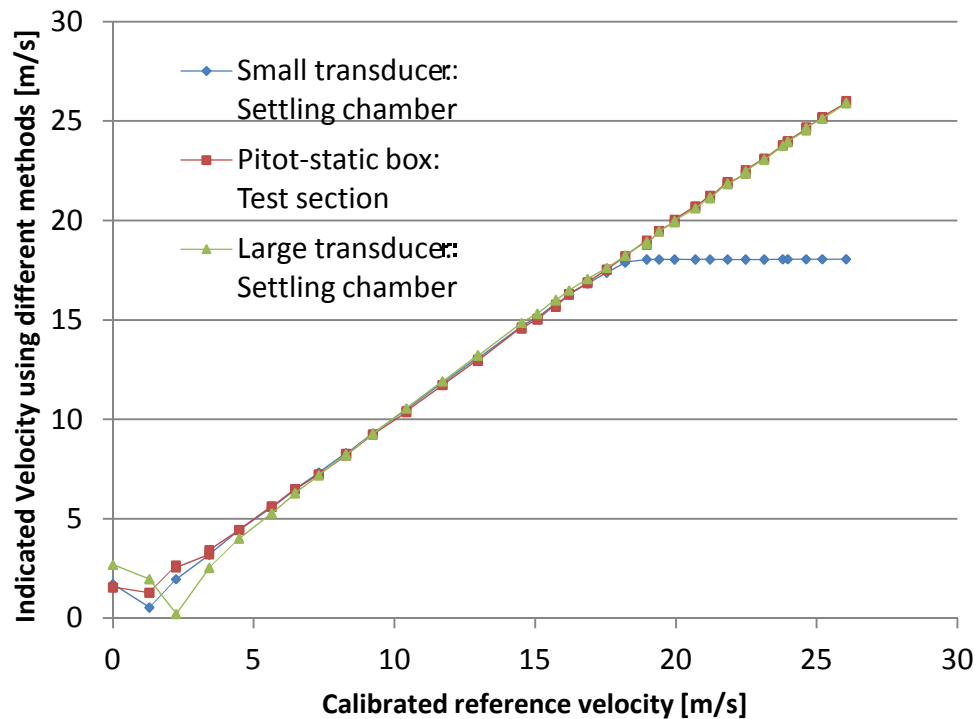
Figure 32: Tunnel speed calibrations.

4.3.2 Data sampling conditions

Sampling time, rates and number of samples had to be chosen to ensure data quality whilst maximising the number of combination that can be measured in a given time. In this section it is discussed how suitable parameters were determined from experiments.

4.3.2.1 Settling time

The settling time to reach steady-state is driven by the inertia of a system and needs to be considered for the wind tunnel speed and demand changes to the propeller system.

Figure 33 shows the tunnel-speed response to step inputs to the drive mechanism. The velocity response measured across the contracting cone is slightly underdamped and steady state is reached within 15-25 seconds. An additional, albeit smaller, delay is introduced by the time the flow requires to travel from the contracting cone to the centre of the section. A conservative 60 s tunnel settling time was selected to ensure steady state conditions in the test section.

Figure 34 shows the non-dimensional rotor PWM demand and rotational speed response for a high collective pitch, high torque coefficient case. For a PMW demand increase of 20% (+0.2 ms) the settling time for a rising rotor rpm is significantly less than 1 s. For a rapid decrease (PWM demand down from 80% to 0%) in rotor rpm the settling time is in the order of 2-3 s and this is strongly dependent on the brake function of the motor speed controller. For the single rotor experiments a worst case settling time of 3 s was used. In the multi-rotor trim loops a settling time of 1 s is used in combination with saturation limits on the rate of rpm change to ensure steady state values.
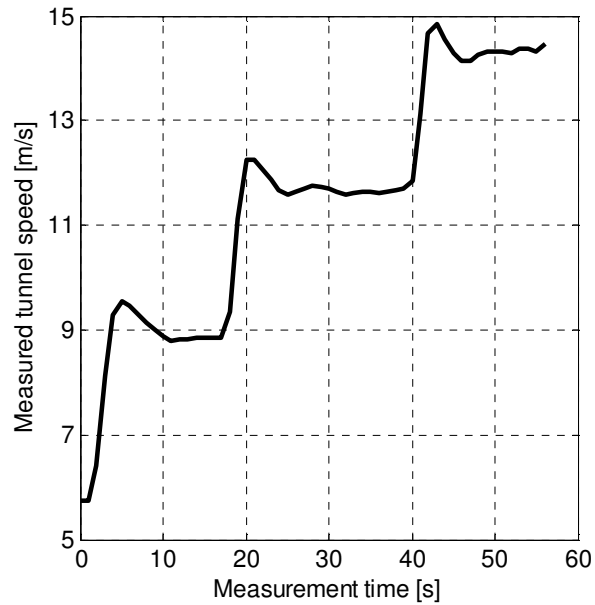
Figure 33: Velocity, measured using pressure drop across settling chamber, averaged over 0.5 s.

a)

b)
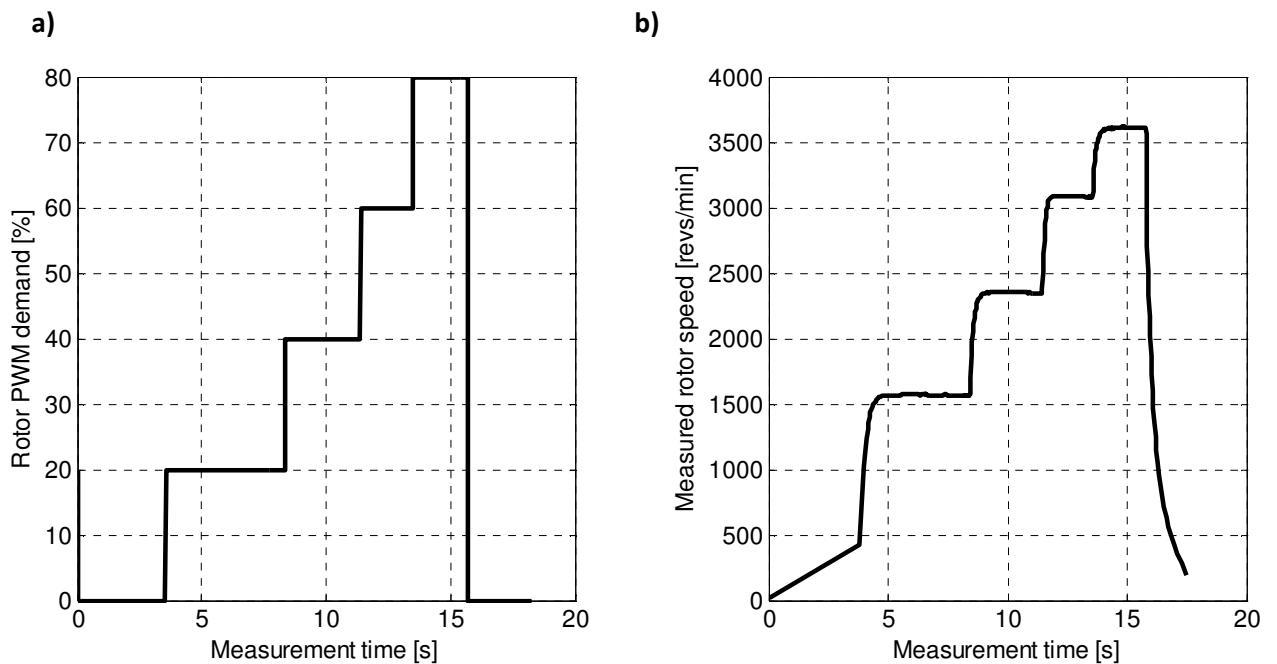
Figure 34: Motor demand and rpm response for high collective pitch variable pitch system in hover.

4.3.2.2 Sampling rates and number of samples

The constraints on sampling rates and sample length were computational power and

the time required for data acquisition. A distinction had to be made for time-averaged results

(force, pressure, current) and time-dependent results (rpm sensor data).

First, the time-dependent rpm sensing is discussed. Figure 35 shows the voltage signal from the hall effect rpm sensor at approx 7000 rpm. Every time the installed magnet passes the sensor the voltage drops to zero and the rotational speed was calculated using the time between these falling edges. The sampling frequency was determined using the Nyquist-Shannon sampling theorem: "If a function x(t) contains no frequencies higher than B hertz, it is completely determined by giving its ordinates at a series of points spaced 1/(2B) seconds apart" [65]. The Nyquist theorem had to be applied to the frequency based on the short periods of the magnet passing the sensor around 0 V (< 0.5 ms, 2 kHz). Figure 35 shows how the signal could be reconstructed by oversampling at a sampling frequency of 10 kHz, whereas no meaningful data could be obtained if the Nyquist rule is applied to the rotor rpm and data is sampled at 1 kHz.

Next, sampling settings for the time-averaged signals were determined experimentally. For pressure and current sensors a 1 kHz sampling frequency and 1 s sample length were found sufficient to capture the steady-state value with noise levels below the expected experimental uncertainty. The force balance was subject to significant noise that could not be filtered using a band-pass filter. The noise problem was reduced by oversampling at the highest feasible sampling rate of 10k Hz and averaging the data over a length of samples. Figure 35 (a) shows the effect of sampling length: Whilst a 0.1 s sampling length significantly reduces noise it was decided to match the 1 s sampling time for the other sensors to further reduce the noise level.
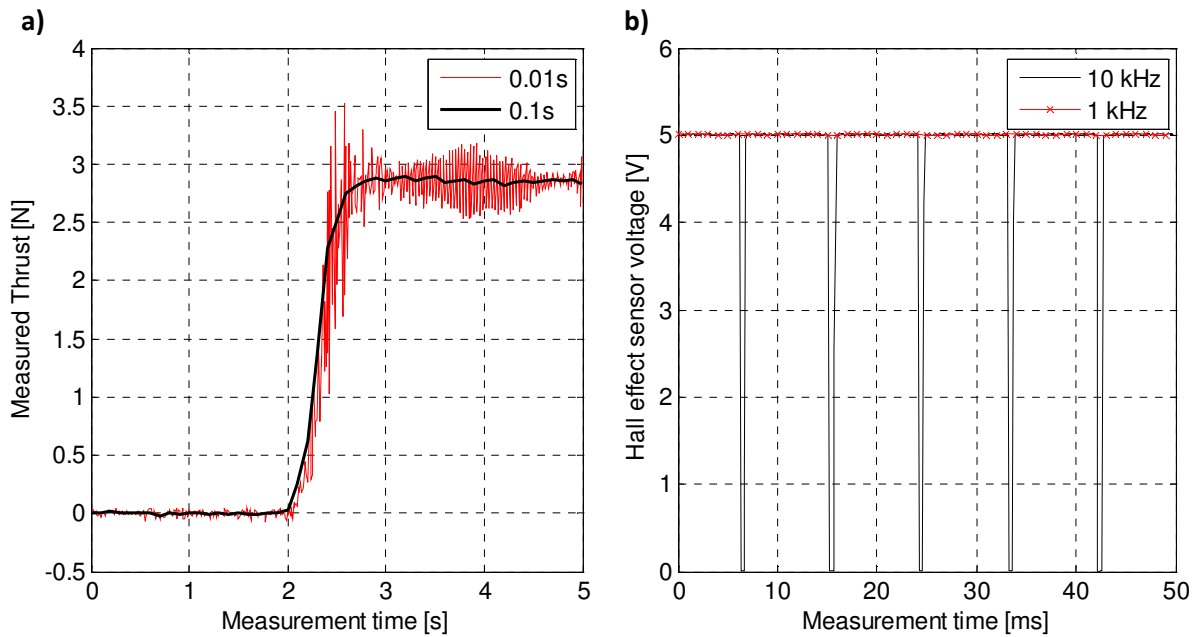
Figure 35: Effect of sample length on thrust (a) and of sampling frequency on hall effect rpm signal (b).

4.3.2.3 Summary and limitations of the data sampling conditions

Using the proposed setup time-averaged steady-state measurements of the variables of interest can be obtained and the sampling conditions are summarised in Table 7. Due to the trade-offs between data-quality, sampling time and frequency the proposed sampling settings and setup are not suitable to measure high quality dynamic data on rotor response to rpm and pitch demands at time-scales of less than one blade revolution.

Sensor/Operation	Settling time to steady state [s]	Sampling rate [kHz]	Number of samples
Tunnel velocity changes	60		
Pitot-static		1	1000
Small-range transducer		1	1000
Large-range transducer		1	1000
Rotor demand changes	3 (1 s for trim study)		
Hall effect RPM sensor		10	10 000
Hall effect current sensors		1	1000
Rotor/Vehicle force data	3		
Six-component balance		10	10 000

Table 7: Summary of data sampling conditions.

4.3.3 Procedure for single rotor wind tunnel experiments

Following the tunnel speed and sensor calibration, wind tunnel experiments were carried out on fixed-pitch, variable-speed rotors and variable-pitch, variable-speed rotors. A similar procedure was applied for both types of rotors.

Step 1: Installation and setup

Rotors and motors were balanced and the motor speed controllers were programmed to repeatable settings used throughout the experiment. All components of the rig were installed in the test section and positioned to bring the specimen close to the centre of the tunnel and the rotational alignment of propeller and force balance was measured using an inclinometer. For variable pitch rotors the actuator position vs. blade pitch calibration was checked. Sensor and power wires were taped to the measurement strut to minimize flow field disturbance. The sensor signals were checked and the repeatability of the setup was validated.

Step 2: Sweeping disk angles of attack and velocities

With the tunnel and motor both switched off, the overhead yaw turn table was used to change the disk angle of attack from +90 deg (climb) to −90 deg (descent). The increments were biased towards the 0-30 deg region of practical interest.

Once the angle had been set the force balance and pressure transducers were zeroed. For each disk angle the tunnel speed was set manually and varied from 2.5 m/s to 22.5 m/s in increments of 2.5-5 m/s and with the 60s settling time determined in Chapter 4.3.2. For each disk angle of attack the aerodynamic forces of the assembly were recorded at one of the high speed cases with the rotors still being switched off. Temperature and atmospheric pressure were recorded for each velocity/disk angle of attack combination.

Step 3: Running RPM and collective pitch sequence and recording data

For each unique combination of tunnel angle and velocity the motor was powered on, the ESC range calibrated and the motors and ESC warmed up to ensure repeatable results. An automated sequence of motor rpm (ESC PWM) and collective pitch demands was run with small increments. Measurements were taken with the sampling conditions described in Chapter 4.3.2.
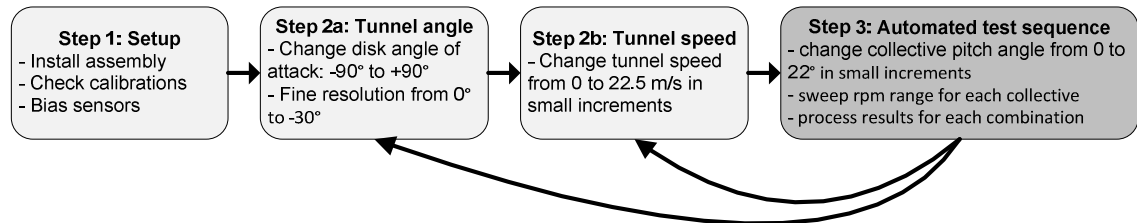
Figure 36: Experimental procedure for single rotor experiments.

4.3.5 Procedure for closed loop trim studies

The forward flight trim experiments were conducted on the Aeroquad open source quadrotor frame and the adjustable quadrotor test-rig, which was used in "x" and "+" configurations at different rotor spacings.

First, the force balance was biased (reset to zero) and the vehicle was mounted vertically on the force balance at end of L-shaped strut (Figure 26). The centre of gravity was identified from force balance data and the balance was re-biased to offset any weight effect of the vehicle.

A LabView programme for the closed loop trim routines was initialised and set with demands for the vehicle "weight", a prescribed CG about which to trim the vehicle, motor saturation limits and maximum residual force values to define convergence.

The vehicle motors and wind tunnel were switched on and the trim studies were conducted from hover up to 20 m/s in approximately 2.5 m/s increments. For each wind speed a closed-loop LabView trim routine was run to find vehicle angle of attack and rotor speeds to

ensure near zero net forces/moments at the CG. The trim routine is broken down into two loops to prevent the slower vehicle angle of attack updates from delaying the more rapid motor rpm loop:

In the outer trim loop the vehicle angle of attack was adjusted semi-automatically to reduce the total vehicle drag in F_{X_earth}. The vehicle angle of attack updates were based on a gradient analysis from the previous residual drag values.

In the inner trim loop the individual motor rotational speeds were set to counteract the vehicle "weight" in the Z_{earth} axis ($\sum F_{Z\_earth} \rightarrow 0$) and ensure zero net moments about the user-defined CG ($\sum M_{body} \rightarrow 0$). Updates were calculated based on a simple proportional control loop using force balance data. A sufficient settling time, as defined previously, was left between updates.

Two main difficulties were experienced when running this experiment. First, strong vibration and unsteady motor loading were experienced near the top-speed, making it difficult to precisely map out fine differences in absolute top-speed for different configurations. Secondly, the adjustable quadrotor test-rig was found to have a different body drag for the "x" and "+" configuration not enabling the desired like-for-like comparison of the power and trim curves for the two configurations.
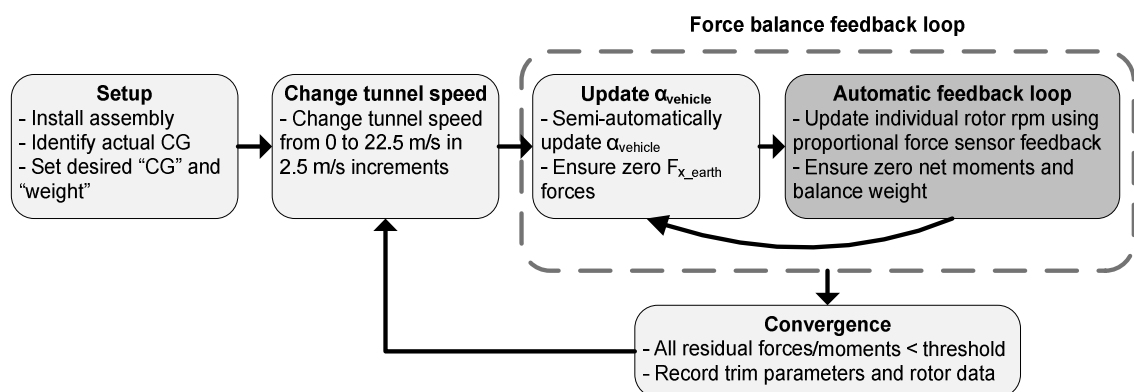
Figure 37: Experimental procedure for the closed loop trim studies.

112

4.3.6 Adjustable quadrotor test-rig: interference testing procedure

The study of rotor interference effects is an extensive multi-variable problem strongly dependent on vehicle orientation, airspeed, rotor loading, rotor spacing and orientation. To restrict the number of variables all experiments were carried out along the airspeed-trim setting curves defined from the previous experiment.

First, the adjustable test-rig was mounted in the tunnel in either "x" or "+" configuration and the alignment tested with an inclinometer. Both configurations were tested, although the "x" results later had to be discarded due to wall inference effects (see Chapter 6.2.2). All experiments were conducted for four rotor spacings (d/D = 1.03, 1.1, 1,2 and 1.3).

The six-component force balance was placed between the motor support bracket and the quadrotor airframe. The experiments were repeated for front, rear and side rotors. All wiring connections across the force balance were securely attached to avoid distortions to the force measurements. The balance was re-biased following every change in rotor spacing.

The tunnel was started and velocities from 0-20 m/s were studied in 2.5 m/s increments. For every airspeed the previously defined trim conditions (vehicle angle of attack and rotor rpm) were loaded. The motors were switched on and off in an automated test sequence about their trim conditions identified earlier. The sequence consisted of:

- Single motor running (with the force balance) at trimmed value.
- All possible commutation of rotor pairs running at trim values, as to identify main source of interference.
- All rotors running at the previously determined trim values.

The measurements taken at every step of the sequence consisted of the rotor forces/moments, rpm and electric power values of the motor currently studied as well as electric power and rpm of all other rotors.

Once the test sequence was completed it was repeated for the next wind speed, rotor spacing and vehicle configuration.

| Obtain trim curves
- For both "x" and "+" configuration
- For each spacing | Select configuration and rotor
- Set configuration
- Install force balance under front/rear/side motor | Change rotor spacing
- Change spacing from d/D 1.03 to 1.3
- Bias force balance after changes | Load trim parameters
- Set tunnel speed
- Set trim $\alpha_{vehicle}$
- Set trim rpms | Automated interference sequence
- Single rotor on
- All rotors on
- Pair-wise on/off
- Take measurements |

Figure 38: Experimental procedure for the quadrotor interference studies.

4.3.7 Quadrotor body drag procedure

Quadrotor body drag measurements were conducted on the two airframes with their rotor blades removed. The battery tray on both vehicles was replaced with a reinforced, but geometrically similar battery tray to attach the force balance directly to the vehicle without modifying the vehicle geometry.

Vehicle and force balance were mounted on an L-shaped support strut in a vertical orientation as shown in Figure 30 and the alignment was checked with an inclinometer.

Force balance readings were used to obtain the CG of the vehicles for reference and the balance was then biased to offset the vehicle weight.

The tunnel was switched on and tests were conducted from 5 to 22.5 m/s. The lower speed values of 5 to 15 m/s were used to check for Reynolds number effects, but all force coefficients were later based on the results obtained between 15-22.5 m/s as these offered the largest absolute forces and lowest measurement uncertainty.

For every tunnel speed the vehicle angle of attack was swept from -90 deg (pure climb) to 90 deg (descent) in 15 deg increments. In the most relevant forward flight regime from 0 to -30 deg experiments were conducted in 2.5 deg increments.

4.4 Data reduction and tunnel corrections

4.4.1 Wind tunnel corrections

4.4.1.1 Aerodynamic forces on the test rig

Elements of the test rig, such as motors, actuator, motor brackets, wires and sensors had to be positioned at the measurement side of the force balance and gave rise to aerodynamic forces affecting measurement results. These effects were corrected by measuring the rig aerodynamic forces (without rotor blades) for every test angle, normalising the rig drag against airspeed and then subtracting this from the measurement results.

4.4.1.2 Corrections for single rotor experiments

The motor, sensors and motor bracket with a diameter of about ¼ of the rotor diameter had to be positioned within less than ¼ radius underneath the rotor giving rise to a small amount of interference with the rotor wake. The rotor loading distribution shown in Figure 23, however, shows that only a negligible fraction of thrust is produced by the inner ¼ radius and hence further corrections were not required.

The effect of the wind-tunnel walls on a single rotor near hover was approximated using the Cheeseman-Bennett ground effect equations [2]. The results indicate that the rotor to tunnel wall spacing of 2 rotor diameters or more is sufficient to keep ground effects on thrust to within less than 1%.

Next the effect of the rotor on the tunnel speed was evaluated. The strongest effect on the velocity induced in the tunnel flow direction was expected in the pure climb case. For this case the rotor acts like a propeller and Glauert's velocity correction [64] was used to assess the required correction for rotors between 10-13 cm radius and at thrust levels from 2-3 N which are typical for a 1 kg class quadrotor. Results presented in Figure 39 show that the velocity

correction effects are very small. For flight speeds over 5 m/s they are typically less than 2%, fall within the measurement noise of the tunnel speed measurements and could be neglected.
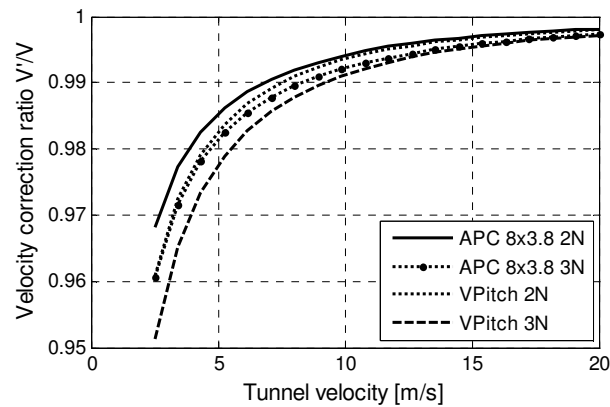
Figure 39: Glauert velocity correction factor for the test arrangement.

4.4.1.3 Correction for full-scale vehicle tests

Corrections for the wind tunnel testing of complete rotorcraft models are more difficult and it was initially unclear what minimum tunnel wall distance and rotor disk to test section area ratio was required for quadrotor windtunnel tests.

Literature on wind tunnel testing of rotorcraft often applies fixed-wing correction solutions [63, 66]. The classic tandem rotor experiments by Halliday & Cox [63] were used as the example most closely related to the current experiments. Halliday & Cox applied a standard boundary correction method to correct the effective vehicle angle of attack:

$$\Delta \alpha = \delta \frac{A_{disk}}{A_{Test\_section}} C_L \quad (rad)$$

Eq. 88)

Where C_L represents the equivalent lift coefficient of a wing of the same area and δ represents a boundary correction factor dependent on the tunnel geometry.

The wind tunnel boundary correction factor for the project tunnel was approximated using the theoretical results presented by Theodorson [67]. Based on the project tunnel's height/width ratio of 0.8 and assuming the rotor radius was sufficiently small compared to the

tunnel width, $\delta = 0.125$ was obtained. For a 1 kg quadrotor with R=0.1 m rotors and test at 10 m/s this means a correction of less than 1 deg to the vehicle angle of attack.

Fixed-wing based correction methods such as those presented in [63, 66] are no ideal solution for rotorcraft testing [63]. One of the key problems relevant to this work is that the model appears to break down in the important low speed regime of the quadrotor flight envelope. At these speeds the equivalent lift coefficient increases dramatically and the angle of attack corrections become unphysical and cannot be used.

Based on the difficulties of the boundary correction model to capture low speed corrections and the moderate angle of attack correction values at high speed, it was decided to present all results for quadrotor trim curves and body drag without using a correction factor. Whilst it is acknowledged that this is a simplification and true vehicle angles of attack could be slightly higher than presented in this study, it is expected that the validity of the conclusions made from the data holds. Uncertainty remains on the wall effects and this is discussed together with experimental results for the effect of rotor spacing in Chapter 6.

4.4.2 Data filtering and rejection

Under some conditions, resonance on the measurement rig could be observed. A fine rotor-rpm sweep in hover was conducted and resonances were identified from excessive noise in the off-axis force measurements. The data was used to identify narrow resonance frequency bands which were then avoided or filtered from all future measurements.

To ensure results represent steady-state values the relative noise and drift in a signal over the measurement time was observed. Data points in which noticeable drift (over 2 %) or noise between the start and finish of the measurement period was observed were rejected. An exception to this was made for data presented in the vortex ring state in which strong fluctuations were expected.

4.4.3 Transformation of force signals

All single rotor results were first corrected for assembly drag of the rig, as discussed previous, and then transferred from the balance measurement centre to the desired reference point: the hub centre for the single rotors or the predefined CG or reference point for multi-rotor experiments.

Next, suitable Euler rotations are used to rotate the forces from the balance coordinate system to the desired reference system (earth axes, body axes or hub axes). At this stage small rotational misalignments of the force balance z-axis could also be corrected.

4.4.4 Non-dimensionalising measurement results

Where it was appropriate, all rotor force and moments are expressed in standard helicopter force and moment coefficients as introduced in Chapter 2.5, Equation 29.

The variable rotational speed operations of quadrotors mean that it was not always practical to normalise the airspeed against the rotor tip speed. It was hence decided to present absolute airspeed and instead of non-dimensional advance ratios typically used in helicopter literature.

The selection of a suitable reference area for body drag is not straightforward [6] and hence the body drag is not expressed as a conventional drag coefficient, but as an equivalent flat plate area:

$$f = \frac{D}{\frac{1}{2}\rho V^2} \ [m^2]$$ Eq. 89)

This equivalent flat plate area is defined as *"the frontal area of a flat plate with a drag coefficient of 1, which has the same drag as the object whose drag is being estimated"* ([6], p132). The same procedure is applied to fuselage downforce. All "fuselage force coefficients" discussed later on in this thesis refer to a flat plate area of the above definition.

4.5 Uncertainty analysis

The aim of this section is to quantify the experimental uncertainty, identify the driving factors

and define measurement procedures to reduce uncertainty.

4.5.1 Definitions

An error is defined as the deviation from a KNOWN value, whereas an uncertainty means

that a measured value lies within certain plus/minus range of the true value [68]. For this work

all estimated uncertainties are expressed as "expanded uncertainties" about their nominal

measurement value.

4.5.2 Method for establishing uncertainty

The crudest way of estimating the uncertainty of a result derived from different

instrumental inputs is to sum up the maximum uncertainty for all measurements. This worst

case scenario is, however, not a realistic representation, because the maximum errors of

independent sensors would be very unlikely to correspond [68].

For this work, a standard method by Kline and McClintock as presented in [68] is used. This

method is based on specifying the uncertainty in each independent primary measurement x_i

contributing to the calculated experimental result R. The uncertainty of each measurement x_i

is expressed as:

$$x_i \pm \omega_i.$$

Where Kline and McClintock propose the experimenter specifies certain odds for the

uncertainty. For the purpose of this work a 95% confidence interval was used for the

uncertainty of the independent measurement uncertainties.

If the result function R of several independent measurements takes the form of a product,

as applicable to aerodynamic coefficients, it can be expressed as:

$$R = x_1^{a1} x_2^{a2} \dots x_n^{an}$$

<div align="right">Eq. 90)</div>

The uncertainty in R is expressed as

$$\omega_R = \left[\left(\frac{\partial R}{\partial x_1} \omega_1 \right)^2 + \left(\frac{\partial R}{\partial x_2} \omega_2 \right)^2 + \dots + \left(\frac{\partial R}{\partial x_n} \omega_n \right)^2 \right]^{1/2}$$

<div align="right">Eq. 91)</div>

Eq 91 can be simplified dividing by Eq 90 and using partial fractions:

$$\frac{\omega_R}{R} = \left[\Sigma \left(\frac{a_i \omega_i}{x_i} \right)^2 \right]^{1/2}$$

<div align="right">Eq. 92)</div>

From equation 92 two important observations can be made:

1. The uncertainty in R is driven by the square of the uncertainties of the individual contributions meaning that the largest individual uncertainty will dominate the uncertainty in R.

2. The uncertainty is dependent on the absolute value of each independent variable x_i and will decrease with an increase in x_i, for a given ω_i. The significance of this is that the uncertainty is best defined if a range of x_i conditions rather than a single point are considered.

4.5.3 Uncertainty estimation of the results

The uncertainty in the key experimental results can be expressed as:

- Aerodynamic force and torque coefficients (CF$_i$,CM$_i$)

$$\frac{\omega C_{Fi}}{C_{Fi}} = \left[(1)^2 \left(\frac{\omega F_i}{F_i} \right)^2 + (-1)^2 \left(\frac{\omega \rho}{\rho} \right)^2 \right.$$

$$\left. + (4)^2 \left(\frac{\omega R_{rotor}}{R_{rotor}} \right)^2 + (-2)^2 \left(\frac{\omega \Omega}{\Omega} \right)^2 \right]^{1/2}$$

<div align="right">Eq. 93)</div>

$$\frac{\omega C_{Mi}}{C_{Mi}} = \left[(1)^2 \left(\frac{\omega M_i}{M_i}\right)^2 + (-1)^2 \left(\frac{\omega \rho}{\rho}\right)^2 \right.$$

$$\left. + (5)^2 \left(\frac{\omega R_{rotor}}{R_{rotor}}\right)^2 + (-2)^2 \left(\frac{\omega \Omega}{\Omega}\right)^2 \right]^{1/2}$$

Eq. 94)

- Power (Electric, Mechanical)

$$\frac{\omega P_{El}}{P_{El}} = \left[(1)^2 \left(\frac{\omega V}{V}\right)^2 + (1)^2 \left(\frac{\omega I}{I}\right)^2\right]^{1/2}$$

Eq. 95)

$$\frac{\omega P_{mech}}{P_{mech}} = \left[(1)^2 \left(\frac{\omega \Omega}{\Omega}\right)^2 + (1)^2 \left(\frac{\omega M_z}{M_z}\right)^2\right]^{1/2}$$

Eq. 96)

- Tunnel speed

$$\frac{\omega U_\infty}{U_\infty} = \left[\left(\frac{1}{2}\right)^2 \left(\frac{\omega P_{transducer}}{P_{transducer}}\right)^2 + \left(-\frac{1}{2}\right)^2 \left(\frac{\omega \rho}{\rho}\right)^2\right]^{1/2}$$

Eq. 97)

The underlying uncertainties of each independent sensor ωx_i were taken from manufacturer datasheets and calibration data as well as from calibrations against known reference values, such as test-weights. Uncertainties were based on the same data acquisition system used in the experiment and hence also reflect the uncertainties inherit in the DAQ system, like the DAQ counter/time ([68], p204) and analogue input uncertainties and resolution limits.

Figure 40 shows the variation of experimental uncertainty against nominal values for result x_i. These figures clearly show an increase in uncertainty for small measurement values and were used to constrain the experimental space to area for which an uncertainty below a certain threshold can be achieved.

4.5.4 Conclusions on uncertainty

For rotor thrust, torque and power coefficients of practical interest the uncertainty was found to be in the order of 5 % or less and considered acceptable for this research. The uncertainty in the tunnel speed measurement is below 10% for speeds higher than 5 m/s and less than 5% for speeds higher than approximately 7.5 m/s. At very low speeds of less than 5 m/s experimental results are further influenced by the tunnels capability of holding the low speed.

The uncertainty in the measurements of small forces and moments, such as the hub forces and moments, was found to be significantly larger and in excess of 10% for very low values. This is driven by the fact that these forces and moments are generally an order of magnitude smaller than the rotor thrust and torque. Hence, only a small part of the range of the balance is used and uncertainty increases. Due to the compactness requirements of the internal force balance, the limited availability of suitable commercial six-component balances and the lack of available data, this was considered to be an acceptable limitation. Furthermore, a twofold approach is used to manage experimental uncertainty:

1. The uncertainty for each measurement is expressed using error-bars giving the reader an appreciation of the uncertainty under the respective measurement conditions.

2. Experimental procedures are put in place to limit uncertainty:

- Wherever possible measurements are taken at higher force and tunnel speed values to improve the signal to noise ratio.

- Measurements are repeated.

- Suitable corrections and sensor bias readings are considered.
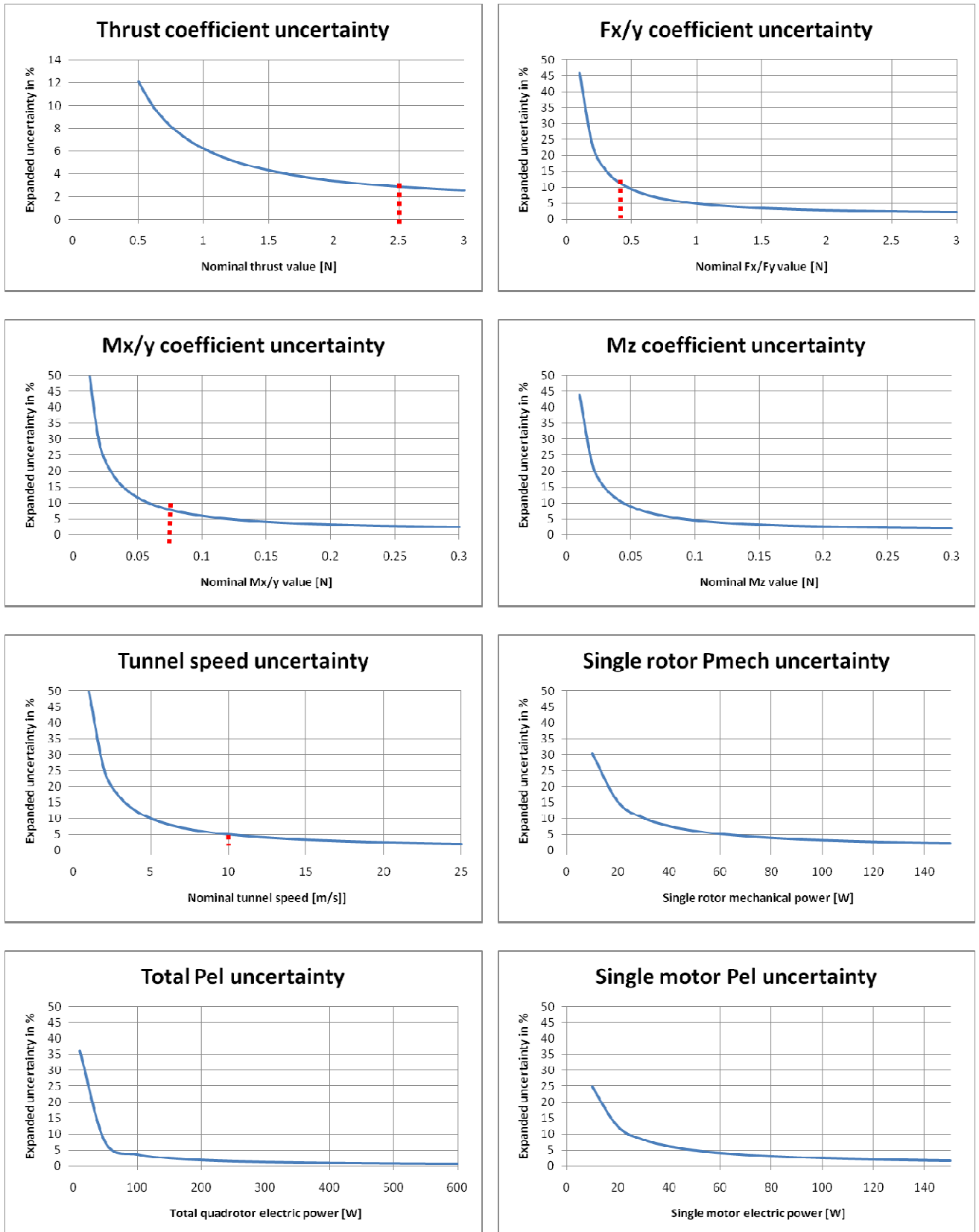
Figure 40: Measurement uncertainty for the variation of different measurement variables. The red lines indicate typical rotor operating conditions in forward flight.

123

4.6 Experimental methods, conclusions and limitations

Experimental measurement setups and procedures were introduced and shown to be suitable to repeatably measure the steady-state, time-averaged forces and moments, the rotational speed and power demands of a single rotor and full quadrotor vehicle.

An uncertainty analysis on the experiments showed that uncertainty for nominal tunnel speed, thrust, torque and power values was acceptable, but that increased uncertainty had to be expected for smaller forces and moments, which is particularly relevant to smaller hub forces and moments. Experimental procedures to manage uncertainty were introduced and the experimental uncertainty is considered in the discussion of the results.

Wind tunnel correction methods were investigated and it was found that a rotor disk to test section area ratio of 0.05 appears sufficiently large to avoid tunnel interference effects for single rotor experiments. However, tunnel wall effects on full quadrotor experiments could not be determined conclusively and experimental observations will be discussed with the results of the quadrotor interference study (see Chapter 6.2.2).

A novel closed-loop quadrotor trim method based on force-balance feedback was introduced and enables the study of quadrotor forward flight trim and power curves in a controlled environment. The method allows the researcher to rapidly obtain power and trim curves for different CG positions and take-off weights and thus helps to add previously unavailable data to literature.

Chapter 5: Results – Rotor Aerodynamics

The objectives of this chapter are:

> *To understand the forces and moments created by a single hingeless, variable-speed, variable-pitch quadrotor rotor in hover, climb and forward flight and to evaluate the performance of the proposed simulation model using wind-tunnel data.*

5.1 Chapter overview

An understanding of the six components of forces and moments transferred to the rotor hub is required for the study of quadrotor flight performance, but the applicability of previous helicopter and propeller data is limited due to the nature of quadrotor rotors discussed in Chapter 1.

This Chapter presents experimental data for one variable pitch and one fixed pitch rotor at selected test-cases. The Chapter is structured in line with typical helicopter literature by considering hover, axial and then forward flight. Both experimental and blade element theory (BET) simulation results are presented. For all experiments the rotational speed (rpm) and collective pitch were controlled and results are expressed in coefficient form for an untrimmed rotor.

The forward flight discussion highlights the importance of the pitching moment for quadrotor rotors. Furthermore, a strong increase in forward flight power with large negative disk angles was observed.

Different blade element modelling choices are evaluated and limitations are discussed. A local-differential blade element method was found to be an acceptable low-order method for the velocity range of practical interest, because it can capture hover as well as the key rotor behaviour in forward flight condition at moderate collective and disk angles.

5.2 Rotor aerodynamics in hover

5.2.1 Thrust and power against baseline BET model

A comparison of the experimental variable-pitch hover results with the local-differential blade element model is presented in Figure 41. The "baseline" model refers to airfoil data based on Xfoil and the numerical setup as discussed in Chapter 4. At low pitch angles up to around 15 deg the thrust coefficient gradient is approximately linear. Above an angle of 15 deg the thrust coefficient gradient flattens out, consistent with parts of the rotor disk entering the nonlinear region of the lift curve slope, where any additional increase in pitch, and hence angle of attack, yields a smaller increase in thrust.

The torque coefficient response is approximately quadratic with pitch angle, with a rapid increase in torque for larger pitch angles beyond 15 deg. From basic helicopter theory (Chapter 3.3.1) the torque coefficient is identical to the power coefficient, with the negative sign representing the fact that the direction of the reaction torque is opposed to the direction of rotation, counter-clockwise in this case.

Except for very low pitch angles, the baseline BET method shows a good agreement with the experimental thrust coefficient up to the onset of nonlinear effects between 15-20°. From this point onwards the baseline model initially over-predicts thrust and then predicts a drop in thrust at about 22°. This drop is caused by parts of the rotor disk entering the nonlinear part of the lift-curve slope around stall. In this regime, local flow separation on the blade is possible and the accuracy of the 2d airfoil model in the BET code is greatly reduced.

Considering now the torque results (Figure 41) the baseline model shows an acceptable agreement at moderate pitch angles, but starts diverging significantly from about 10-15°. The most likely reason for this are uncertainties in the drag model, in particular the change of drag with angle of attack at larger angles and uncertainties in the profile drag Cd_0

given the low local Reynolds numbers (<100k). The divergence in the power coefficient results

has also been observed in previous studies by Bramwell ([10], p111), who suggested that it

could be caused by a low profile drag coefficient. In the next section, Chapter 5.2.2, modelling

strategies are presented to improve the torque prediction.

Next, attention is drawn to the blade element results for a uniform inflow model

(Figure 41). The uniform inflow model follows the experimental thrust trend closely, but

diverges from around 20°. The torque prediction for angles above around 8° is significantly

below the experimental data and baseline BET results. This is because the uniform inflow

model misrepresents the local angle of attack distribution of the untwisted blade, especially at

large pitch angles. This observation highlights the key difference between the local-differential

blade element method (baseline), in which conservation laws are satisfied on each (local)

blade element, and the uniform inflow model, in which conservation laws are satisfied on a

(global) disk level. This can have a strong effect near the tips, if the radial variation in the

Prandtl tip loss model (see Chapter 3.3.8) is used on the induced velocity (shown in Figure 42

b). Since this can cause unrealistic loading near the blade tips and affect the thrust results the

combination of a uniform inflow model with the Prandtl tip loss model, as presented in the

formulation in Chapter 3.3.8, was found unsuitable for this research. Based on this and the

improved torque/power prediction in hover the local-differential model was selected as the

preferred model.

Results for a conventional fixed-pitch quadrotor rotor are presented in Figure 43.

Figure 43 a) contains 3rd party test data (Courtesy of Robert Goble, flybrushless.com) and good

agreement is found with experimental results from the present work. The baseline BET results

show good agreement up to moderate loading, but starts diverging under high loading –

especially at rotational speeds above the 8125 rpm limit suggested by the manufacturer.

Whilst theory implies thrust and torque should vary with rotational speed squared,

experimental data indicates that, in this case, they actually vary with rotational speed to a power slightly greater than 2. This could be related to Reynolds number effects or aeroelastic effects and is discussed separately in Chapter 5.2.3.

a)   b)
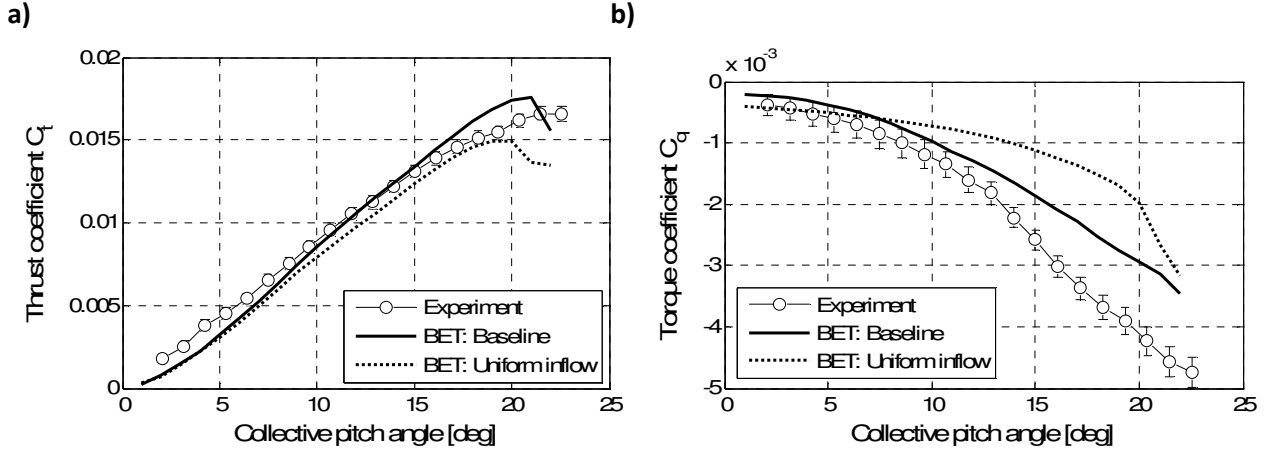
Figure 41: Comparison of baseline model thrust (a) and torque (b) coefficients against experimental results.

a)   b)
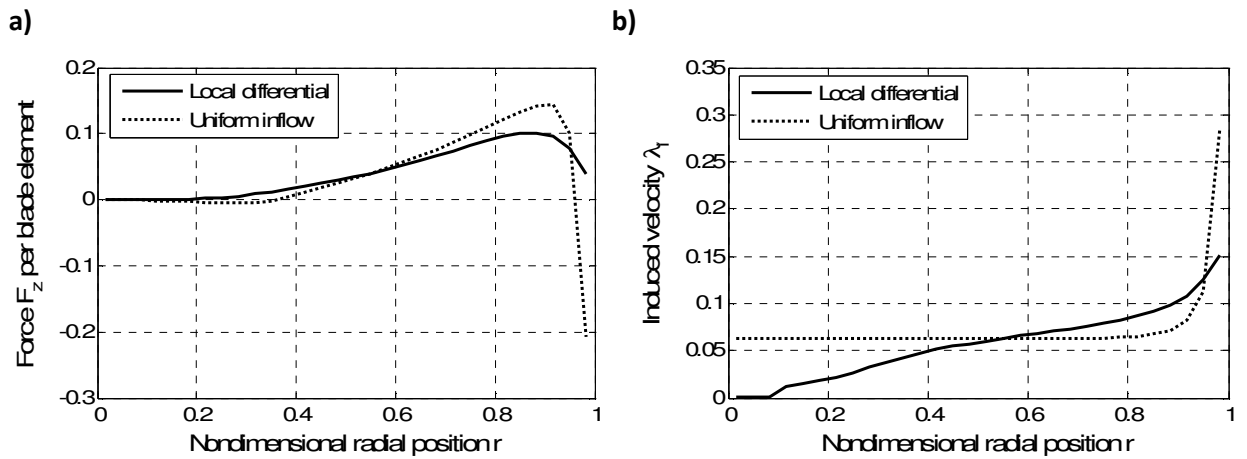
Figure 42: Radial loading (a) and non-dimensional inflow (b) distribution for both models: Uniform inflow in

combination with tip-loss model results in unrealistic tip loading.

a)   b)
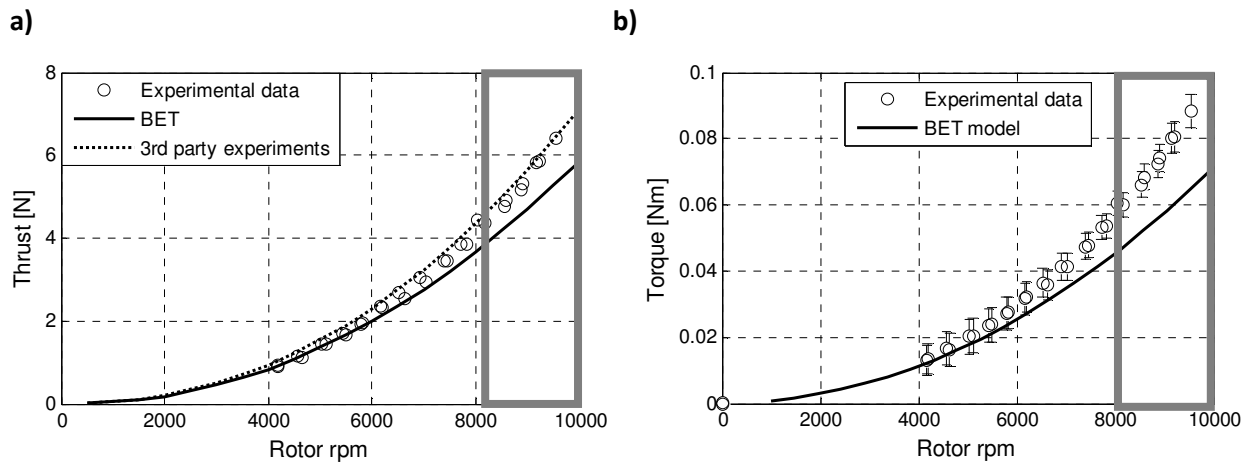
Figure 43: APC 8x3.8 prop against rpm, 3rd party thrust model [Courtesy of Robert Goble, Flybrushless.com],

Shaded areas are beyond suggested rpm limit of 8125 rpm.

Finally, results on rotor efficiency are presented in Figure 44. Small rotorcraft are often reported to have a reduced efficiency compared to larger helicopters [2] which is attributed to the relatively thick boundary layer, large values of profile drag, poor lift-to-drag ratios and high induced power requirement. As a result of this, typical induced power coefficients k, profile drag values C_{d0} and figures of merit from conventional helicopter literature often do not apply and are investigated in Figure 44.

In Figure 44 a) a standard graphical method [2] is applied to obtain k and C_{d0} from the hover thrust and torque coefficients of the 0.254 m diameter variable-pitch test rotor. The method is applied to values relating to low and moderate C_T (<0.011), where the results form a straight line as expected from theory. Values of k = 1.67 and C_{d0} = 0.022 were obtained which indicate significantly larger losses than on typical helicopters wind tunnel models (e.g. k=1.15, C_{d0} = 0.008 approx), but are slightly lower than literature values for a smaller 6 inch diameter rotor (k=1.75, C_{D0} = 0.035) ([2], p334). For higher thrust coefficients (C_T > 0.011) the graphical method breaks down, probably because of significant drag increases with local angle of attack which are not captured if the drag model is solely based on a mean C_{d0}.

Figure 44 (b) shows experimental and BET figure of merit data for a fixed–pitch APC 8x3.8 as a function of rpm. It can be seen that experimental FoM increases with rpm, which is consistent with expected improvement in aerodynamic performance at higher Reynolds numbers. A FoM of 0.55-0.63 can be obtained, which is above the efficiency reported for 6-inch smaller MAV rotors ([2], p334), and shows the positive effects of the chord and twist distribution on the APC 8x3.8. The trend in FoM is correctly predicted from BET, however the magnitude is slightly higher, consistent with an underestimation of torque/power coefficients.
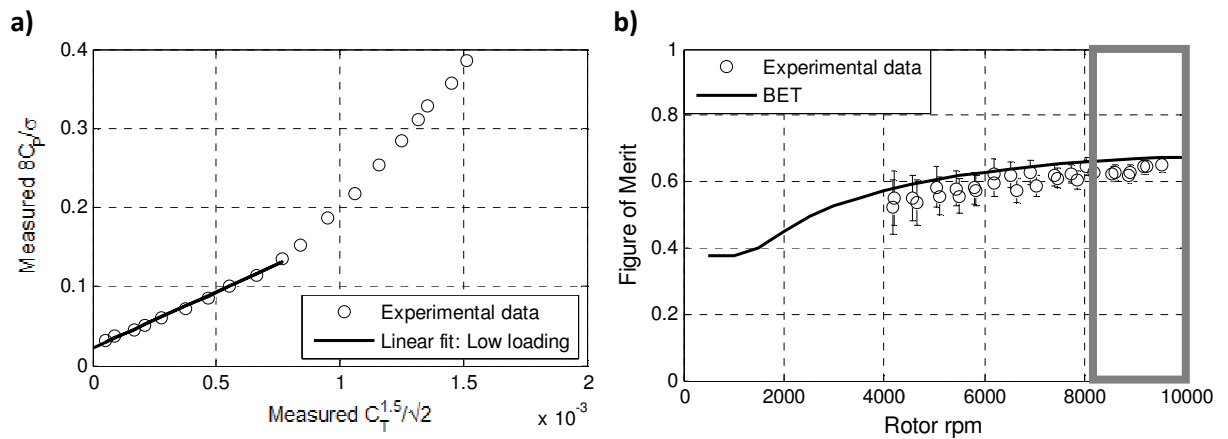
Figure 44: a) Graphic method for finding k and C$_{d0}$ on a variable-pitch rotor b) Figure of merit for a fixed-pitch rotor.

5.2.2 Effect of blade element modelling choices in hover

Some modelling choices, like choosing the local-differential blade element method (previous section), the numerical setup and the decision not to include the effects of the induced swirl velocity (both Chapter 3) were made in earlier parts of this thesis. This section now investigates further hover modelling choices with a particular focus on the 2-d airfoil models and the tip-loss effects.

Figure 45 shows thrust and torque results for modelling variations from the baseline BET model. First the tip-loss model is analysed: Without the tip-loss model the thrust coefficient is significantly increased and at large pitch collective pitch angles it is up to 15% above the baseline results. This is larger than the expected 6-9% tip-loss effects reported in Helicopter literature ([9], p60) and can be explained by the rotors operating at higher thrust coefficients than typically found in conventional helicopter literature. This amplifies the loading near the tip and hence increases the relative effect of the tip-loss modelling. In the absence of a tip-loss model, the larger thrust coefficient also increases induced power and hence causes a slight increase in power coefficient. This is untypical for helicopter rotors (2-4% according to [9], p61) operating at a lower C_T. As a consequence of the above the use of a Prandtl tip-loss model is highly recommended to improve the modelling of quadrotor rotors.

Next the 2-d aerodynamic model is analysed. Selecting a lift model based on the Javafoil package, rather than Xfoil (baseline) has negligible effects on thrust for most pitch angles, but small differences can be observed in the nonlinear part of the lift curve that acts at high collective pitch angles (around 20°). Because of the small differences between the lift models and the robustness of Xfoil, the Xfoil lift model is maintained for the remainder of the study.

As discussed previously, the baseline thrust coefficient shows a better agreement with experimental hover data than the torque coefficient, especially at collective pitch angles over 10°. This implies that Javafoil and Xfoil drag models fail to capture the profile drag magnitude and the drag variation with angle of attack. This is not unexpected given the reduced modelling fidelity at low Reynolds numbers and the uncertainty in leading edge radius and surface roughness of the small-scale blades. Drag results for a study on similarly-sized rotor blades [38] predicts a larger C_{d0} and a strong C_d variation with angle of attack that can best be described by a polynomial model. If such a second degree polynomial drag model (for details see Chapter 3.3.2) is fitted using experimental torque results at low and high pitch, a significantly improved torque (and power) prediction can be achieved without significantly altering the performance of the thrust results. As a result of this study a polynomial drag model is used for the remainder of the study unless indicated otherwise.

a)

b)
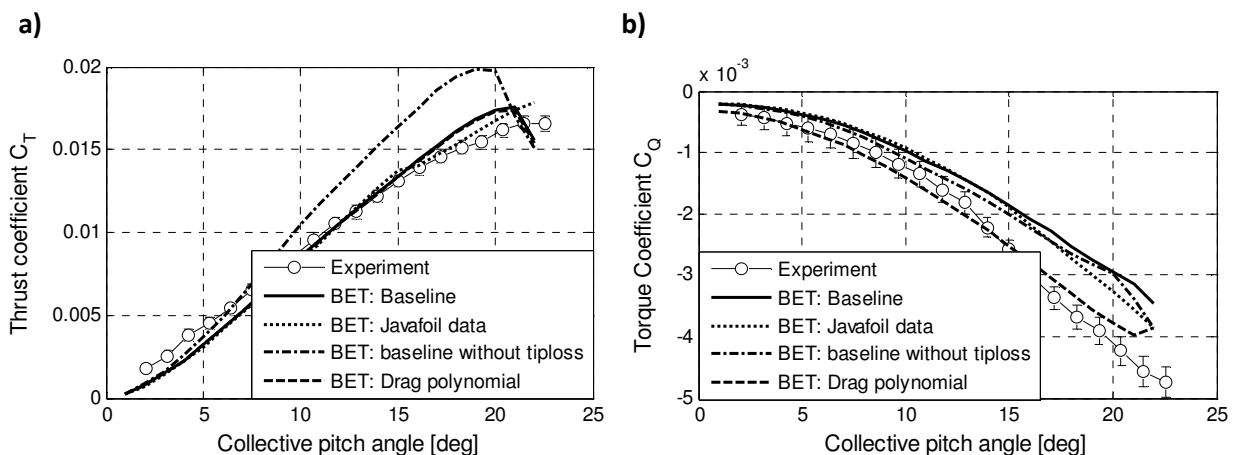
Figure 45: Influence of blade element modelling choices on thrust (a) and torque (b) coefficients.

5.2.3 Reynolds number and blade elastic effects

For the airfoils (NACA 0012, Clark-Y) and Reynolds number range (20k-200k) studied, experimental results from literature [49, 69] and Xfoil simulations suggest three main effects from increasing Reynolds number within the specified range:

- An increase in C_L

- An increase in the stall angle

- A reduction in C_D

From this, a hovering rotor would experience an increase in thrust coefficient and a reduction in torque coefficient with increasing Reynolds number. Experimentally, the Reynolds number can be varied by changing the rotor rpm as shown for the fixed-pitch APC 8x3.8 rotor in Figure 46. The blade element results, in this case based on a 2-d lift and drag lookup from Xfoil, show the expected Reynolds number trends of an increasing C_T and decreasing C_Q. Effects are most pronounced for rotational speeds below 4000 rpm (3/4 radius Re = 41k), and start levelling off between 4000-6000 rpm (3/4 radius Re = 63k). Experimental results show a rise in thrust coefficient beyond that expected from Reynolds number effects alone and the C_Q in fact increases significantly with rpm instead of decreasing. As discussed in Chapter 5.2.1 both, thrust and torque do not scale with rpm squared, as expected from basic theory, but scale with Ω^n with n > 2.2. A likely explanation is that this scaling is caused by structural rather than pure aerodynamic effects. Increasing rpm increases the lift acting at ¼ chord of the blade and induces a moment about the blade centreline near ½ chord. This causes a leading-edge-up elastic deformation (twist) of the blades, increases the local angle of attack and results in an increased rotor thrust compared to a stiff rotor. Whilst the present model for the fixed-pitch propeller can provide an acceptable agreement around nominal hover conditions (6000 rpm) a coupled aerodynamic-structural model could improve the quality of predictions at high loadings. The development of such a model is recommended for future work.

a)

b)
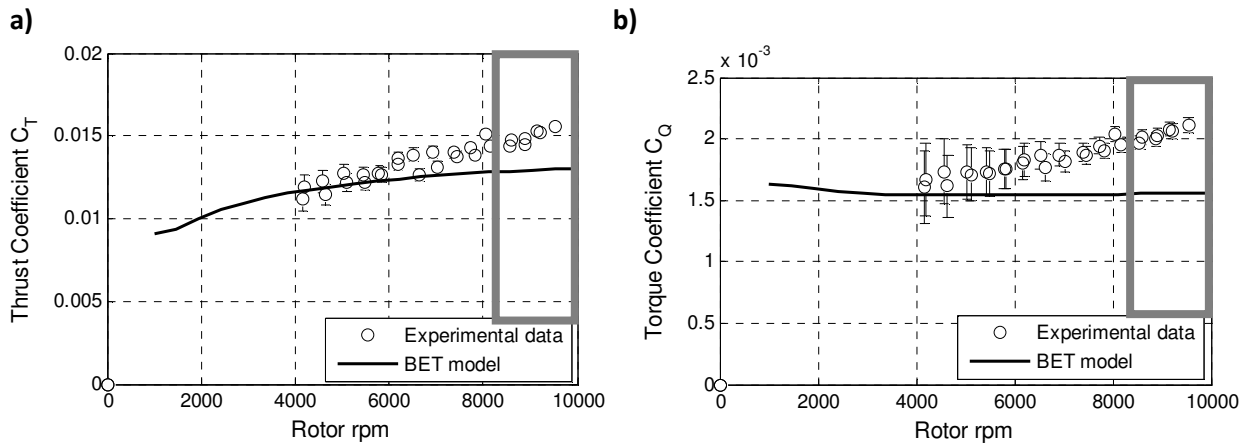
Figure 46: APC 8x3.8: The trend of thrust and torque coefficient against rpm

Next, Reynolds number and elastic effects are studied for the variable-pitch rotor operating at different rotational speeds and hence different Reynolds numbers. Both experimental and simulation results in Figure 47 show the expected trend of an increasing thrust coefficient with Reynolds number, but effects are much less pronounced than on the fixed-pitch APC 8x3.8 discussed previously. For most C_Q cases no noticeable trend with Reynolds number is apparent. The net result of the Reynolds number effects is an increased figure of merit for most pitch angles. Results do not indicate any noticeable elastic deformation effects in twisting, because the blade mounting point on the test blades is around the ¼ chord point of the blade preventing the creation of a strong twisting moment.

a)

b)

c)
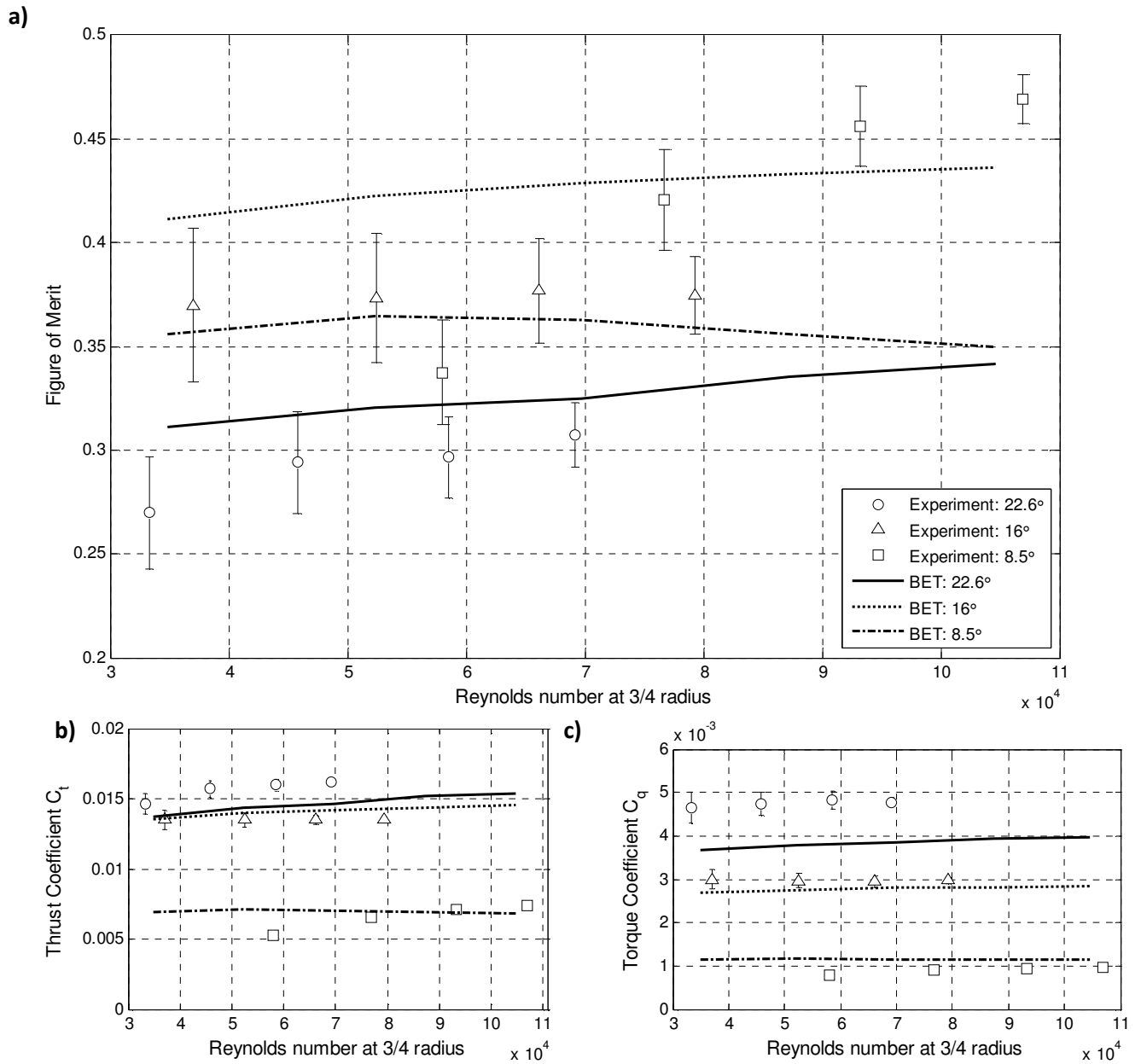
Figure 47: Effect of ¾ radius Reynolds number on Figure of Merit (a), thrust (b) and torque (c) coefficients of the variable pitch data (BET simulations based on Xfoil airfoil model).

5.3 Axial flight

In this section experimental and simulation results for a rotor in axial flight are discussed. Axial flight consists of descent and climb at zero forward speed, which is similar to a fixed-wing aircraft propeller in forward flight. In axial flight cases the flow is assumed to be axisymmetric.

Experimental results are discussed first. The reader is reminded that pitch and rpm were used as experimental control variables, rather than maintaining a constant power. The RPM was set between 4000-6000, depending on pitch, to ensure a similar hover thrust. Any rpm drift due to the ESC was also considered in the blade element simulations.

Figure 48 (a) and Figure 49 (a) show the thrust and power coefficients of a variable pitch rotor in descent (negative vertical velocity) and climb (positive vertical velocity). Climb speed increases the local inflow angle and, for a given pitch angle, decreases the local angle of attack. Hence the thrust coefficient reduces. For a given rpm there is a maximum climb speed up to which a rotor can produce a positive thrust. This maximum speed can be significantly increased by using a higher collective pitch and also scales with rpm as shown in Figure 50 (a). A close observation of the thrust trend in climb (Figure 48 a) reveals that large collective pitch angles allow rotors to maintain a higher percentage of their low climb-speed thrust at higher climb speeds. This could be exploited to make a quadrotor platform less sensitive to airspeed changes and reduce the trim and control system demands for effective changes in axial velocity, but would come at the costs of reduced endurance.

In very low speed and high speed descent the thrust coefficient appears to increase with descent speed, but a noticeable drop can be observed between around -2 and -5 m/s. This regime is called the vortex-ring state (highlighted on Figure 48 and Figure 49) in which the direction of the flow through the disk is not clearly defined. The loss of thrust and high thrust fluctuations make this an unstable and dangerous operating state for rotorcraft. The vortex

ring-state boundaries in Figure 48 are between vz/vh = 0.43 and 1.1 (vh = 4.6 m/s) and slightly narrower than literature values [70], possibly due to wind-tunnel interference or data sampling effects on the highly fluctuating thrust values. Wind tunnel interference effects could also play a role at the hover and near-hover values in which the propeller thrust axis is aligned with the tunnel flow direction and introduces a flow in the order of 1 m/s through the tunnel. This is below the measurement certainty of the pressure transducers (~1 Pa), but sufficient to have slight effects on low-speed thrust and power results.

Next the performance of the blade element simulation model is discussed. In Figure 48 and Figure 49 a good agreement of thrust and torque trends can be observed for climb at moderate pitch angles. The simulation results at large collective pitch angles do not show a good agreement, because, as in hover, they are severely affected by uncertainties in the nonlinear part of the lift curve slope at high local angles of attack. For the fixed-pitch results in Figure 50 an acceptable thrust agreement can be observed. Torque results for the lower rpm case deviate significantly at high descent speeds, probably driven by a combination of a poor drag model with local angles of attack and a reduced induced torque because of the slight thrust under-prediction.

The proposed local-differential method is theoretically not valid for slow descent cases in the vortex ring state because the direction of velocity through the disk is not unique and momentum theory breaks down. However, the method appears numerically stable for very small descent values in which the numerical iteration schemes for the local-differential inflow model produce a clear direction of induced velocity. The descent rates up to which the code appears numerically stable coincides with the decent rates for which the onset of the VRS was experimentally observed (Figure 48 (a)) and reported in helicopter literature [70]. This implies that the local-differential inflow model could provide an approximate solution to cases at very slow descent before the onset of a vortex ring state.

a)

b)
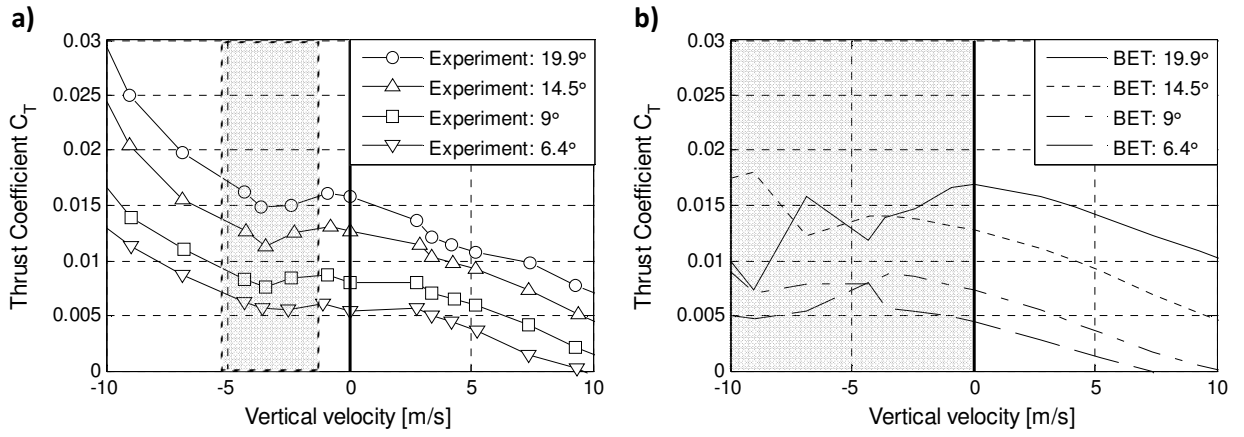
Figure 48: Comparison of experimental (a) and blade element (b) thrust coefficient in descent (left hand side) and climb for the variable pitch rotor. The expected vortex ring state area is shaded in (a), and the simulation method becomes unphysical in the shaded area in (b).

a)

b)
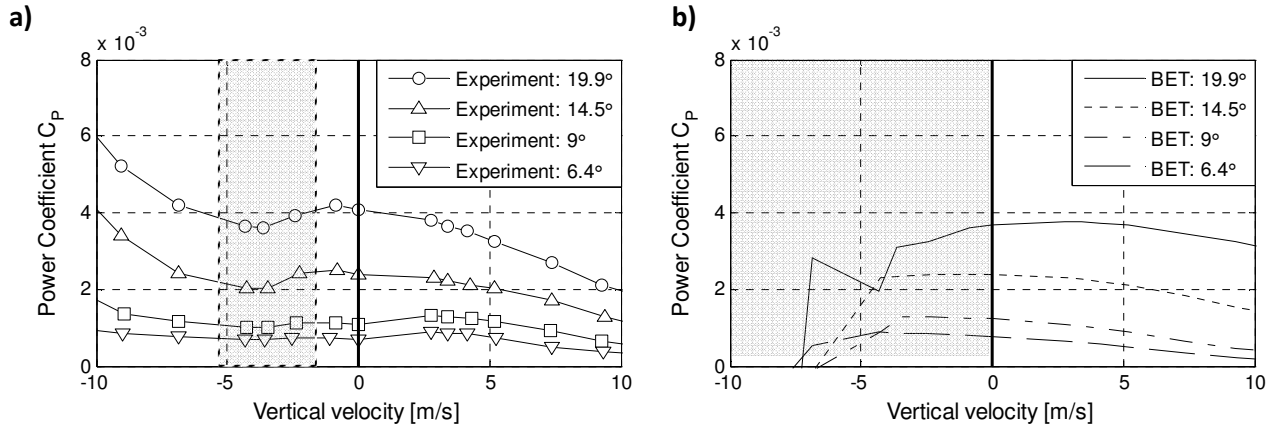
Figure 49: Comparison of experimental (a) and blade element (b) power coefficients in descent (left hand side) and climb for the variable pitch rotor. The expected vortex ring state area is shaded in (a), and the simulation method becomes unphysical in the shaded area in (b).

a)

b)
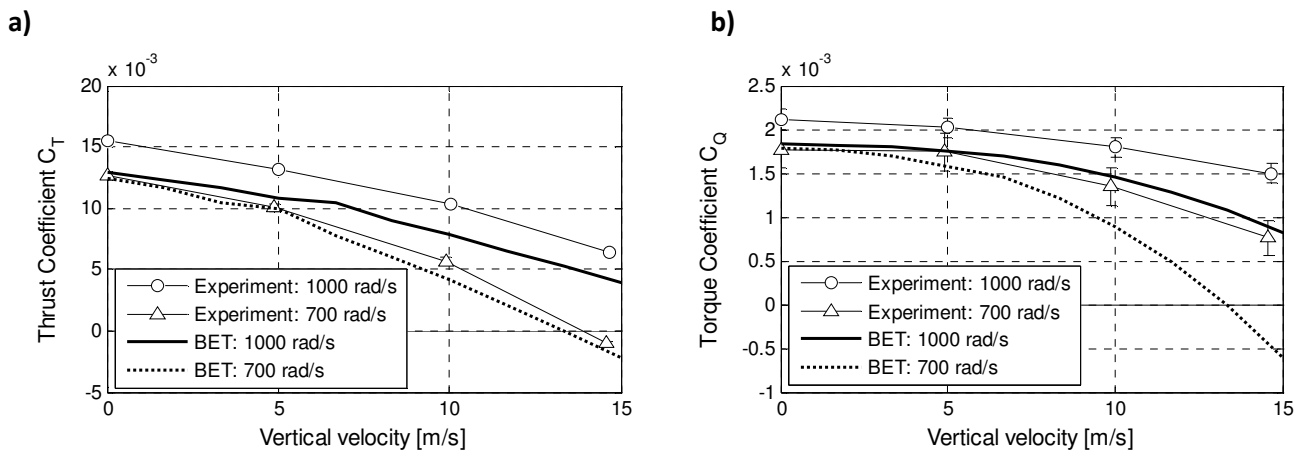
Figure 50: Experimental and simulated thrust (a) and torque (b) coefficients for a fixed-pitch APC 8x3.8 in climb.

5.4 Forward flight

5.4.1 Overview of forces and moments in forward flight

In the previously discussed cases of hover, climb and descent the flow is considered axisymmetric and the only resultant forces are thrust (F_z) and reaction torque (M_z). In forward flight the asymmetry of lift on the advancing and retreating side of the rotor and the resulting blade flapping motion give rise to hub forces (drag force F_x and sideforce F_y) as well as hub moments (rolling moment M_x, pitching moment M_y). As introduced in Chapter 3, the same hub coordinate system is used for clockwise and anticlockwise rotors.

Figure 51 shows the non-dimensional resultant forces and moments on a fixed-pitch rotor forces in forward flight (0deg disk angle of attack, rotational speed approx 6700 rpm). It is important to remind the reader that these results were obtained for a hingeless, untrimmed and relatively stiff APC 8x3.8 rotor as it is typically used on quadrotors.

a) b)
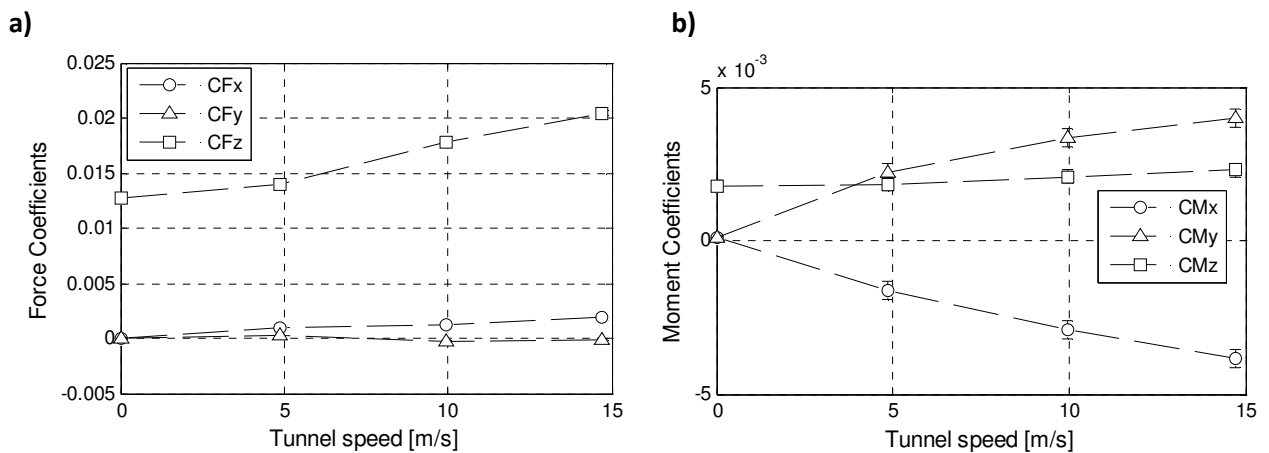
Figure 51: Non-dimensional hub forces and moments on a clockwise APC 8x3.8 fixed-pitch rotor

As the airspeed increases the thrust (CFz) and reaction torque/power coefficients (CMz) also increase, potentially driven by increases in the local angle of attack on large areas of the disk. The thrust and power trend might seem counter-intuitive, as one might expect a reduction in induced power with flight speed. But, on closer inspection, CMz increases at a smaller rate than $CFz^{1.5}$ and hence the absolute power required for a rotor trimmed at a given

thrust level would indeed reduce with increasing flight speed. A more detailed discussion of thrust and power can be found in Chapter 5.4.3.

On the advancing side the increase in local airspeed gives rise to an increase in blade loading and due to gyroscopic effects this results in a longitudinal front-to-back flapping that tilts the tip-path plane backwards (*although note that this 90 deg phase shift could be affected by the stiffness of the blade). The backwards tilt of the TPP vectors parts of the rotor thrust backwards and is a main contributor to the drag force coefficient CF_x which is about one order of magnitude smaller than the rotor thrust coefficient (at speeds of 15 m/s or about mu=0.2)

The effects of rotor coning and the longitudinal inflow variation give rise to a lateral flapping motion which typically results in the advancing side flapping down [2, 11, 52], although this could be affected by a phase lag introduced through the effects of hingeless flapping discussed above. The direction of the lateral flapping changes with the direction of rotation and contributes to the side-force CF_y. The measured side-force is very small, falls within the noise of the force-balance and will be considered negligible for the study of quadrotor flight performance.

Of particular interest in Figure 51 are the large rolling (CM_x) and pitching moment (CM_y) coefficients. These are driven by two effects: the non-uniform distribution of lift on the blade and the hub-reaction to the effective spring restraint to longitudinal and lateral blade flapping. Even at small advance ratios the magnitude of the pitching moment can reach the magnitude of the reaction torque. At higher advance ratios (15 m/s, mu<0.2) both rolling and pitching moment significantly exceed the reaction torque and can be of significant importance for quadrotor flight mechanics. A more detailed discussion of the hub forces and moments is hence included in Chapter 5.4.4.

5.4.2 Effect of modelling choices and parameters

In this section, modelling choices for two key areas specific to forward flight are discussed: flapping and inflow modelling. Both fixed and variable pitch experimental data are shown for comparison. To restrict the number of comparison cases, variable-pitch results in this section are presented for one moderate collective pitch angle (11.8 deg). This was selected for two reasons: first it is most representative of typical operating conditions, and second it ensures that the model comparison is not strongly affected by the nonlinearities in the lift-curve slope which were discussed earlier. For completeness experimental results for different pitch angles are then presented further on in this Chapter.

Flapping is discussed first. It has been shown previously that lateral and longitudinal flapping has a strong effect on the rolling and pitching moment coefficients of a hingeless rotor. The balance between lateral/longitudinal flapping is strongly affected by rpm, as implied by the ratio of the rolling and pitching hub moment (M_x/M_y) shown in the fixed-pitch results in Figure 52.
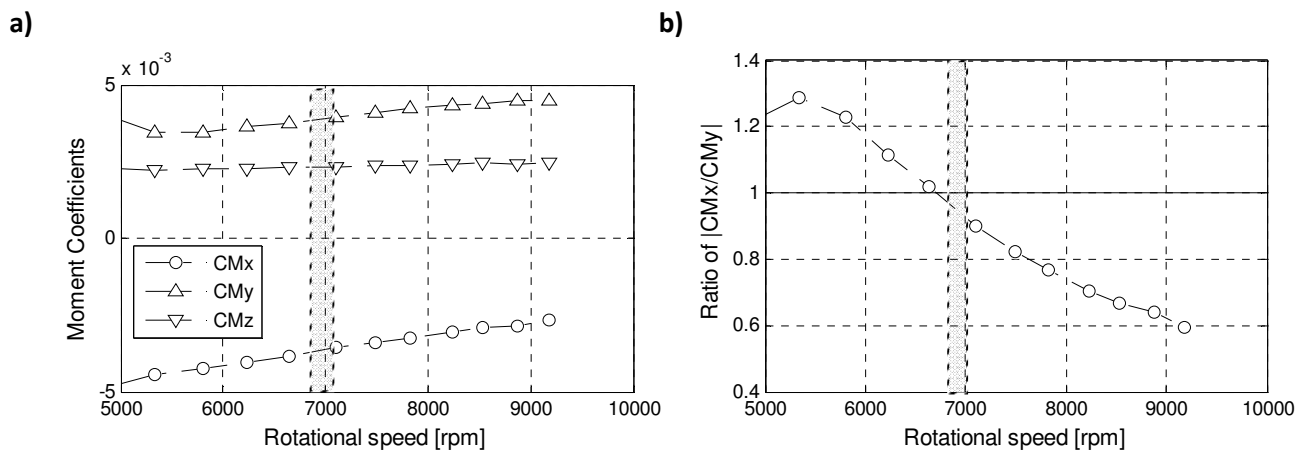
Figure 52: Moment coefficients of a fixed-pitch APC 8x3.8 rotor at about 14.7 m/s; the change in relative rolling moment vs pitching moment coefficient (magnitude) is clearly seen in b).

A simple steady-state flapping model based on Newman [11] was introduced in Chapter 3.3.3 and uses the vertical and horizontal advance ratio, lock number and flapping frequency ratio as inputs. The biggest modelling challenge lies in predicting the flapping

frequency ratio λ_β ($\lambda_\beta = 1$ for teetering rotors, $\lambda_\beta > 1$ for hingeless rotors) which is driven by the equivalent centre spring stiffness for a hingeless rotor. It is also dependent on the rotational speed of the rotor, which represents a particular challenge for variable-speed rotors. Thrust and power coefficients were found not to be particularly sensitive to the flapping frequency ratio. However, the effects on hub drag force, rolling and pitching moment were found more pronounced. These are shown in Figure 53 and Figure 54, wherein the flapping frequency ratio is varied about its predicted value of 1.35 (at nominal hover rpm). A "λ_β variable" is also used (Figure 53 (b) to adapt to the slight rpm drift during the experiment.

At higher speeds the experimental hub force coefficient CF_x is best matched with a low flapping frequency ratio ($\lambda_\beta = 1.28$), which reduces the equivalent centre spring stiffness of the rotor and hence increases the longitudinal flapping angle leading to a larger CF_x. The benefits over the baseline model are, however, small and mainly fall within the noise of the experimental measurements.

The pitching moment (Figure 54 (b) for the test case is well captured for moderate speeds where the experimental data shows a linear trend. Results appear to be not very sensitive to the flapping frequency ratio, potentially because the opposing effects of longitudinal flapping angle and equivalent spring stiffness partly cancel out under these test conditions: a low λ_β leads to a higher longitudinal flapping angle at reduced stiffness, whereas a high λ_β results in a smaller flapping angle at a higher stiffness.

The rolling moment for the test case is much smaller in magnitude than the pitching moment and affected by both flapping and the distribution of aerodynamic loading. A strong variability with flapping frequency ratio can be observed. Whilst the best agreement can be observed with a high flapping frequency ratio ($\lambda_\beta = 1.42$), other flapping frequency ratios differ significantly. This highlights the issue that the current model does not capture the

variation between lateral and longitudinal flapping very well. Rolling moments are very sensitive to this, because lateral flapping affects both: the rolling moment induced due to hingeless flapping as well as the rolling moment caused by lift imbalances between advancing and retreating side.

Nevertheless, the simplified flapping model appears to make a useful contribution for hub drag and pitching moment as long as the flapping frequency ratio is defined for a rotational speed close to the actual operation conditions. Higher order effects such as the rpm effect on the mode shape ([10], p249), are not captured.

a)   b)
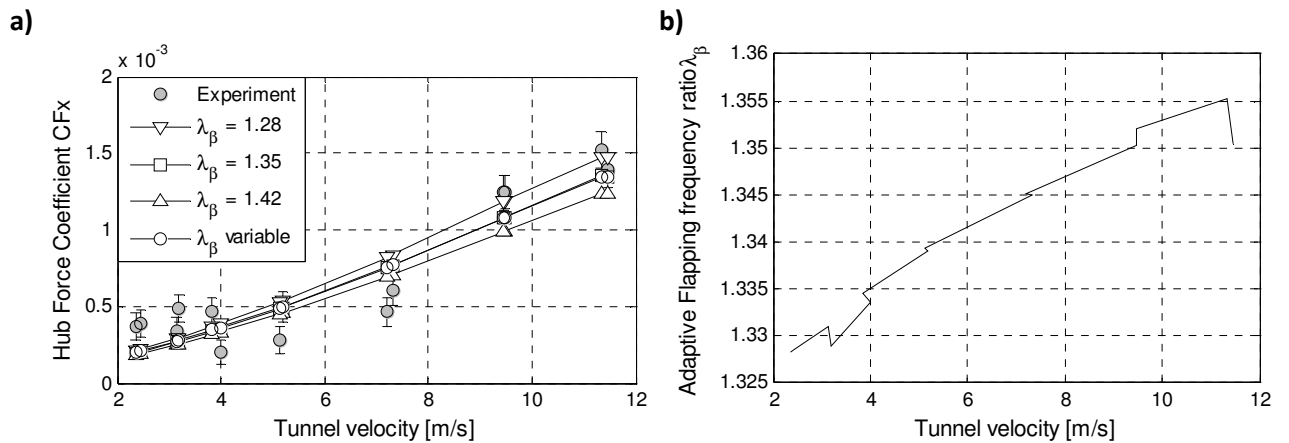
Figure 53: a) Effect of flapping frequency ratio on hub drag force coefficient CFx (11.8 deg pitch); b) variable flapping frequency ratio adapted to actual rpm (5% rpm drift).

a)   b)
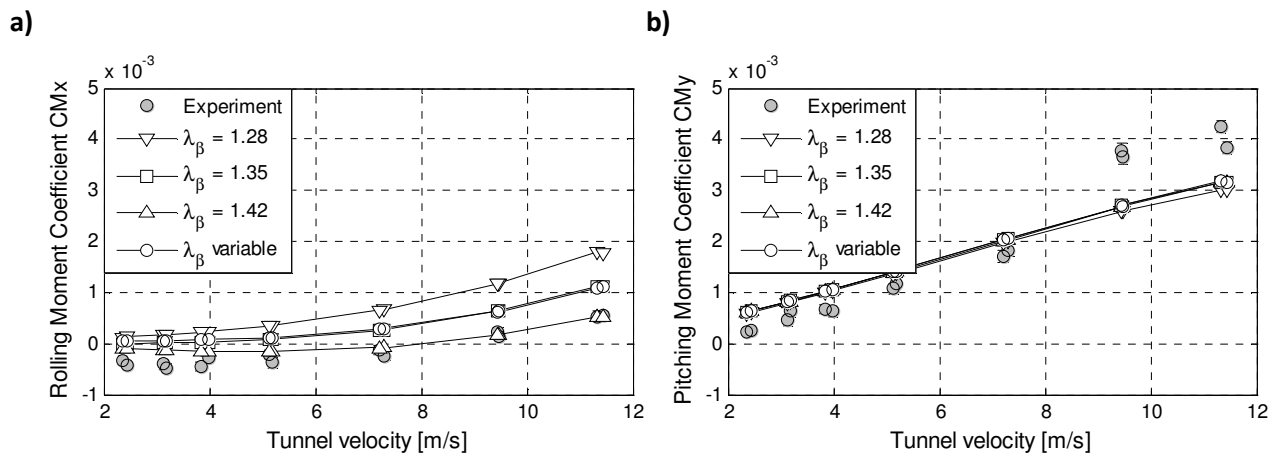
Figure 54: Effect of flapping frequency ratio on rolling moment coefficient CMx a) and pitching moment coefficient b); both at 11.8 deg pitch.

Next, various modelling choices for the time-averaged induced velocity in forward flight are discussed. The comparison includes a local differential blade element method, the Manger-Squire method and two first order harmonic inflow models (Drees and Payne) as discussed in Chapter 3.3. The latter were selected as examples of first order harmonic models based on their reported low speed performance in literature [54].

The fundamental difference between the local differential blade element model and the first harmonic models is that the former is based on a numerical convergence of loading and inflow on a blade element level, whereas the other models are applied in a way that ensures global convergence on a disk level. The local differential model makes the *"gross assumption that the relationship between the change in momentum and the work done by the load across the element applies locally as well as globally"* ([7], p124) and is the most radical implementation of the blade element assumption of independent elements. The Mangler-Squire model is "based on the incompressible, linearized Euler equations to relate the pressure field across the disk to an inflow" ([2], p161). The thrust coefficient for the Mangler-Squire method is updated iteratively to ensure convergence of C_T. An equal contribution of Type-1 and Type-3 loading was assumed. A severe limitation of the Mangler-Squire method is that it can only be applied to advance ratios >0.1.

A comparison of force and moment coefficients against experimental data is shown in Figure 55. The first order harmonic and Mangler & Squire inflow models show a very similar performance and there is good agreement between experimental and modelled thrust coefficient data, especially for medium and high speeds. The baseline (local-differential) model offers best thrust performance at very low speeds and offers an acceptable agreement for higher speeds. It also shows best agreement against experimental torque coefficients for low and medium speeds. At high speeds the Mangler- Squire model offers slightly improved

results, whereas the first order harmonic models can only capture the torque trend with a significant offset in the modelled torque coefficient.

The rolling moment prediction suffers from the same difficulties as discussed in the flapping modelling section. Whilst the local-differential model appears to match experimental results most closely the complexity of lateral/longitudinal flapping phase shifts and its effects on the advancing/retreating side blade element loading limits the confidence in the rolling moment prediction. This uncertainty is acceptable for the present quadrotor performance application, since rolling moments for the four rotors tend to cancel out.

At low to medium speed the best hub force CFx and pitching moment agreement with experimental results appears to be provided by the local-differential model. The baseline model shows a linear trend with pitching moment which appears dominated by the pitching moment induced from hingeless flapping. The first order models are influenced by nose-up pitching moments from hingeless flapping and the effects of the longitudinal inflow distribution. The inflow distributes increases the local blade angles of attack at the front of the disk and explains the initially higher pitching moment prediction. The reason for the reversing trend in pitching moment could, however, not be determined conclusively. At high speeds the magnitude of the experimental pitching moment is best reflected by the Mangler & Squire method.

None of the low-order methods provided an excellent agreement for all test conditions. At higher speeds the Mangler & Squire model gives the best prediction of thrust and power, but because it can only be used for advance ratios greater 0.1 it is unsuitable for large parts of the practical quadrotor flight envelope. For the test cases and velocity range analysed it appeared that a local-differential model could provide a better overall agreement than a first order harmonic inflow model. This can be explained as follows:

- Pitching moments on the relatively stiff hingeless test rotor mainly originate from flapping, rather than the longitudinal inflow distribution.

- For a rotor with untwisted blades and a high C_T, better power predictions can be achieved if the inflow variation along the radius is matched to the blade loading using a local-differential model, than if it is based on a mean disk inflow and a first order harmonic inflow model.

The pure local-differential model, despite its limitations and shortfalls on the longitudinal inflow distribution, appears to provide a robust method which enables a seamless transition from good hover predictions to acceptable steady-state forward flight force/moment predictions. It was thus picked as baseline case for the remainder of this study.

5.4.3 Thrust and power relationships

In this section, thrust and power relationships with airspeed, disk angle and flight speed are presented and compared qualitatively against simulation results based on the experimental rpm, pitch and airspeed conditions. The basic principles suspected to drive this behaviour are discussed, but a detailed analysis of the underlying flow physics is outside the scope of this work.

Three different disk angles of attack (0,-15,-30 deg) representative of typical quadrotor flight conditions are selected for comparison. Thrust results for constant pitch and similar rpm in Figure 56 show that for 0 deg disk angle the thrust coefficient increases with airspeed. This appears to be driven by an increase in the local blade angle of attack as a result of a reduced inflow angle. This reduction in inflow angle is caused by the addition of a free-stream component to the tangential velocity and changes to the inflow component perpendicular to the rotor disk. As the magnitude of the disk angle is increased (nose down disk orientation), the thrust coefficient gradient changes sign, and beyond a -30 deg disk angle the thrust coefficient reduces with increasing airspeed.

a)

b)

b)

c)

d)
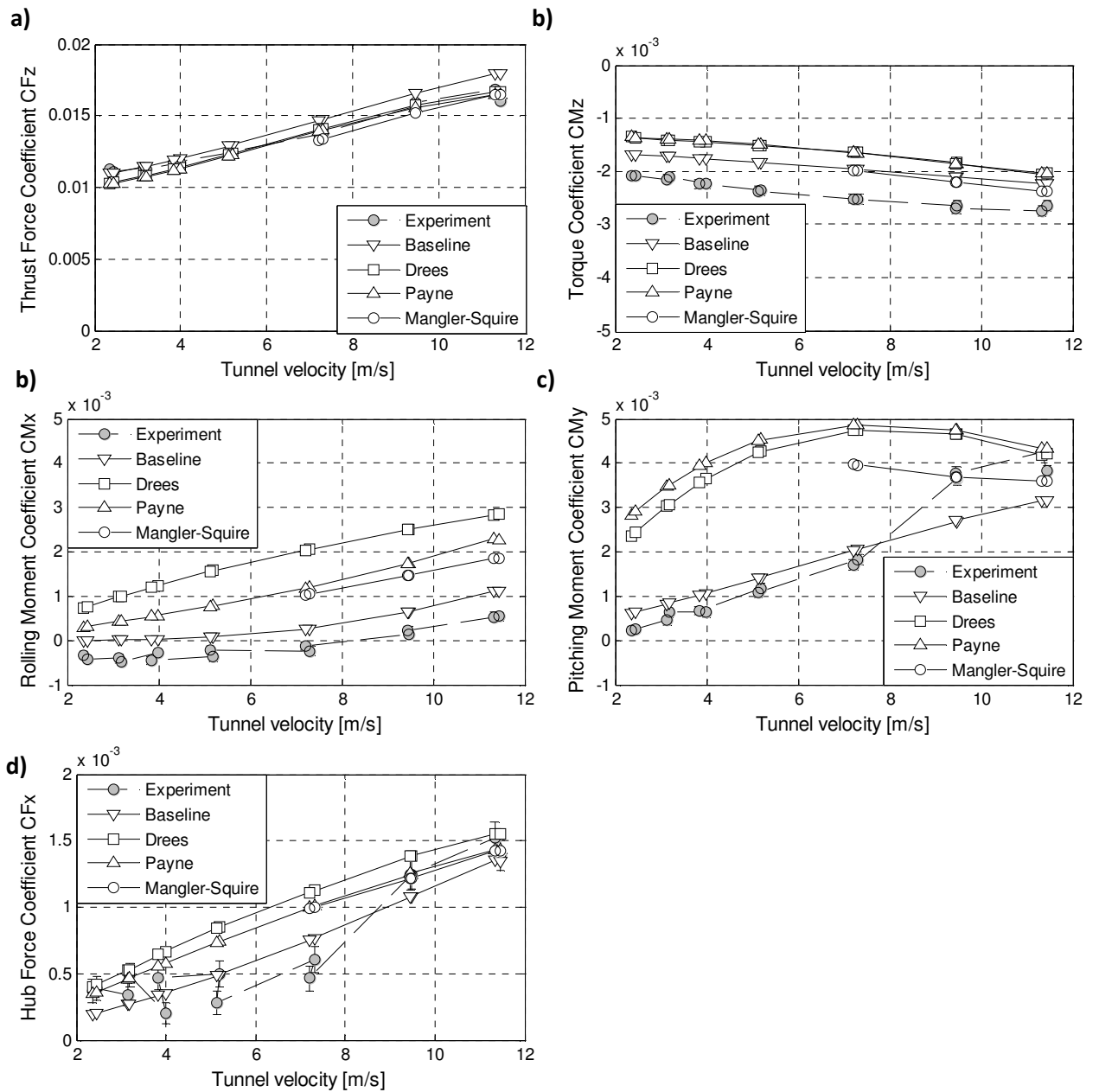
Figure 55: Effect of inflow modelling choice on rotor (hub) force and moment coefficients. All at 11.8 deg

pitch and with λ_β = 1.35.

This can be explained as follows: A more negative disk angle increases the flow normal to the rotor disk, which increases the inflow angle and hence results in a reduction in the blade angle of attack. The higher the disk angle the more the rotor starts behaving like in the axial climb case (-90 deg disk angle) and a rotor at a high (negative) disk angle thus also has a maximum airspeed at which positive thrust can no longer be produced.

Increasing collective pitch (Figure 56) increases the local blade angle of attack and hence thrust coefficient. Whilst the simulation method captures most of the thrust coefficient trends, it is compromised in situations with high angles of attack, such as the high collective pitch thrust coefficient at 0 deg disk angle. A notable feature of the experimental results is that increasing the disk angle results in a noticeable drop of the low speed thrust coefficients, which is most pronounced for the -30 deg disk angle ("drop") on Figure 56 (e). This was not expected and is suspected to be a result of uncorrected effects of the rotor on the wind tunnel flow.

The torque (=power) coefficient data shown in Figure 57 exhibit a similar trend as the thrust coefficient, although effects are less pronounced, and the trend appears to be caused by similar angle of attack mechanisms. The simulation model captures the overall trend in the reaction torque, however, the correlation becomes less good as the disk angle increases.

The results presented in this section lead to important conclusions for quadrotor flight performance: A rotor at a small negative disk angle of attack experiences a greater increase in thrust coefficient than in power coefficient as airspeed is increased. Hence it needs less power for constant thrust at higher speeds (at this stage all further trim considerations, like the need to compensate drag with additional thrust, are ignored). Higher (negative) disk angles of attack, on the other hand, require more power as flight speed is increased. A full discussion of the resulting quadrotor power curve is found later on in Chapter 6.
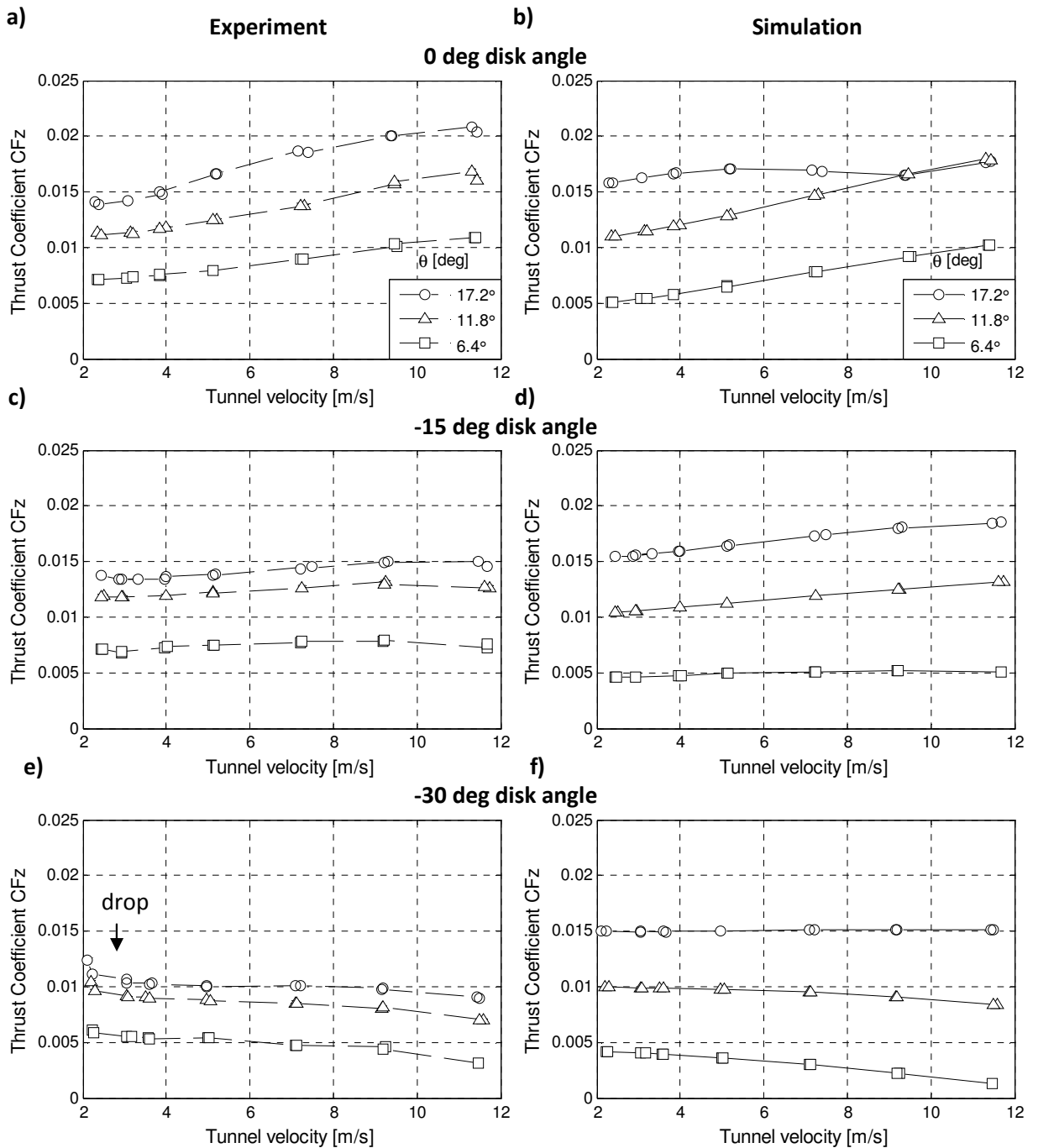
Figure 56: Thrust coefficient change with airspeed and disk angle of attack; pitch held constant and rpm for

each pitch fixed at similar rotational speeds.
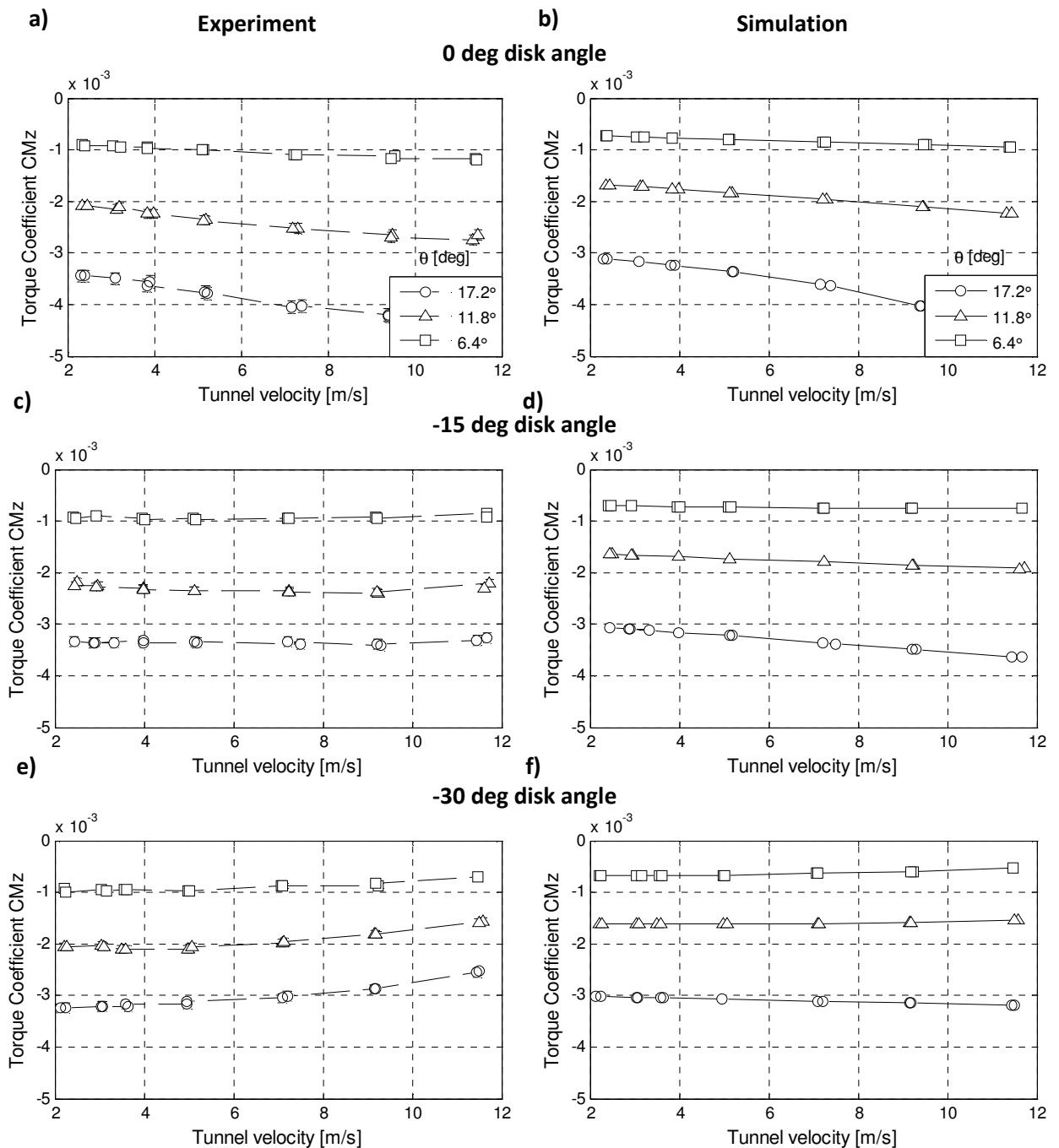
Figure 57: Torque coefficient change with airspeed and disk angle of attack; pitch and rpm were controlled.

To show the implications of the thrust/power trends under practical consideration the rpm and power/thrust ratio of the baseline method were compared against data extrapolated from experimental force/power coefficients. The simplified analysis shown in Figure 58 considers a fixed 2.5 N thrust requirement at three different disk angles (0,-15,-30 deg). Agreement for 0 and -15 deg is acceptable, but the power ratio at -30 deg is not captured well. The experimental results for high disk angles show a sudden jump in power/thrust between 2-4

m/s which is maintained throughout the velocity range. As mentioned earlier these experimental effects cannot be explained conclusively, but a likely explanation could be that the rotor at higher disk angles adds more momentum in the tunnel flow direction and hence has a stronger impact on thrust/power results.
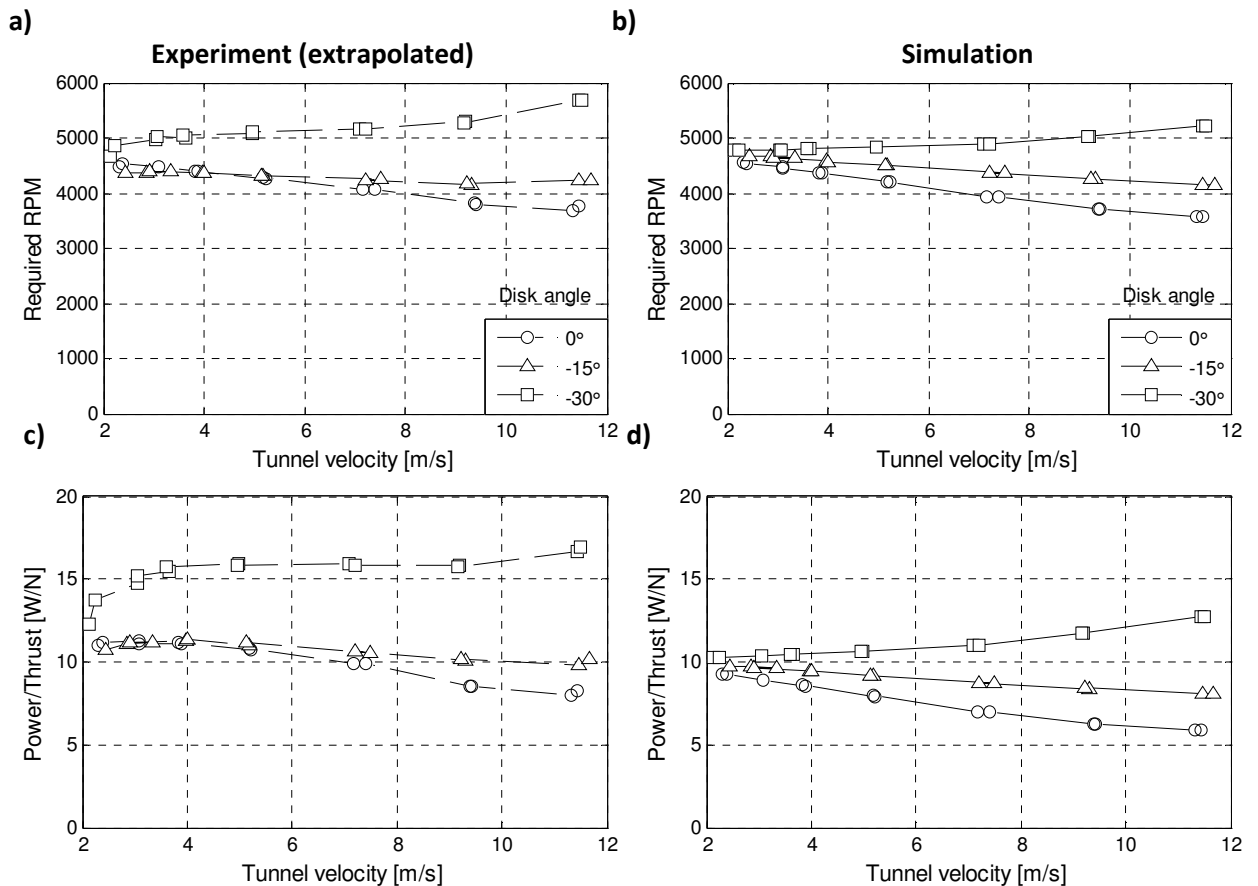
Figure 58: Comparison of trim rpm and power/thrust for different disk angles and experiment/simulation;

All at 11.8 deg collective pitch, thrust fixed at 2.5 N.

5.4.4 Hub forces and moments

In this section, rotor drag force, rolling and pitching moments acting at the rotor hubs are discussed. The discussion goes beyond aspects covered in previous sections by including the effects of collective pitch, disk angle and airspeed. Before going into more detail the reader is reminded of the experimental and modelling limitations: Hub forces are typically small compared to the rotor thrust which makes measurements more difficult and increases measurement noise. They are also more vulnerable to disturbances and residual drag from the

support brackets and sensors. Furthermore, effects might not be unique to one force axis alone, but subject to a certain degree of coupling due to flapping. Some of these effects go beyond what can be covered by an uncertainty analysis and hence care has to be taken when interpreting the data. For the simulations there is a strong influence of flapping and the inflow distribution, as discussed previously, which leads to modelling difficulties.

The drag force (CF_x) coefficient, as shown in Figure 59, increases with airspeed, but its magnitude decreases with an increasing (negative) disk angle. This appears driven by the reduction in total thrust coefficient that the rotor experiences at negative disk angles. The simulation model captures a near linear trend. For low and moderate collective pitch angles an acceptable agreement of the high-speed CF_x can be shown, but the drag force coefficient for large collective pitch angles is overestimated.

The rolling moment coefficient CM_x (Figure 60) also increases with airspeed, but the magnitude decreases with negative disk angles. The magnitude of the rolling moment coefficient is much smaller than the pitching moment coefficient and the difficulty in modelling the effects of lateral inflow and flapping is shown by the change of sign from positive to negative rolling moments that can be observed on the experimental data at low speeds. The simulation provides acceptable results for low and moderate pitch angles and disk angles, but breaks down at larger disk angles (-30 deg). Given the limited importance of the rolling moment for quadrotor flight performance studies, the lack of accuracy in this aspect of the modelling is seen as acceptable.

The pitching moment coefficient CMy (Figure 61) shows a similar overall trend as CFx and CMx: It increases with airspeed and decreases with (negative) disk angle of attack. The simulation model captures the trends for low/moderate collective pitch angles and low (negative) disk angles of attack, but significantly overestimates the pitching moment coefficient for high collective pitch angles.

The analysis above shows hub forces and moments follow similar trends which appear to be strongly influenced by the effect of the steady state flapping angles. Whilst the simulation model appears to capture the key trends at moderate collective pitch angles, there are clear limitations for more extreme flight conditions involving large collective pitch angles at high negative disk angles.
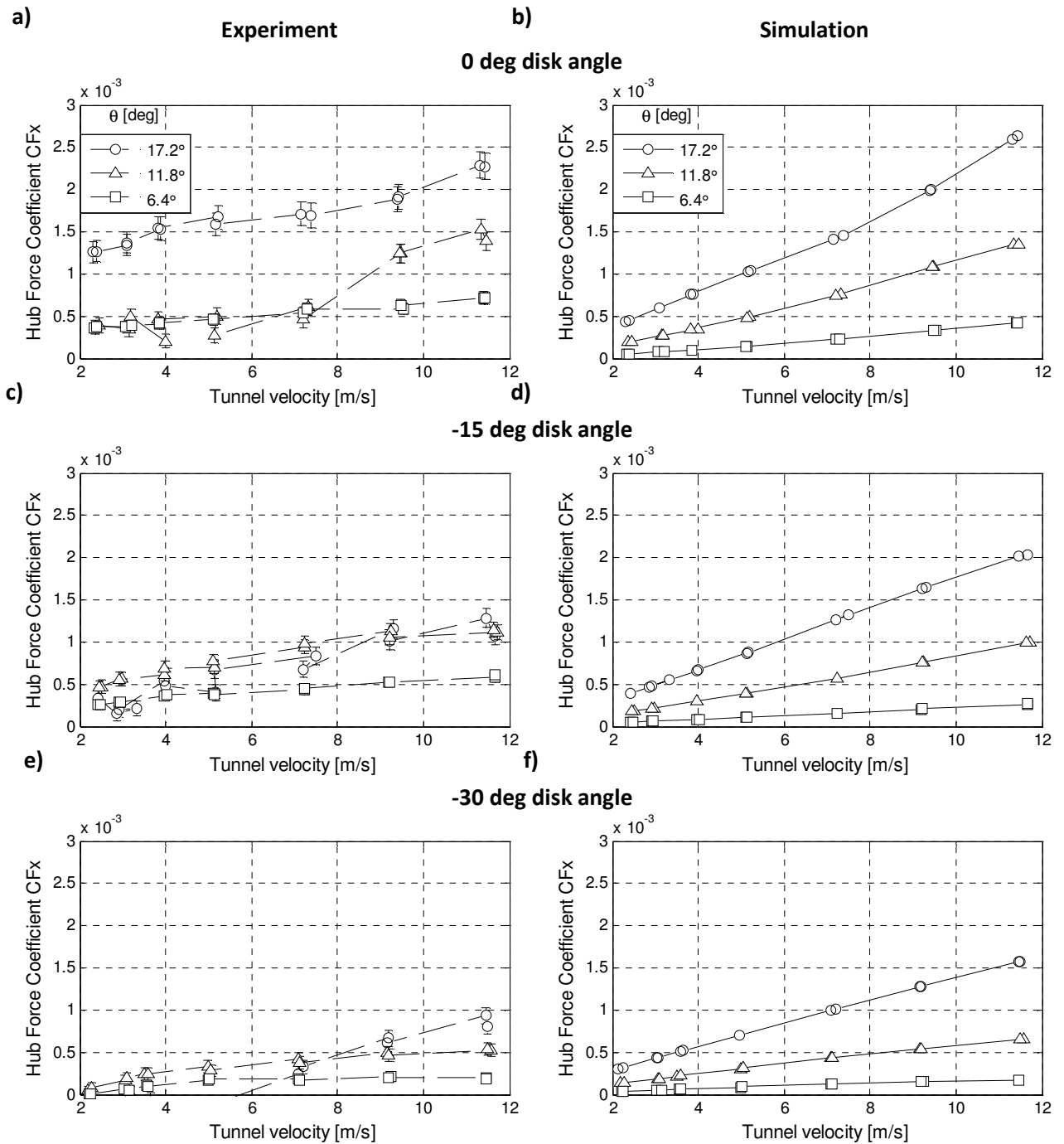
Figure 59: Rotor hub force coefficient CFx (drag) with disk angle and airspeed.
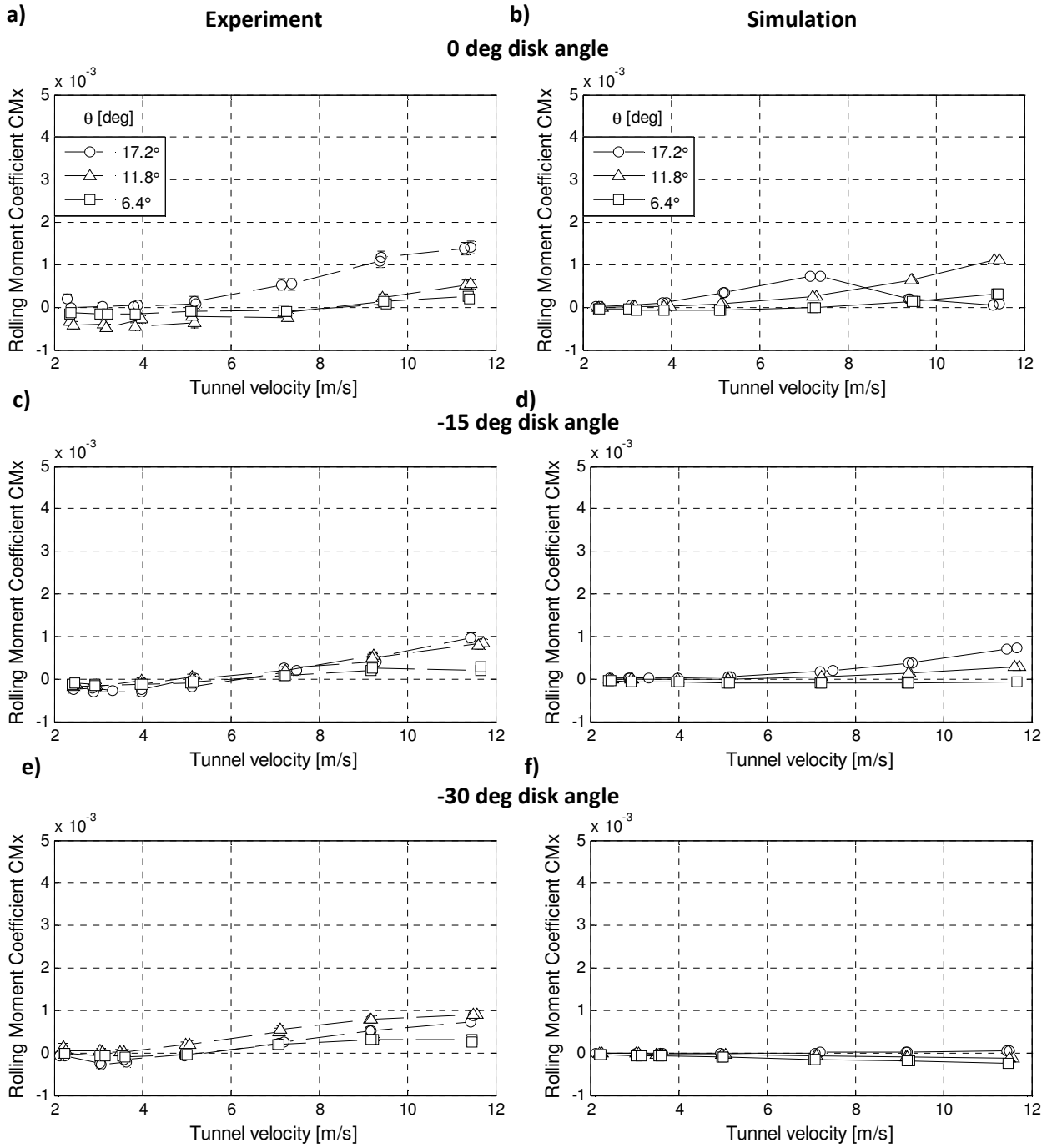
Figure 60: Rotor rolling moment coefficient CMx with disk angle and airspeed.
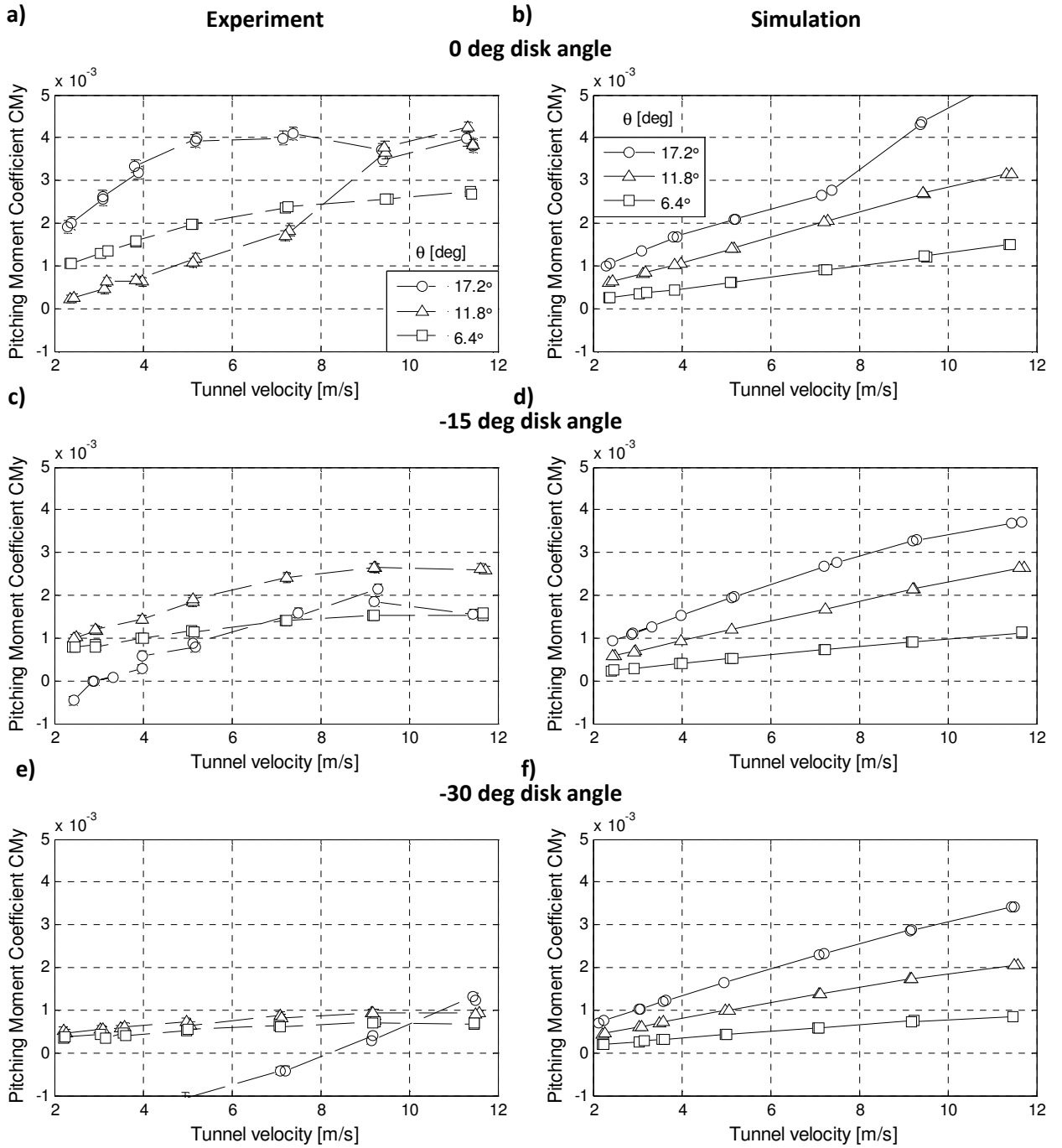
Figure 61: Rotor pitching moment coefficient CMy with disk angle and airspeed.

5.5 Rotor aerodynamics summary

In this section, the findings from the rotor aerodynamics chapter are summarised. The experimental results are considered first with a focus on the implications on quadrotor flight. Following this an overview of the key modelling experiences is presented.

5.5.1 Summary of measured rotor forces and moments

- Hover thrust/torque on the APC 8x3.8 fixed-pitch rotor appear to be affected by aeroelastic deformation in the blade twist: the thrust varied with rpm to a power greater than 2.

- For the collective pitch rotor the hover thrust increases linearly with collective pitch up to about 15 deg where the slope reduces.

- In axial climb there is a maximum speed at which positive thrust can be no longer produced. A large collective pitch angle increases this maximum speed and reduces the variation of thrust with airspeed.

- A large negative (nose down) disk angle in forward flight leads to a significant increase in power demand for a constant thrust.

- Forward flight pitching moments, rolling moments and drag force can be significant for a typical hingeless quadrotor rotor:

  o The rotor drag force arises from the deflection of the tip-path plane and can be larger than 10% of the total thrust at velocities of about 15-20 m/s.

  o The pitching moment largely arises from the effective stiffness of the blade restraining its longitudinal flapping motion. Depending on rotor rpm and collective pitch, the pitching moment is of the same order of magnitude, and sometimes significantly larger, than the reaction torque; the pitching moment is independent from the direction of rotation.

  o The rolling moment arises from two key sources: the stiffness of the blade restraining the lateral flapping motion and an imbalance of local thrust on the

155

advancing and retreating side. The magnitude of the rolling moment increases with an increasing flapping frequency ratio and can exceed the magnitude of the blade pitching moment for low rpm cases; the direction of the rolling moment changes with the direction of rotation, which largely cancels out the rolling moment on a quadrotor.

- o For flight performance purposes the pitching moments are most significant, since they are additive and do not cancel out for counter-rotating rotor pairs.

5.5.2 Summary on the blade element modelling

- For a rotor operating at a high C_T and with untwisted rotor blades, a local-differential blade element method provides an improved thrust and torque prediction compared to a uniform inflow model.

- For typical quadrotor rotors operating at high C_T the effects of a tip-loss model appear more pronounced than on low C_T rotors; a Prandtl tip-loss model was found suitable.

- A 2-d lift model based on x-foil was found suitable if a Reynolds number variation was included; However, the profile drag for the test rotors was underestimated using this method and better results could be obtained with a polynomial drag model highlighting the drag variation with angle of attack.

- The local-differential blade element model is numerically stable for very small descent speeds, but is invalid around the vortex-ring state.

- In forward flight the Mangler & Squire model provides the best rotor forces/power agreement at high speeds, but it's only valid for advance ratios greater than 0.1 and therefore impractical for quadrotor forward flight studies.

- The local-differential model appears to be an acceptable low-order method that gives continuous results for hover and forward flight; the reduced fidelity in the longitudinal

inflow distribution appears acceptable at the velocity range of interest because pitching and rolling moments appear dominated by hingeless flapping.

• The model captures the key characteristics of the hub forces and moments at moderate collective pitch and disk angles, but the coupling between rolling and pitching moments is poorly represented.

• The model breaks down at high angle of attack cases where the post-stall model is insufficient.

• One of the key strengths of the local-differential model is that no a priori knowledge is required, which makes it a suitable low-order tool for performance analysis and initial stage design comparison.

Chapter 6: Quadrotor Flight Performance

The objectives of this chapter are:

>   *To understand the limits to the flight performance of current quadrotors. To investigate ways to reduce forward flight power requirements and increase maximum flight speed through a) configuration design changes and b) the introduction of collective pitch capabilities.*

6.1   Chapter overview

Whilst the previous chapter focused on the aerodynamic forces and moments on single rotors under prescribed operating conditions, this chapter focuses on the performance of an entire quadrotor system including the effects of motor efficiency, fuselage aerodynamics and trimmed level flight conditions. Unless stated otherwise all analyses are for fixed-pitch/variable-speed rotors. This chapter is organised in four main parts:

The first part, Chapter 6.2 presents experimental findings on quadrotor performance:

First the motor efficiency as a function of operating conditions is quantified and found to be a major source of losses when compared to aerodynamic losses and ideal rotor power.

An experimental study of the effect of rotor spacing and flight speed on rotor-rotor interference is presented which suggests that interference effects follow similar trends as on tandem helicopters in forward flight: the front rotor experiences a slight thrust increase, whereas the rear rotor decreases in thrust when compared to an isolated rotor. For most rotor spacings of practical interest these interference effects are, however, small and fall within the measurement uncertainty of the force balance.

Experimental data for the body aerodynamics of two different quadrotor fuselages is presented and used to populate the semi-empirical model introduced in Chapter 3.4. Contrary

to the current state of the art, which typically ignores quadrotor fuselage aerodynamics, it is shown that fuselage drag and downforce can be significant compared to body weight.

Experimental trim and power results for a wind tunnel based quadrotor test-rig are presented and it is shown that large vehicle angles of attack are required to trim the vehicle in forward flight. The resulting u-shaped power curve is similar to SMR helicopters, but a closer inspection reveals that rear rotors typically run at significantly higher power levels to compensate for the nose-up pitching moment from hingeless rotors. This causes the rear rotors to reach thrust saturation first and this represents one of the main limits to the top speed of conventional quadrotors.

Using experimental power curves it is demonstrated that the useful mission duration could be greatly improved by exploiting maximum range and minimum power conditions for quadrotor mission planning, a strategy commonly used for conventional helicopters has not yet been reported for quadrotors.

The second part, Chapter 6.3, analyses the effects of atmospheric density and battery discharge level. A low density case was found to significantly increase the power in low speed, whilst reducing the power demand at high speed flight near the top speed. The effect of battery discharge on the flight envelope was found to be negligible for correctly sized batteries.

The third part, Chapter 6.4, analyses the power breakdown in forward flight and evaluates configuration design strategies to minimise forward flight power demands and increase the top speed. It was found that the rapid rise in power at high-speed demand was due to the large vehicle angles of attack required at this flight condition, which pushes up the required induced/propulsive power. The two most promising design strategies appear to be reducing the blade flapping frequency ratio, for example by using a teetering rotor system, and

introducing a tilt angle between rotors and the airframe which minimises the effective drag at high vehicle angles of attack.

The final part, Chapter 6.5, investigates the effects of introducing collective pitch capabilities on quadrotors. This was found to significantly improve the maximum speed and high-speed power requirements, but a wide cost analysis including the collective pitch mass penalty suggests there could be small power penalties in nominal hover and low-speed forward flight.

6.2 Experimental analysis of quadrotor performance

6.2.1 Motor integration: motor efficiency effects and optimum hover settings

For a realistic analysis of the flight performance of an electric vehicle it is important to establish the link between mechanical and electric power demands and pay close attention to the electric power requirements.

The efficiency of an electric motor changes with rotational speed and torque demand according to the relationships introduced in Chapter 3.5. The effects of this are illustrated in Figure 62 where the same thrust magnitude is achieved with a moderate-collective/high-rpm and a high-collective/low-rpm: The high collective case not only increases the aerodynamic losses and hence mechanical power – it also loads the motor in a less efficient high torque/low rpm setting which amplifies the electric power penalty. Figure 63 was used to obtain the collective/rpm combination for minimum hover power and this value was used as baseline case for Chapter 6.4. From Figure 63 it is clear that electric power has to be considered to fnd the "true" minimum power point. It is important to point out the results this chapter represent the particular motor setup as introduced in Chapter 4 and electric losses are higher than current high-end brushless motor systems.

a)

Moderate collective (11.7deg, T = 2.44N)

b)

High collective (22.6deg, T = 2.42N)
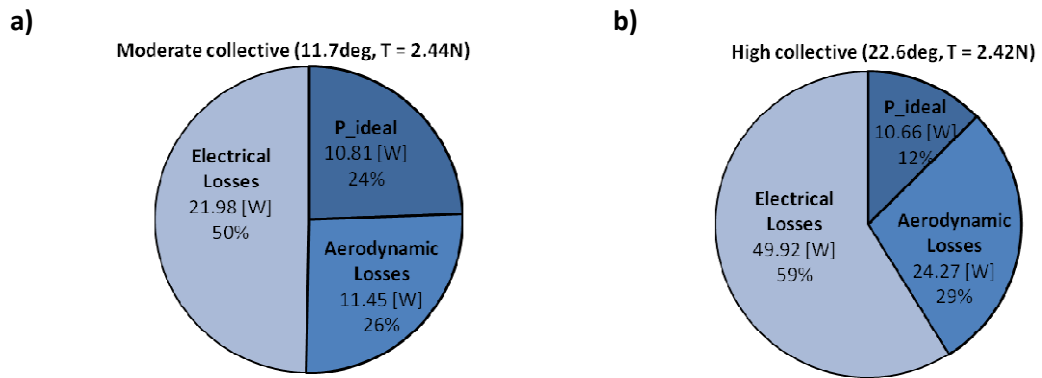
Figure 62: Power breakdown for two collective-pitch hover scenarios.

a)

b)
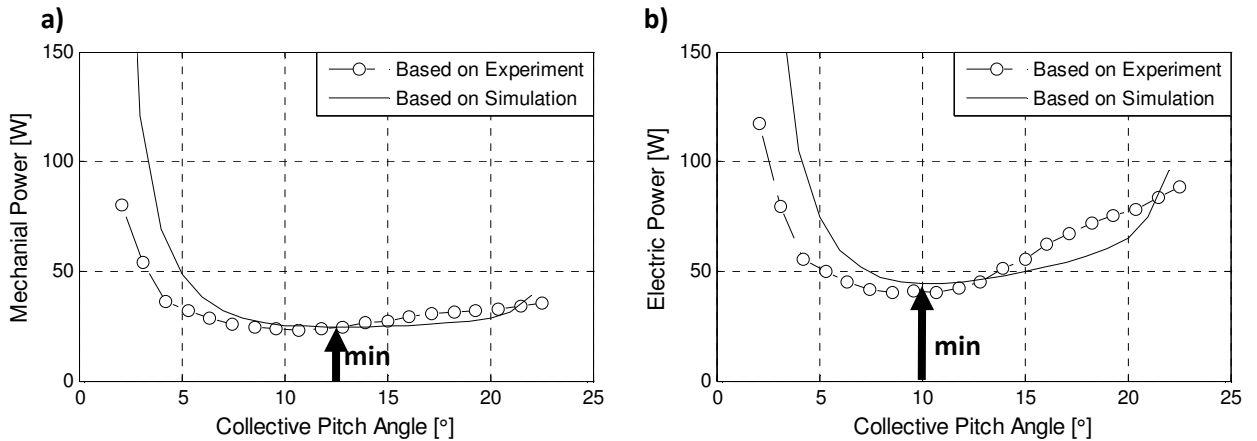
Figure 63: Minimisation of hover power requirements, experimental values extrapolated from the C_T/C_Q.

Figure 64 shows the performance of the electric power model against experimental results. Using the motor parameters supplied by the manufacturer ("Power Model" curve) a reasonable agreement can achieved. Significantly better results could, however, be achieved by using an experimentally determined internal resistance value (0.47 ohm as opposed to the 0.235 ohm), that captures the motor-ESC and integration effects – the same strategy has also been reported by Stepaniak [24].

a)

b)
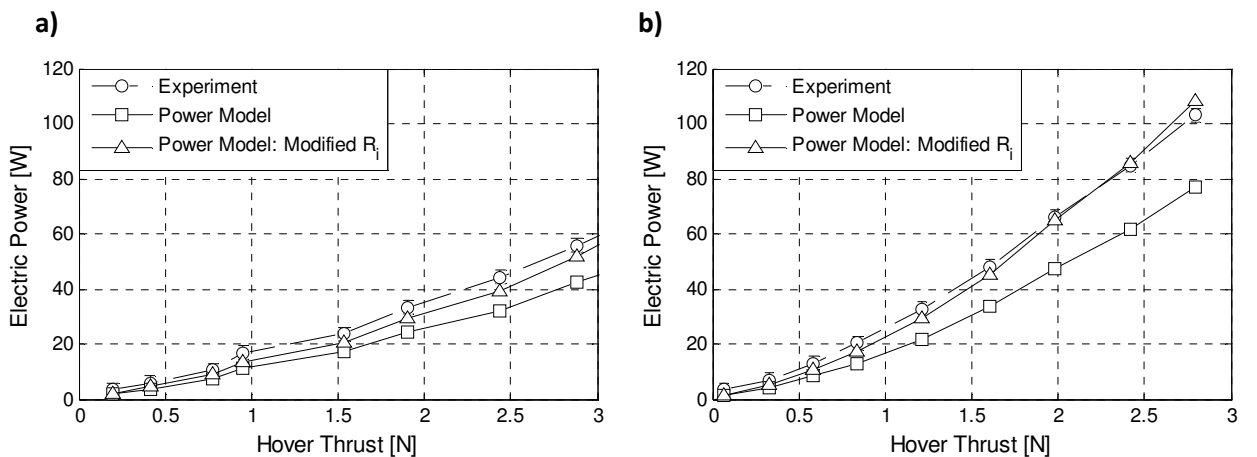
Figure 64: Performance of the electric motor model a) high pitch (22.6 deg), b) moderate pitch (11.7 deg).

161

6.2.2 Rotor-Rotor interference effects

6.2.2.1 Background

Whilst the rotor interference on tandem rotors has received considerable treatment in the past (for example in [2, 8, 62, 63]) a lot of this work is for overlapping rotors and there appears to be no literature dealing with the rotor-rotor interference on typical quadrotor configurations. This section presents the results of a systematic wind-tunnel study of the effects of rotor spacing and flight speed.

6.2.2.2 Interference effects in hover

First, results for hover are presented. For this case the quadrotor model was mounted in the wind-tunnel test sections with the flow off, as described in Chapter 4. For hover symmetric flow conditions and hence a similar behaviour for all rotors is expected. Figure 65 shows the change of the individual rotor thrust coefficient and figure of merit with rotor spacing and leads to two important observations:

- Whilst displaying a small amount of variability, front and rear rotor do not exhibit any measurable trend with rotor spacing; hover interference effects on thrust and power appear negligible.

- The side rotor, which moves closer to the tunnel walls as the rotor spacing is increased, shows a measurable change in thrust and efficiency with increased rotor spacing.

The implication of the latter is that the ratio of tunnel to rotor area, despite being significantly smaller than on previous tandem rotor experiments, is too small to avoid individual side rotor results being affected by a reduction in the rotor distance to the tunnel walls. In the absence of a bigger tunnel the remainder of the interference study had to be limited to the effects on the front/rear rotor on a plus configuration.

The lack of a measureable change in rotor efficiency with spacing (Figure 65 (b) disagrees with early tandem rotor research by Dingeldein [62] who reported a tandem rotor with a 1.03 d/D spacing to show measurable power benefits in hover and claimed this on larger effective disk area than 2 A_{disk}, but also stated that *"This favourable interference effect is probably confined to a true hovering condition and probably disappears at extremely low forward speeds. It is therefore not expected to be of any practical importance".* Based on simulations Griffiths & Leishman [71] also reported a small reduction (<4%) of induced power overlap factor for closely separated tandem rotor. The reason for this discrepancy is unknown, but small effects could fall within the measurement noise of the force balance and further discrepancies could be caused by the four-rotor arrangement, different rotor geometries and the wind tunnel test conditions.
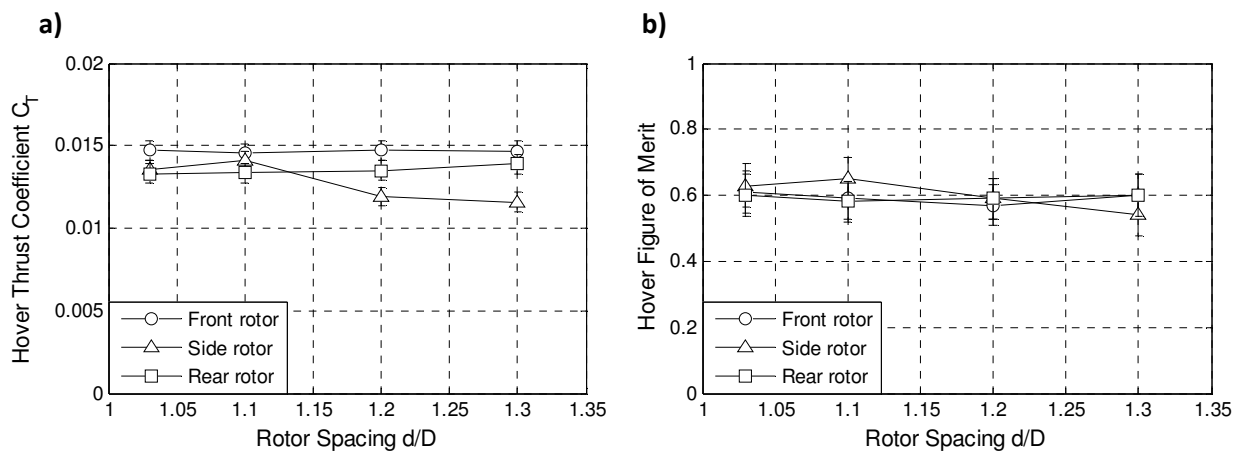
Figure 65: Rotor interference effects vs. rotor spacing in hover.

6.2.2.3 Interference effects in forward flight

Figure 66 shows how rotor spacing and flight speed affect the ratio of front/rear rotor thrust and power compared to a single rotor case. The data experiences a significant amount of uncertainty and measurement noise, but the general trend suggests that a small spacing slightly increases the front rotor thrust and causes a small decrease in rear rotor thrust at low speeds. The front rotor power coefficient ratio (Figure 66 (c) decreases with rotor spacing, albeit at a lower rate than the front rotor thrust coefficient ratio (Figure 66 (a) to power of 1.5 – this implies that a small rotor spacing would reduce the front rotor power requirement. The

opposite effect, although less pronounced, was measured for the rear rotor: Because the thrust coefficient ratio at low speeds and small rotor spacing is reduced, the nearly constant power coefficient ratio (Figure 66 (d) would cause an effective increase in rear rotor power.

The trend of these findings agrees with previous experimental work on tandem helicopters, that claims that the front rotor produces more thrust at forward speeds [63], but because the aft rotor operates in the slipstream/downwash of the fore rotor its power requirements tend to be bigger [72].

Like on tandem rotors [63], the net effect of rotor-rotor interference on total quadrotor thrust and power is expected to be small for most flight conditions.
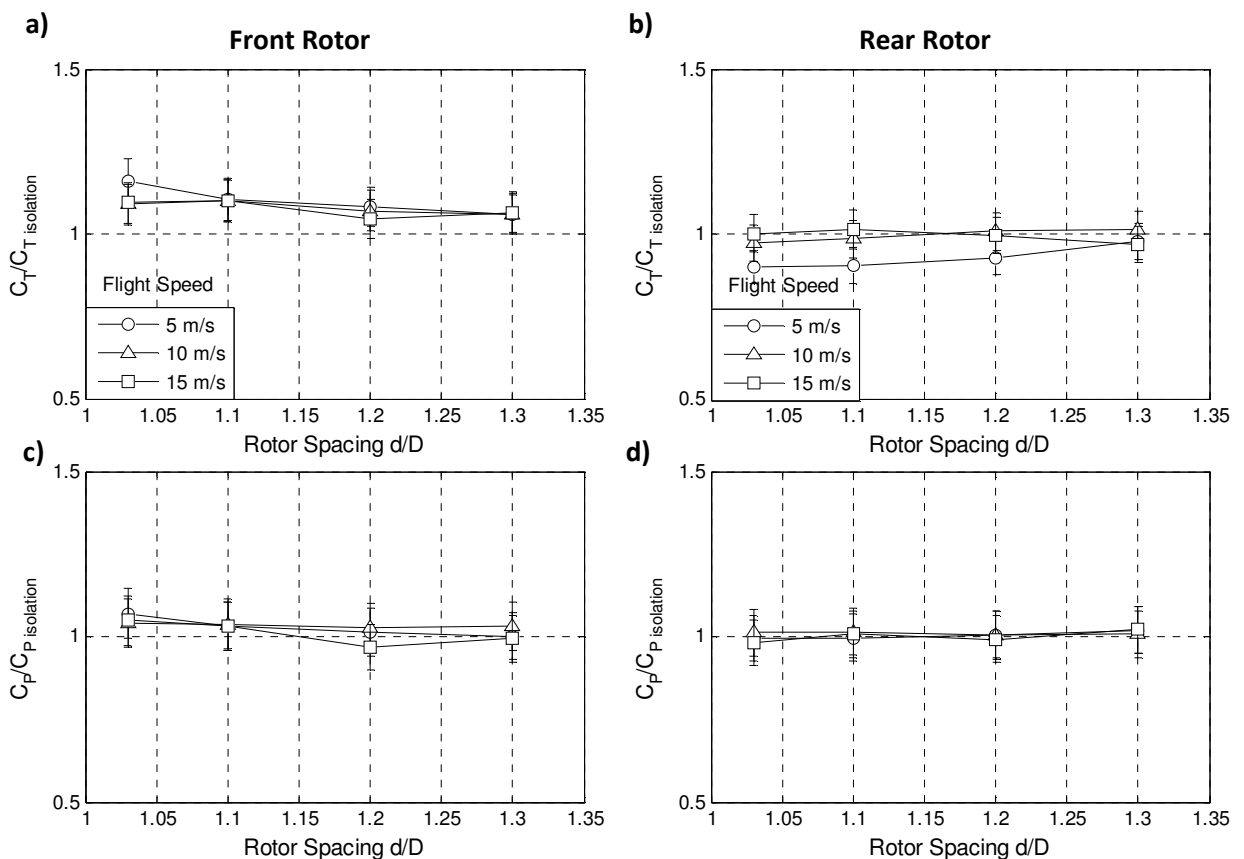
Figure 66: Interference effects on front and rear rotors with rotor spacing and flight speed (+ configuration).

6.2.3 Quadrotor airframe aerodynamics

6.2.3.1 Background and Scope

The quadrotor fuselage forms the biggest geometric part of a typical quadrotor vehicle and often has features, like exposed motors, antennas, wiring and sensors that produce significant drag. Additionally, the importance of drag increases for small vehicles due to the square-cube law as discussed previously. Yet, up to now there do not appear to be any published results on quadrotor airframe aerodynamics. This section shows the absolute rotor-off fuselage force coefficients and moments and presents a fit for a semi-empirical model for fuselage drag and downforce. The data is expressed as an equivalent flat plate area in m^2 (with CD = 1) and plotted for a +/-90 vehicle angle of attack range.

It is important to point out that results are solely based on basic force measurements and several limitations have to be considered:

- No breakdown of the drag is presented (the reader is referred to helicopter literature [2, 6] for a typical drag breakdown on SMR helicopters).

- The influence of the support strut, despite being measurable in other experiments on SMR helicopters is not corrected for.

- Rotor-fuselage interactions, which Leishman and Prouty [2, 6] put in the order of 5-7 % of the total drag for a typical SMR helicopter, are not included.

- Finally, the reader is reminded that results are for "unfaired" quadrotors which have, external wires, antennas and motors.

6.2.3.2 Discussion of results

Reynolds number effects which lead to a measureable increase in the drag coefficients were only observed between 5-10 m/s. Between 10-25 m/s Reynolds number effects on the drag coefficient fall within the noise of the force balance. Due to the lower experimental

uncertainty at higher speeds all drag data presented here is averaged from tunnel speeds from 10-25 m/s.

Figure 67 (a) and (b) shows the force coefficients as a function of to the vehicle angle of attack, where a negative angle indicates the nose down orientation needed for forward flight trim. The side-force is negligible, but the z-force causes a slight upwards force (-z) around 0 deg. The force coefficients in X_b and Z_b can be well represented by a sin/cosine drag model introduced in Chapter 3 and with parameters as listed in Table 8. A better appreciation of the forces can be made by considering earth axes (Figure 67 (c-d): Over the practical angle of attack range from -45 to 0 deg an increase in negative angle of attack increases CF_{xe} and increases the downwards force. In earth axes the difference between the two fuselages can be seen more clearly and the more streamlined Draganflyer experiences lower drag and downforce.

Figure 67 g-h) shows the absolute forces and moments extrapolated from the measured coefficients at 15 m/s airspeed. The axes were chosen to represent the total mass of a 1 kg baseline quadrotor and the approximate single rotor reaction torque of 0.05 Nm. Even at this speed, which is below the claimed top speed of current quadrotors, axial and normal forces can be significant compared to the vehicle weight. The moments were measured from the moment centre Z_{CP}, which was set to ensure zero pitching moment at 0 deg vehicle angle of attack. There is a nose down pitching moment around -30 deg which is probably caused by the vehicle downforce (Fz) acting a point ahead of the moment reference centre. This offset, however, appears small in absolute terms and the fuselage pitching moment is small compared to the rotor pitching moment discussed in Chapter 5 and is hence ignored for the semi-empirical drag model.

	Draganflyer	Aeroquad frame
kCFx	-0.01422	-0.01221
kCFz	-0.01903	-0.02923
Z_{CP} (from rotor plane) [m]	0.003	0.023

Table 8: Fuselage aerodynamic parameters and centre of pressure estimates.
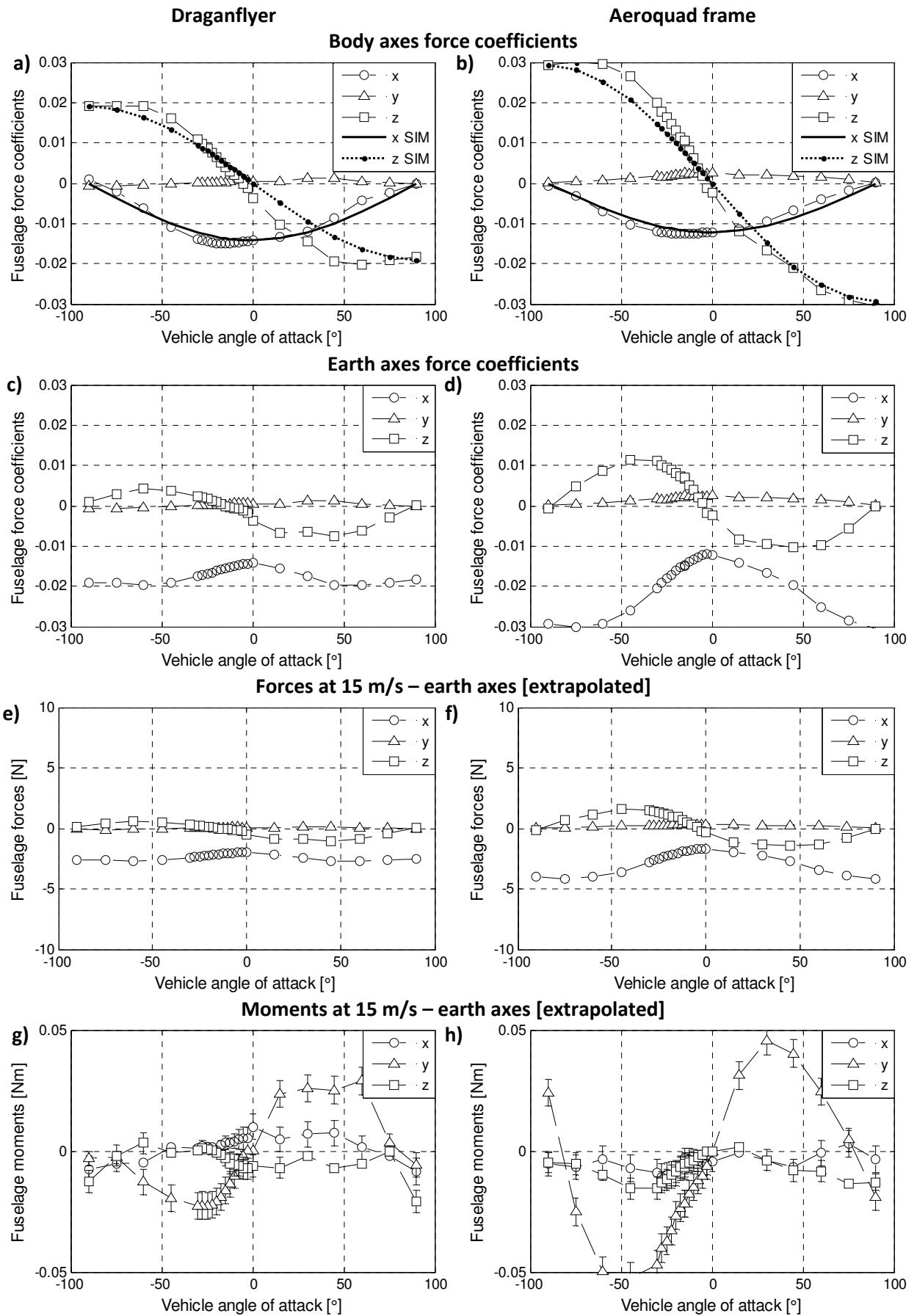
Figure 67: Experimental results for quadrotor fuselage aerodynamics.

6.2.4 Forward flight power and trim curves

In this section the trim-settings and power results for the fixed-pitch, variable-speed test-rig, as described in Chapter 4.2.5, are presented. Results are shown for one "x" and one "+" configuration at a rotor spacing of d/D = 1.1

The power curve shown for a plus configuration in Figure 68 a) resembles a typical helicopter power curve with a clear minimum power speed and a rapid power penalty for further increases in flight speed. For this particular test-rig the x configuration does not show such a clear minimum power, but this could be caused by the different drag on the test-rig in x and plus configuration and is not specific to all x-configurations as shown in (Figure 69). The increased drag on the x-configuration test-rig also affected the power demand, an effect that is not expected to be universal for all x-configurations.

To trim the vehicle in forward flight a large nose-down vehicle angle of attack is required to overcome the resultant force of body weight and drag (Figure 68 (c) and (d)). This large vehicle angle of attack puts the rotors in an operating condition that resembles a conventional helicopter in a steep forward flight climb. It can be seen that slightly larger vehicle angles of attack are required to trim this particular x-configuration which supports the hypothesis that the test-rig experiences higher body drag in the x-configuration.

Next attention is drawn to the trim rpm and breakdown of power between the individual rotors. In hover all rotors are equally loaded, but in forward flight there is a strong trend towards more heavily loaded rear rotors (#3 in +, #1-#2 in x configuration) and lightly loaded front rotors. This is driven by the need for a strong nose-down pitching moment to compensate for the nose-up pitching moment caused by the individual rotors (aerodynamic pitching moment + rotor hub force acting above the CG) and the fuselage drag force acting at a centre of pressure above the CG. The implication of this is that the maximum speed of a

quadrotor can be dictated by a saturation in pitch control authority which can happen significantly before the total installed power of the vehicle is reached.
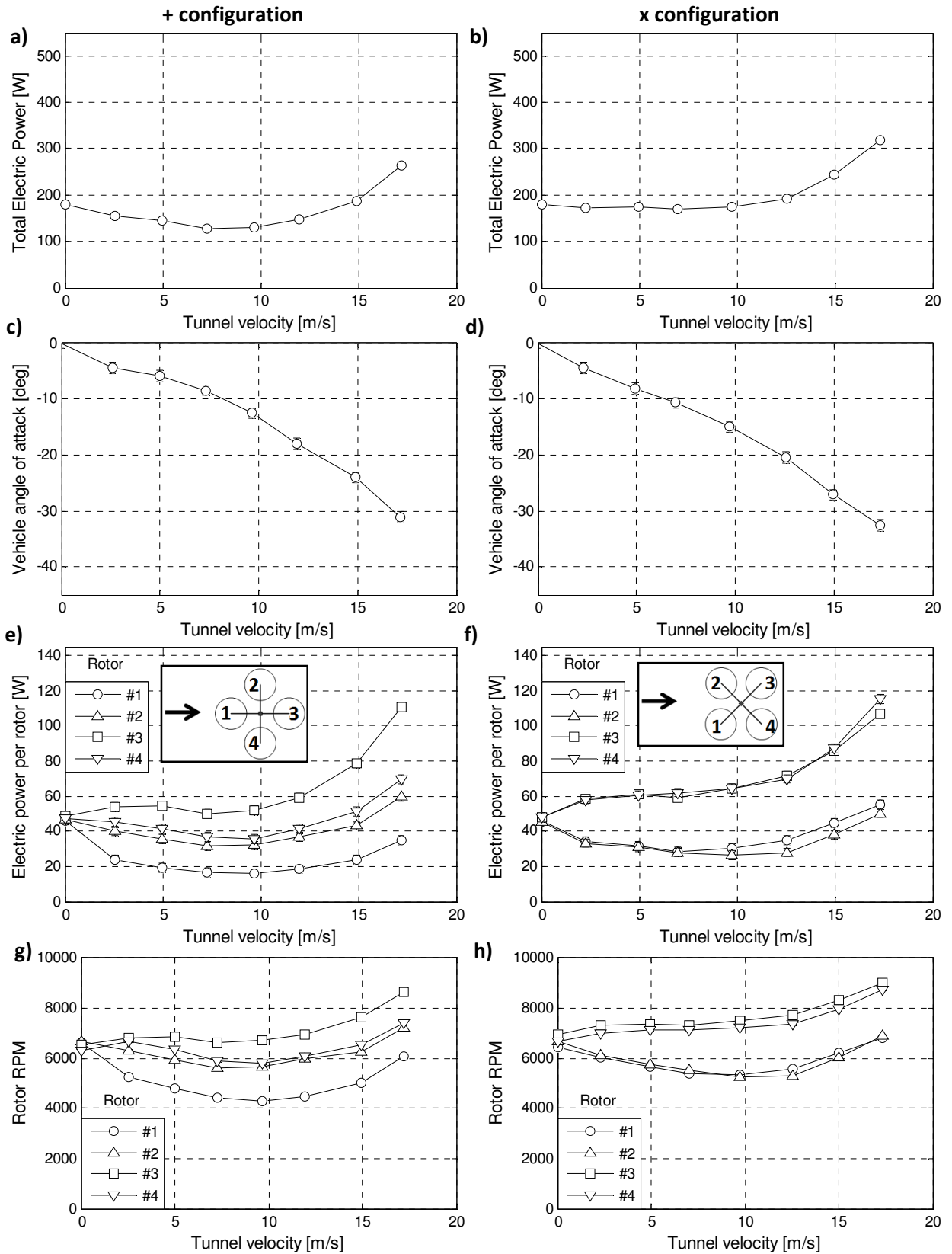
Figure 68: Experimental trim and power results for a quadrotor test-rig of d/D = 1.1.

If the difference in total power between this particular x and + configuration test-rig is compensated, it appears that an x-configuration would result in a reduced difference between front and rear rotor loading and could increase the velocity at which pitch control authority is exceeded. Basic trigonometry suggest that for a given maximum thrust, rotor-CG distance and body coordinate system, an x-configuration could increase the pitch and roll control authority by 41%. Based on this and experimental results it appears that an x-configuration is the favourable configuration for quadrotors in forward flight.

6.2.5 Energy saving operational procedures

Whilst the exploitation of maximum range and minimum power conditions is standard practice in commercial and military aviation, little attention has been paid to this aspect for quadrotors and other small rotorcraft UAVs envisaged for autonomous operations where literature typically only focuses on hover efficiency [34] or trajectory generation [4].

This section explores the potential of exploiting power efficient flight modes for the autonomous mission planning of quadrotors. Experimental data (see Figure 69) from an open source Aeroquad quadrotor was used to extract conditions for minimum power (A), maximum range (B) and maximum speed (D). Based on these results the theoretical endurance and range for a given amount of energy (2000 mAh 3-cell battery) is calculated in Table 9.
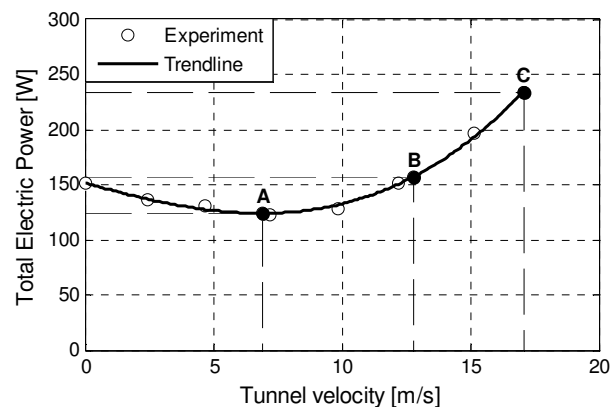
Figure 69: Power curve of an Aeroquad trimmed at 1 kg, based on wind tunnel experiments.

Condition	Hover	Min Power Speed	Max Range Speed	Max Speed
Velocity [m/s]	0	6.9	12.8	17.1
Power level flight [W]	151.6	124.0	157.3	232.9
Endurance [min]	8.8	10.7	8.5	5.7
Range [m]	-	4447	6503	5868

Table 9: Power conditions of an Aeroquad trimmed in the wind-tunnel (W=0.98kg), with a theoretical

2000 mAh battery operating at 11.1 V.

It can be seen that clear endurance and range improvements can be achieved by substituting hover with loiter at minimum power and cruising at maximum range speed as opposed to maximum speed. To illustrate this point a sample mission is defined in which a quadrotor has to travel 1 km, stay on station for as long as possible and then return to base. Two mission scenarios are considered:

- Scenario A: Vehicle cruises at V_{max} and uses hover to loiter at station.

- Scenario B: Vehicle travels at maximum range speed and uses minimum power speed to loiter at station.

	Travel time (return) [s]	Energy for transit [Wh]	Energy available for loiter [Wh]	Maximum loiter time [s]
Scenario A	117	7.6	14.6	347
Scenario B	156	6.8	15.4	446

Table 10: Benefits of exploiting minimum power and maximum range conditions on a sample mission.

It is shown that by using simple operational practices the time on station can be increased by about 30% if the penalty of reaching station (19.5 s or 33% one way) is considered acceptable. It hence appears promising considering power saving practices like these in the autonomous mission planning of quadrotor vehicles.

6.2.6 Conclusions on the performance of current quadrotors

From the material presented in the previous section the following conclusions on current quadrotors can be made:

- The power demand is heavily influenced by non-ideal aerodynamic losses and electric losses and the motor system has to be well matched to the expected loading conditions (in hover and beyond).

- Quadrotor rotor-rotor interference appears small, but suggests a similar trend as on tandem helicopters where the front rotor power is reduced and the rear rotor power is increased.

- Quadrotor fuselage aerodynamics can be have significant effects and add a downforce that further increases the power demands.

- The quadrotor power curve is similar to that of conventional helicopters, but shows a steep rise in power at high speeds.

- Large vehicle angles of attack are required to trim quadrotors (and other small rotorcraft) in forward flight.

- The maximum flight speed may in practice be determined by running out of pitch control authority due to the need to compensate for nose-up pitching moments rather than reaching the maximum installed power of the quadrotor.

- An x-configuration is favourable over a + configuration in that it increases pitch control authority and increases maximum flight speed for a given rotor-cg spacing.

- Like large conventional helicopters, quadrotors could greatly benefit from operational practices that exploit minimum power conditions.

6.3 Impact of density and battery discharge

6.3.1 Density effects

Quadrotors and other MAVs typically operate near the ground and hence, rather than using a classic helicopter performance analysis of considering an altitude-velocity flight envelope, solely the effect of density on the total electric power of a variable rotor speed quadrotor is considered.

Two test-cases were picked to represent the extremes of the operational envelope: A quadrotor operating at -20 C at sea level (ρ=1.32 kg/m^3) and a quadrotor operating 4km above sea level at a temperature of 40 C (ρ=0.71 kg/m^3). Both cases were simulated using the baseline simulation model introduced in Chapter 7.3 and compared against ISA SL conditions.

Two important effects have to be considered when analysing the results: The change in rotor power on a variable-speed rotor and the change in fuselage drag. For constant thrust demand, C_T and C_P the power demand varies according to $\frac{\rho}{\rho_{SL}}^{-0.5}$, because a lower density has to be compensated with a higher rpm. The implication of this is that a lower density results in an increase in rotor power. The opposite effect can be observed for the parasite power: a reduced density reduces drag, parasite power and the required vehicle trim angle of attack which leads to further reductions in induced/propulsive power.

Figure 70 shows the implication of these effects: In a low density environment the power demand at low speed is significantly increased whilst in the high speed regime over 15 m/s experiences considerable power savings compared to sea level. The higher density case behaves the opposite way and shows slight power savings for low and moderate flight speeds, whilst experiencing power penalties in high speed. The high density effects appear less pronounced because of the smaller relative change from sea level conditions (ρ=1.225 kg/m^3)

a)

b)
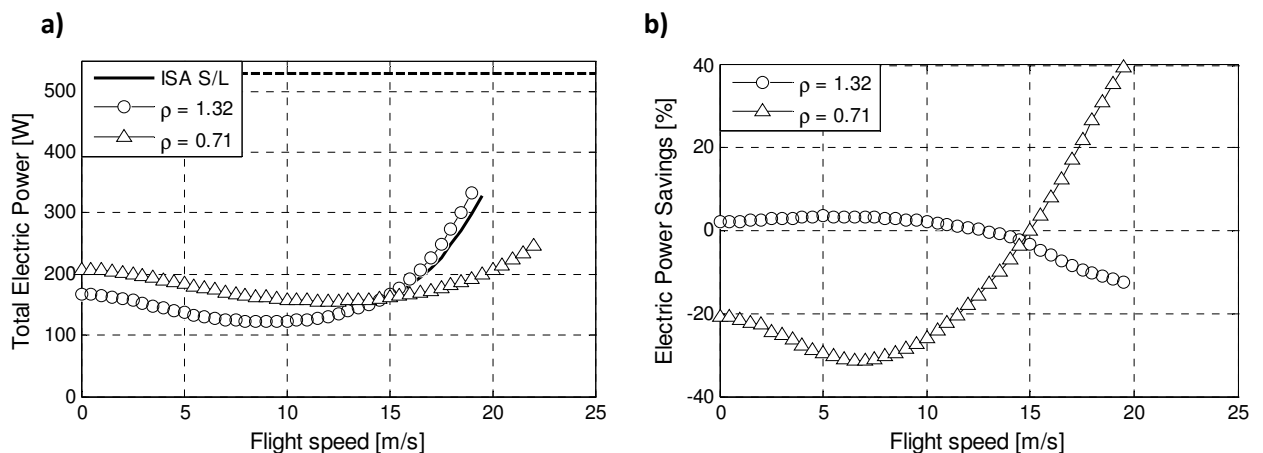

Figure 70: Effect of density on power curve (a), electric power savings compared to a vehicle operating at ISA S/L (b).

6.3.2 Effects of battery discharge

For electric vehicles the mass stays constant with flight-time, however the battery voltage drops. Since the MOSFETs in the motor ESCs are effectively current-limited a reduction in maximum voltage could theoretically restrict the maximum available battery power.

Figure 71 (a) shows the battery voltage against energy consumed for a typical configuration operating at the hover power level of the "Aeroquad" presented above. It can be seen that the battery voltage remains relatively constant over large parts of the curve and only drops significantly for the last 15% of its remaining capacity, a situation that would rarely occur in practice. Even at this level the voltage, and hence maximum available power, only drops by about 15% from its nominal value. Providing the battery is sized such that its maximum discharge rate is well above the maximum current demand, no significant effects on flight performance are expected.
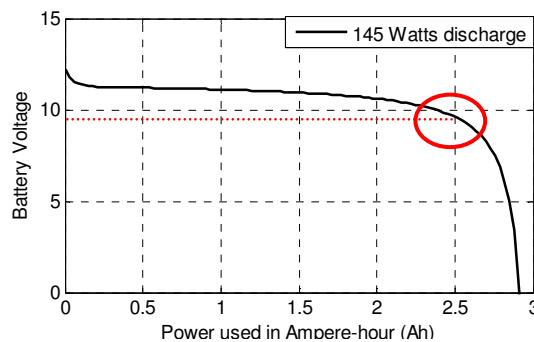
Figure 71: Battery discharge curve showing the voltage drop against the power discharged (based on Simulink battery model [60], 3 cell Lithium-Polymer battery with 3 Ah capacity).

6.4 Configuration design improvements for forward flight

6.4.1 Framework for design improvements

This section takes a structured approach to investigating configuration design choices that could improve the performance of quadrotors in terms of their endurance/range and increasing the maximum flight speed. The analysis is confined to the configuration design of the vehicle only, with rotor and blade design optimisation considered outside the scope of this

174

work (the reader is referred to prior work on this by Bohorquez [38]). Hence all cases are compared based on the same rotor design. The special case of introducing collective-pitch capabilities on quadrotors is discussed separately in Chapter 7.4

Based on the previous performance analysis of current quadrotors a systematic approach for improving performance is presented in Figure 72. The left hand branch investigates ways of improving forward flight power requirements and hence would also contribute towards increasing the maximum flight speed. The right hand branch investigates additional ways of increasing the maximum flight speed through equalising the loading between front and rear rotors and hence delaying the speed at which pitch control authority is lost.
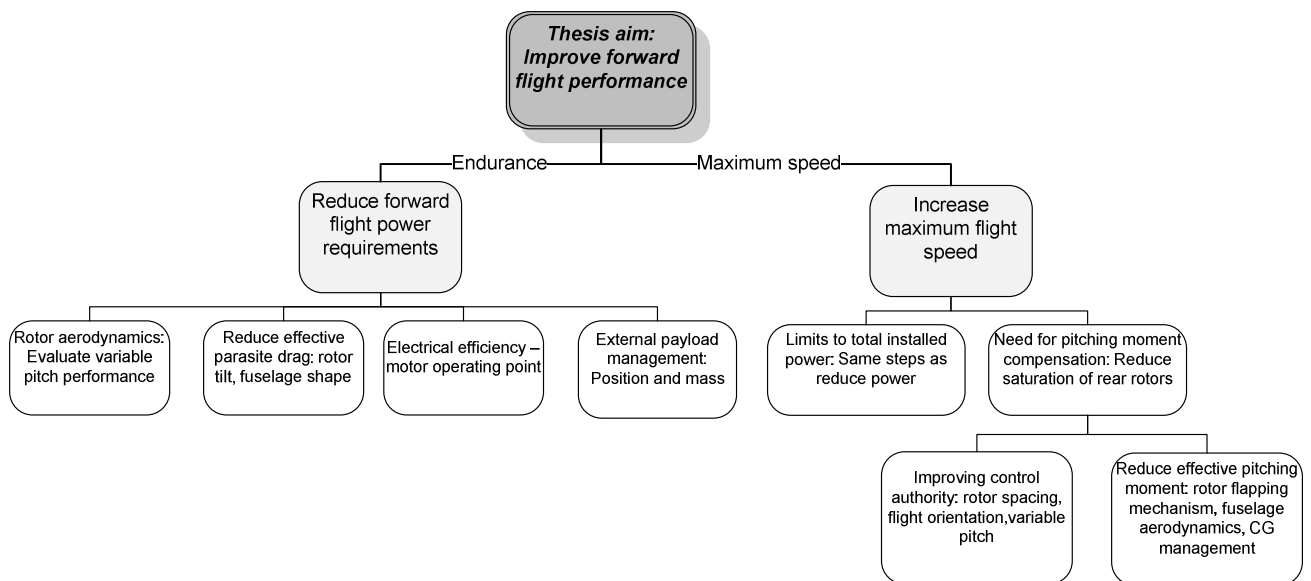
Figure 72: Systematic approach at improving quadrotor flight performance.

A baseline quadrotor as described in Table 11 is used as a starting point and benchmark for the study presented in Chapter 7.3 and 7.4. All simulations in Chapter 7.3 are based on a conventional fixed-pitch, variable-rpm rotor with the rotor collective pitch set at the point of highest hover efficiency.

175

Rotors	0.254 m diameter, untwisted, NACA0012, untapered from 0.4R to tip; hingeless flapping with a flapping frequency ratio as defined in Chapter 3.3.3; Same rotor as in variable pitch wind tunnel study
Configuration and rotor spacing	X-configuration with 0.2159 m rotor-centre spacing
Motor	Rimfire 22M-1000, same as used in tests, with updated motor parameters from Chapter 3
Battery	Hypothetical 3-cell lithium-polymer, 2000 mAh, V_{nom} = 11.1 V
Mass and CG	1 kg, CG at [0,0,0.03] CP at [0,0,0.003]
Drag model	Semi-empirical model for Draganflyer axial and normal forces with parameters as described in Table 8
Rotor aerodynamics model	Local differential blade element code with flapping parameters as identified in Chapter 3.3.3
Motor and battery models	1st order motor model [58], battery losses ignored
Atmospheric conditions	ISA S/L, no atmospheric wind

Table 11: Parameters of baseline quadrotor simulation case.

6.4.2 Reducing forward flight power requirements

6.4.2.1 Baseline model result: Breakdown of forward flight power requirements

The power curve for the baseline case (Figure 73 (a), Table 12) shows the same trend as the experimental power curves with a clear minimum power speed and maximum speed. This section discusses the performance limits of the baseline case which will then be used as benchmark for the effect of configuration design changes. It also provides further insight into the mechanisms limiting quadrotor flight speed beyond the ones discussed previously.

The power curves in Figure 73 show the total and individual motor power requirements and indicate the total installed power limits and the maximum power per motor. As with the previous cases a distinct difference in front/rear rotor loading can be observed, with the rear rotors operating at a significantly higher power. The highest speed at which a feasible trim solution could be achieved lies at 19.5 m/s – by inspection this is slightly lower than the single motor installed power limit. This is caused by a maximum rpm saturation of the rear rotors for the particular motor configuration.

	Hover	Minimum Power (A)	Maximum Range (B)	Maximum Speed (C)
Velocity [m/s]	0	9.38	13.74	19.50-20.0
Electric Power [W]	170.62	125.65	145.52	328.83-363.14

Table 12: Characteristics of the baseline vehicle power curve.
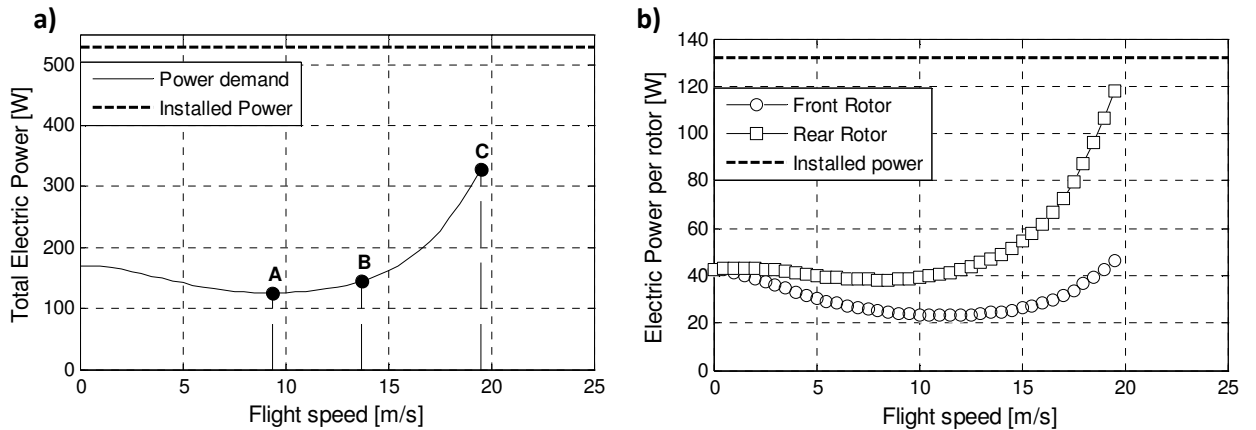
Figure 73: Power curves for baseline vehicle in x-configuration: a) total electric power, b) electric power per motor.

Next, attention is drawn to the large vehicle angle of attack required to trim the vehicle in high-speed forward flight (Figure 74 (a). The effect of this is twofold: First a large vehicle angle of attack increases the effective drag (see drag results in Figure 67) and hence leads to an increase in parasite power beyond the levels expected from the rise in airspeed alone. Secondly, the large vehicle angle of attack causes a significant rise in induced power (which includes the propulsive power) for a number of reasons:

- The downforce increases with negative angles of attack (As shown in Chapter 6.2.3).

- The total required thrust magnitude increases to compensate for the downforce and provide a sufficient Z_{earth} force for weight support. This also increases the induced velocity for a given flight condition.

- The effective vertical velocity through the rotor disk, Vz_disk, increases.

- Hence, as suggested by the basic momentum theory induced power relationship Pi = T*(vi+Vz), the induced power increases significantly.

The trend of the induced power can be clearly observed in Figure 74, which also shows the total mechanical power and parasite power. It can be seen that the rapid rise in mechanical power is driven by the combination of rising induced/propulsive and parasite power.

a)

b)
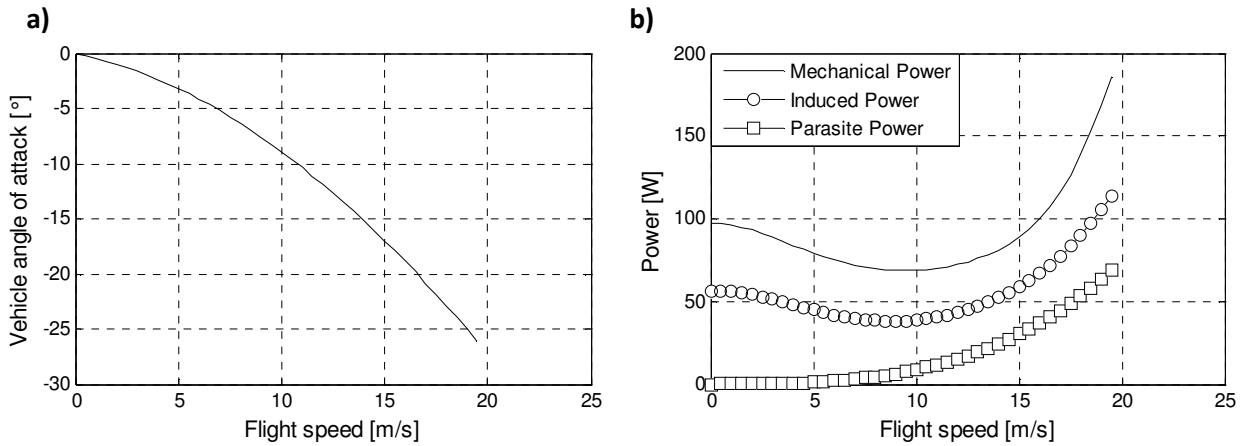
Figure 74: Baseline vehicle trim curve (a) and power breakdown (b)

6.4.2.2 Effect of mass and external payloads

In this section the effect of payload on vehicle is analysed by considering added mass and the effects of parasite drag from external payloads.

First, changes in the take-off weight are considered without any changes to cg and drag – all simulations are run on the baseline vehicle. The power and trim vehicle angle of attack curves for a range of take-off weights are shown in Figure 75. These results imply that low speed regions are mass-driven whilst high-speed regions are dominated by drag. For hover and low speed, an increase in mass results, as expected, in a power increase of about $\left(W/W_0\right)^{1.5}$ and this effect can be slightly amplified by changes in motor efficiency at higher loading. For higher speeds the impact of the additional mass reduces and the power benefit of the low mass cases diminishes to zero. This can be explained by the lower drag/weight ratio which causes a reduction in the vehicle angle of attack (Figure 75 (b) and hence significantly reduces power requirements through the mechanisms discussed in Chapter 7.3.2.1 above.
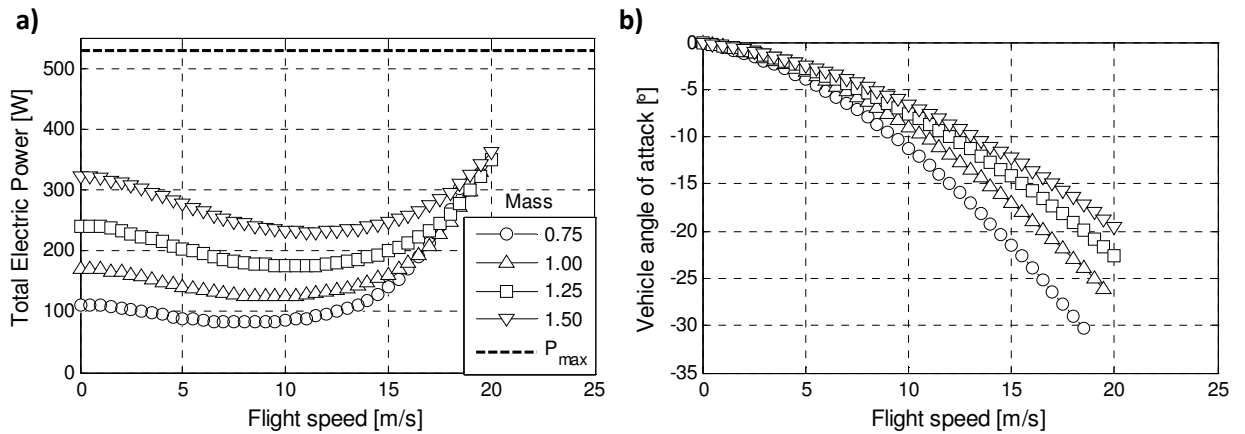
Figure 75: Effect of vehicle mass [kg] on the total electric power (a) and vehicle angle of attack (b).

Next the results for a quadrotor with external payloads are analysed – this case is particularly relevant to current quadrotors which normally carry payloads, like cameras, externally. For this study two different payload weights (0.25 kg and 0.5 kg) are tested using two different payload drag areas (0.01 m^2 and 0.04 m^2). For all four combinations the payload was assumed to be underneath the vehicle at a payload CG and CP of [0,0,0.1] causing a downwards shift of the total vehicle CG and CP.

The power results in Figure 76 (a) confirm once again that low speed regions are mass driven, whereas the high-speed region is drag driven: It can be clearly seen that at low speeds the same take-off masses behave similarly and independently of the body drag, whilst at high speeds the opposite is the case and same drag results behave similarly. This is also reflected in the parasite power (lower for low drag) and the vehicle angle of attack (lower for low drag, high mass cases). When compared to the baseline case the maximum flight speed is significantly reduced with increasing payload drag and minimum power and maximum range speeds are also shifted to lower speeds.

Next, attention is drawn to the ratio of front/rear rotor loading (Figure 76 (d) which shows that the nose-down pitching moment caused by payload drag acting underneath the rotor plane can reduce the loading imbalance and hence delay the loss in pitch control authority.
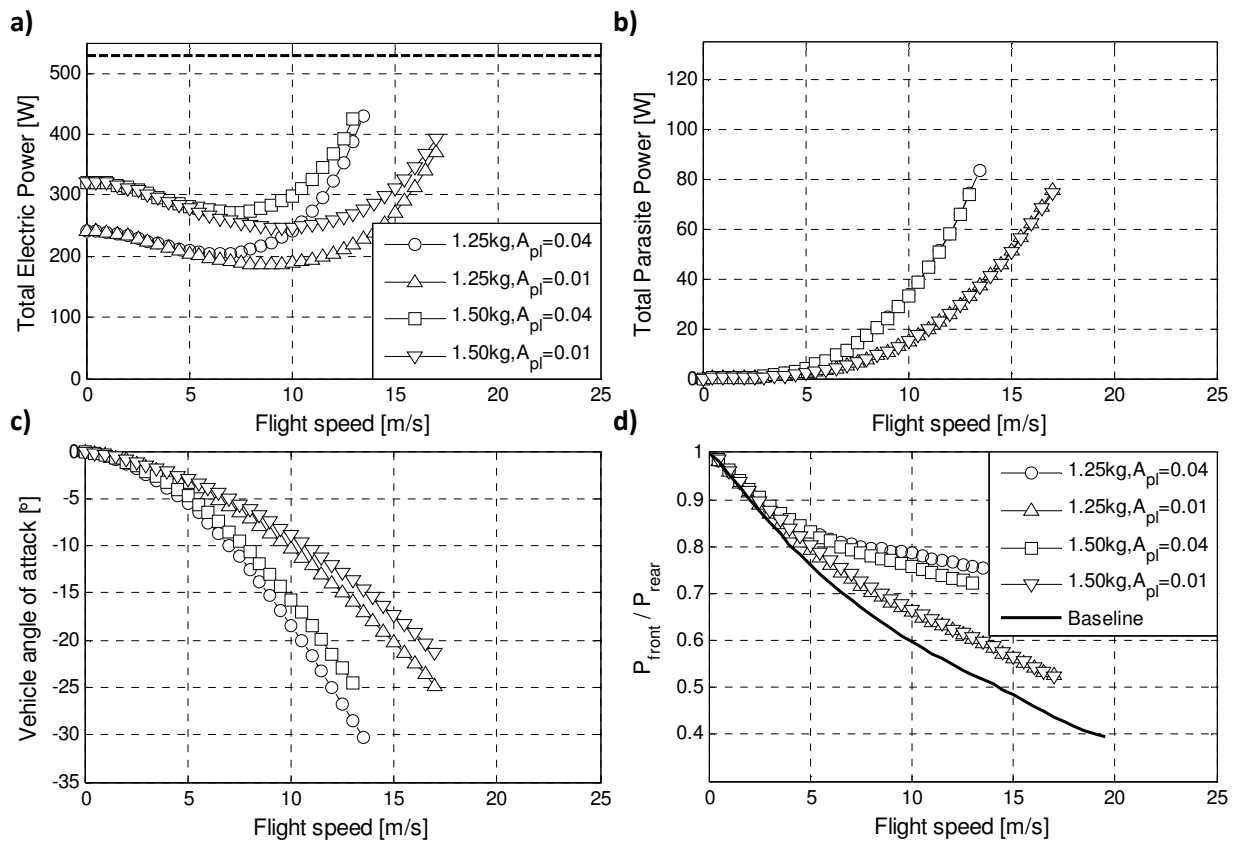
Figure 76: Effect of an external payload on power and trim values

The implications of this section are that quadrotor designers have to carefully balance mass and drag penalties of external payloads to minimise performance losses in the preferred flight regime. For external payloads at high speeds payload drag reduction should receive special consideration.

6.4.2.3 Rotor orientation and fuselage aerodynamics

As discussed previously the high-speed performance is drag driven and, like in many aerospace applications, it is evident that drag reduction could lead to performance improvements. Whilst one of the most obvious solutions could be aerodynamic shaping of the fuselage, there are practical limits to this and the details of fuselage-optimisation outside the scope of this thesis. Instead, attention is focused on reducing the net effect of fuselage aerodynamics at typical operating conditions through introducing a tilt angle between the rotor-shafts and the fuselage body axes (see Figure 77].
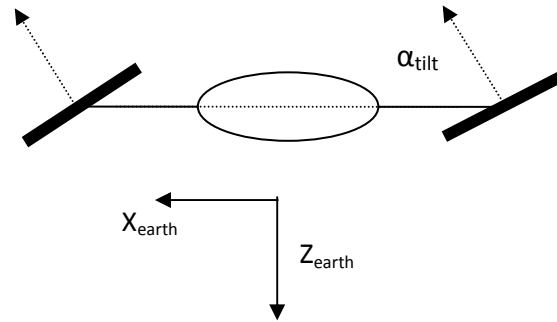
Figure 77: Sketch of the rotor-fuselage tilt angle.

The previous analysis of quadrotor performance revealed that large vehicle angles of attack are required for high speed trim. At the same time the measured fuselage force coefficients are strongly influenced by the vehicle angle of attack as shown in Figure 78 (based on experimental data earlier in this chapter) where the reference lines and arrows indicate the potential reduction in fuselage forces through a fuselage-rotor tilt angle of 20 deg and 30 deg. Particularly significant reductions can be achieved in the fuselage downforce (F_{z_earth}).
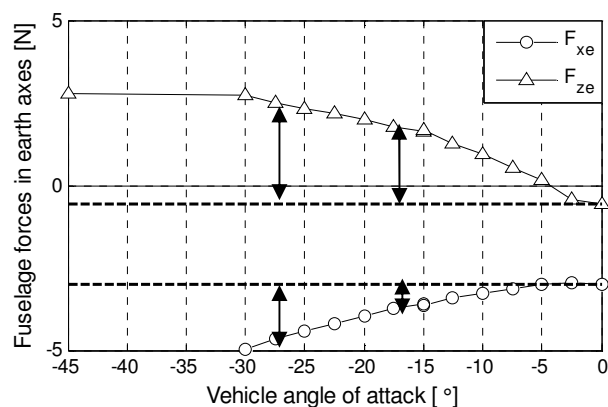
Figure 78: Effect of fuselage tilt on aeroquad fuselage forces at 20 m/s.

Three different fuselage tilt angles (10, 20, 30deg) were studied for the baseline case (Draganflyer fuselage) and the Aeroquad fuselage model. Results for level flight power, power savings and vehicle angle of attack are shown in Figure 79.

At first glance the difference in power in Figure 79 (a) and (b) seems to be small, but a closer inspection of the power savings (Figure 79 (c) and (d)) reveals significant power savings at high speed, in particular for the Aeroquad frame where power savings of almost 20% could

be achieved with a 20 deg tilt angle. Whilst power-savings are most pronounced in the high-speed region there are power savings throughout the velocity envelope. Effects on the Aeroquad fuselage are more pronounced, because this model has the higher total drag and a ratio of vertical to horizontal drag coefficients which make aerodynamic forces more sensitive to the changes in vehicle angle of attack.

In line with the reduction in forward flight power the maximum flight speed can be increased by introducing a tilt angle and results indicate an increase of about 10% for the Aeroquad fuselage model and 5% for the baseline fuselage model.

An interesting observation for both fuselage models is the relationship between power savings and fuselage tilt angles: a large proportion of the power savings can be realised with a moderate tilt angle of 10 deg and maximum savings were found for 20 deg tilt which is in the order of magnitude of vehicle angle of attack in the high-speed region. Increasing tilt beyond the vehicle angle of attack (30 deg tilt) does not yield additional high-speed power benefits.

Introducing a fuselage tilt-angle can be a simple and effective method for increasing maximum flight speed and minimising power for a given fuselage, proving design challenges such as landing gear arrangement and rotor clearance can be tackled. For those fuselage models tested the best power savings could be obtained if the tilt angle is matched to the high-speed vehicle angle of attack. For future airframes a design approach should to be taken that minimises drag and downforce at the actual vehicle angle of attack in high-speed flight, rather than being optimised for 0 deg as indicated by Figure 67.
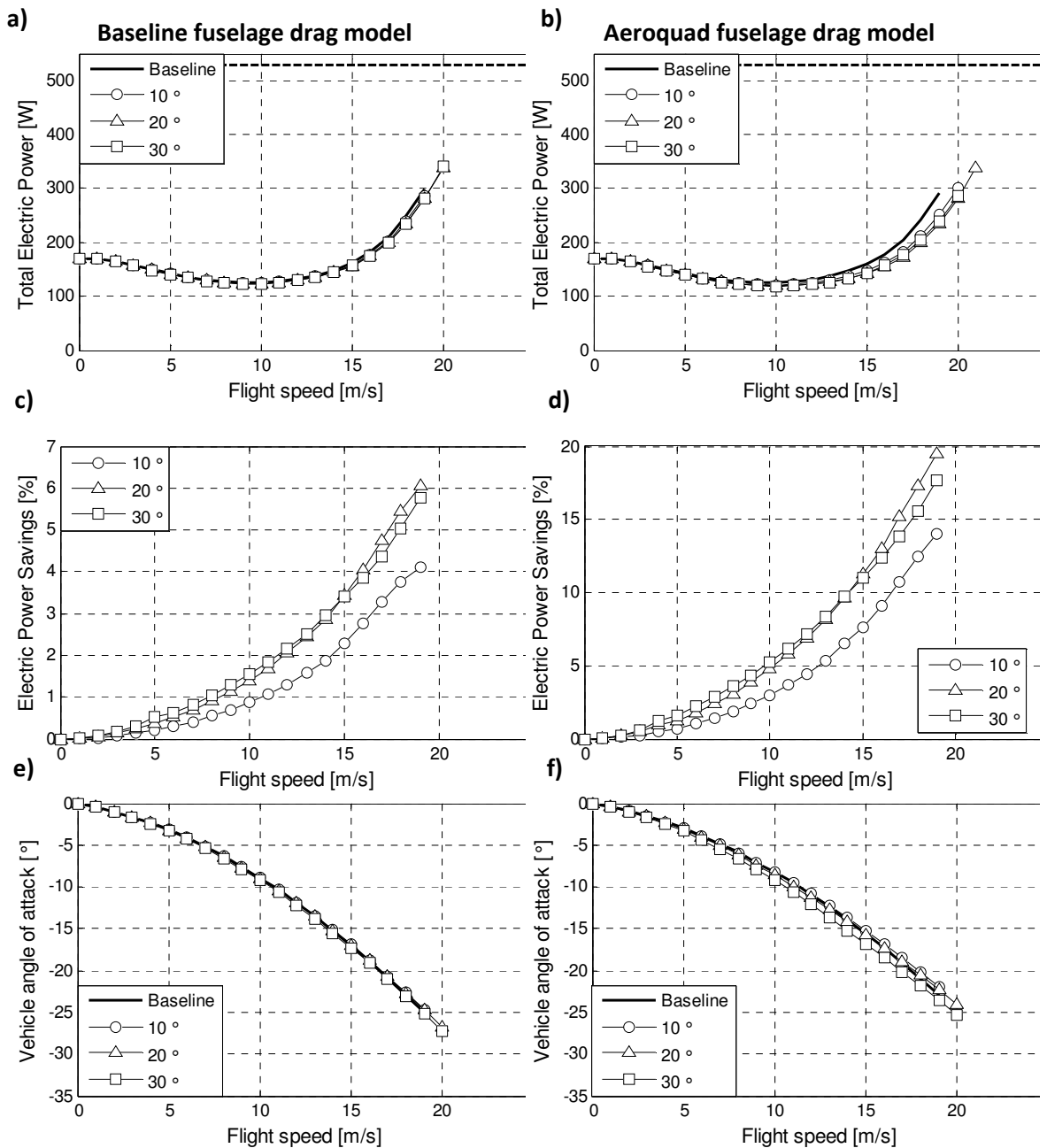
Figure 79: Effect of a fuselage tilt angle on power and trim conditions.

6.4.3 Equalising rotor loading – increasing maximum flight speed

6.4.3.1 Rotor spacing

It has been shown previously that an x-configuration can be advantageous, because it maximises control authority for a given rotor spacing. Based on the x-configuration, it is now investigated how a change in rotor-spacing could affect the maximum flight speed. Two cases are shown: an increase in spacing by 25 % (d/D = 1.5) and 50 % (d/D = 1.8). The expected

effects are a more equal rotor loading, increased maximum speed and reduced forward flight power.

Figure 80 (a) shows that power savings against the baseline case are very small (up to 1% - 1.7%). A balanced design decision would have to consider the increase in fuselage mass and drag due to the increased rotor spacing and it is unlikely that increased rotor spacing could yield significant net power savings.

Next, the ratio of rear rotors to total power is analysed. The importance of this is that a lower rear rotor power contribution delays pitching moment saturation and increases maximum speed. Figure 80 (b) shows that the effects are moderate: a 50% increase in spacing reduces the rear rotor loading from about 71% to 65% and can increase maximum speed in the order of 2-3%.

Given the added mass and drag expected from increased rotor spacing it seems unlikely that increased rotor spacing could result in significant net performance improvements.

Figure 80: Effect of rotor spacing on power and rear rotor loading.

6.4.3.2 CG and CP management

The previous discussions identified a series of sources for the pitching moment, mainly the rotor pitching moment due to flapping and the pitching moments induced from the rotor drag and fuselage drag acting away from the CG. In this section, the question of whether the
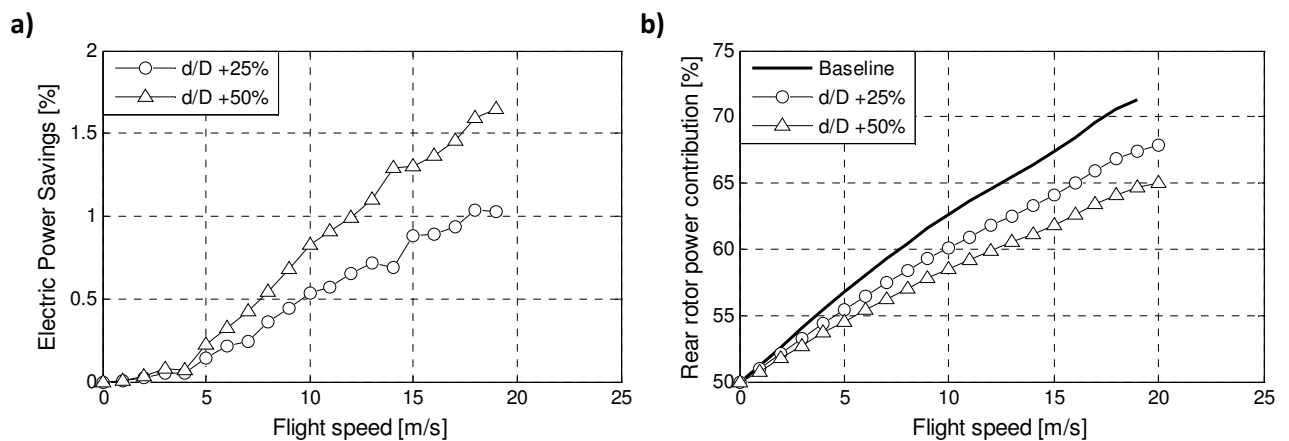
pitching moment correction in high speed flight could be reduced through vertical CG management is addressed.

Figure 81 (a) shows the key forces/moments contributing to the pitching moments on the baseline vehicle. A breakdown of the moments can be found in Figure 81 (b). For this configuration the rotor pitching moment due to the flapping restraint appears dominant, whilst the other moments are small because of the short moment arms between fuselage centre of pressure (see Chapter 6.2.3) and CG, and rotor hub and CG. Because the CG is located below the fuselage CP and the rotor plane (z_{cg} = 0.03m), drag forces result in an additional nose-up pitching moment.
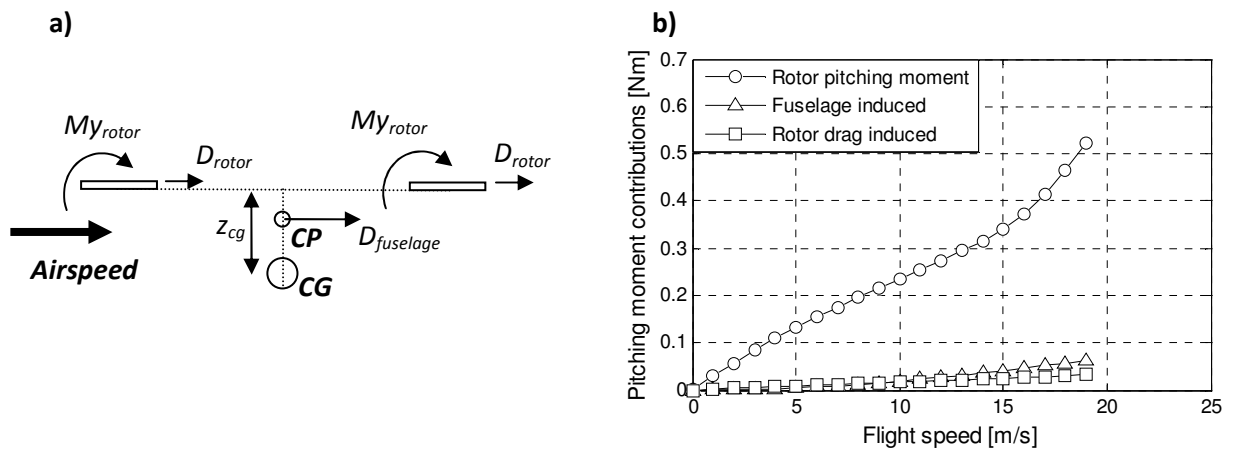
Figure 81: Analysis of pitching moment contributions on the baseline model.

A CG above the rotor plane and the fuselage CP would result in a nose-down pitching moment to counteract the rotor pitching moment. Two theoretical scenarios are considered: A CG 12 cm (z_cg = -0.12 m) above the rotor plane which was selected to largely cancel out the high-speed pitching moments, and a medium CG 6 cm above the rotor plane (z_cg = -0.06 m).

Figure 82 shows that the total electric power savings are relatively small (about 3%), but that a significant reduction in rear-rotor loading can be realised and maximum flight speed can be increased by up to 10%. Whilst, a high CG might not always be practical for vehicles carrying an external payload underneath the fuselage, these performance benefits justify

investigating design alternatives such as a rotor-down design presented by Pounds. As a general rule designers should aim at matching the fuselage induced pitching moments to cancel rotor pitching moments over the desired high-speed range. Lifting surfaces could make a contribution to this, but are not further discussed within this thesis.

a)   **b)**
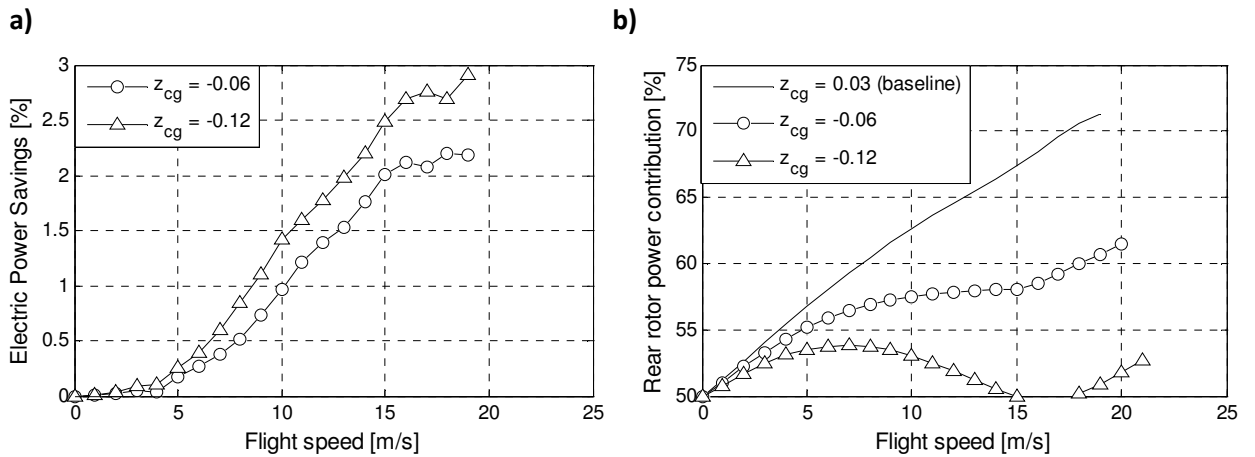
Figure 82: Effects of a high CG on electric power savings and the rear rotor loading ratio.

6.4.3.3 Flapping hinge design

Whilst the previous sections discussed methods for mitigating the effects of the nose-up pitching moment, this section takes a different approach and explores ways of reducing the nose-up pitching moment through modifications of the flapping mechanism.

In Chapter 6, the aerodynamics of a single hingeless quadrotor rotor were discussed and the hingeless rotor flapping was identified as the main source of the rotor pitching moment. The magnitude of the pitching moment depends on the flapping angle and the equivalent flapping spring stiffness which is coupled to the reduced frequency ratio λ_β (1.35 for the baseline case).

Two different cases are studied in this section: A reduced-stiffness rotor with a flapping frequency ratio of 1.05, which is not untypical for conventional helicopters, and a teetering rotor with $\lambda_\beta = 1$. Whilst quadrotors typically use hingeless rotors for mechanical simplicity, a teetering rotor assembly could also be mechanically simple and would not allow flapping

moments to be transferred to the hub. For examples of the use of teetering rotors on quadrotors see [14].

As shown in Figure 84 (b) a reduction in λ_β appears highly effective at reducing the loading imbalance between front and rear rotors and improves the maximum flight speed in the order of 10%. Furthermore significant electric power savings (Figure 84 a) can be realised because of the reduced rear rotor loading. This solution is, however, strongly affected by the change in tip-path-plane predicted by the model and it remains to be seen if such power benefits can be realised in practice.

No significant mass penalties are expected for the introduction of teetering hinges that could outweigh the power benefits, so that net performance benefits in high-speed operations are expected. A simple retrofit for small quadrotors could be the use of prop-savers (see Figure 83 (b), as used in model aircraft, to reduce the flapping frequency ratio and hence the transmission of moments to the rotor hub.

a)   b)
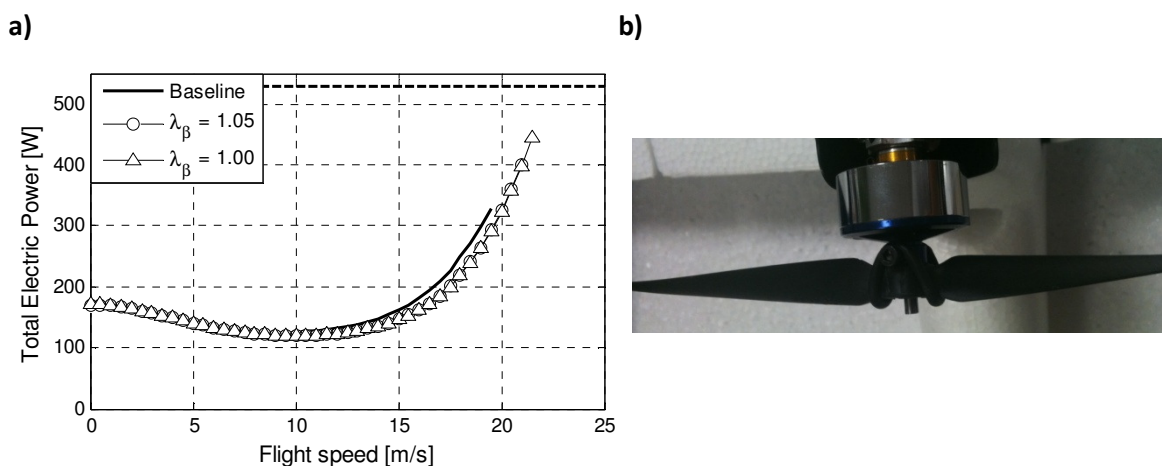
Figure 83: Power curves for various values of λ_β (a); a model aircraft propsaver uses an elastic band and could reduce the moments transferred to the hub (b).
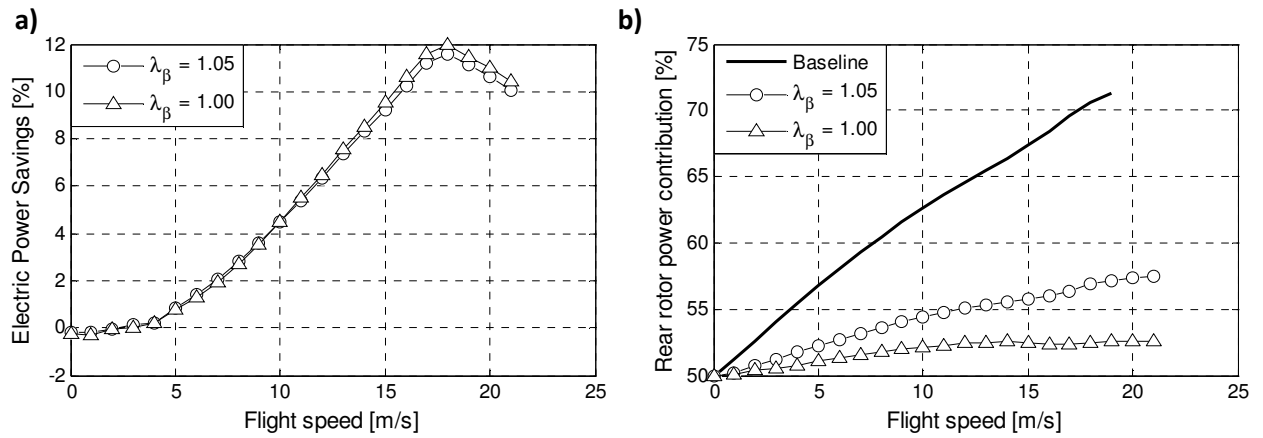
Figure 84: Effect of λ$_\beta$ changes on total electric power and rear rotor loading.

6.4.4 Summary of configuration design recommendations

- Power demand is mass-driven for low-speed flight and drag-driven for high speed flight. This has to be considered when matching payloads and batteries to the mission requirements.

- The drag on external payloads can severely reduce performance at high speeds and payload drag has to be reduced, even if this comes with a mass-penalty.

- Fuselage design needs to focus on minimising drag and downforce at typical high-speed vehicle angles of attack rather than in flight with a horizontal body attitude; For conventional quadrotors, a tilt angle between the rotors and fuselage is very effective in reducing power demands.

- Increasing rotor spacing appears ineffective for yielding net performance benefits.

- The maximum flight speed can be moderately increased through a high CG and more significant performance benefits might be realised from a reduction in flapping frequency ratio and equivalent spring stiffness, although large simulation uncertainty remains on this subject.

6.5 Performance of collective pitch quadrotors

6.5.1 Background and framework

With very few exceptions [31, 33] virtually all current quadrotors use fixed-pitch, variable-speed rotors for control. This section presents a case-study to identify the system level benefits of introducing collective pitch capabilities on quadrotors. The starting point for the case-study was the baseline model introduced in Chapter 6.4.1 and the most efficient hover conditions for pitch/rpm as identified in Chapter 6.2.1.

Beyond the obvious advantages of collective pitch quadrotors, such as increasing control authority, increased control bandwidth, manoeuvrability and scalability to larger vehicles [73], there might be additional benefits for the forward flight performance which are investigated in Chapter 6.5.2. A case-study is presented which shows the theoretical power and maximum speed benefits of a variable-pitch/fixed-rpm and a variable-pitch/variable-rpm scenario against the baseline vehicles.

However, there are drawbacks associated with introducing collective pitch, mainly an increase in complexity and mass. Changes to complexity are difficult to quantify, but it could be argued that the system complexity of a variable-pitch quadrotor would lie in between that of a conventional variable-speed quadrotor and a conventional SMR helicopter [31]. To allow for a balanced analysis, a mass penalty of up to 5% was estimated based on current technology EVP.

6.5.2 Theoretical improvements of forward flight performance

Two cases of using collective pitch are studied: A variable-pitch/fixed-speed approach and a variable-pitch/variable-speed approach. For the latter, a minimum total electric power optimisation was used to find the most efficient pitch/rpm condition for every flight speed. To reduce the degrees of freedom, the analysis is first presented for a global collective pitch angle (same front/rear rotor collective) whilst differential front/rear rotor rpm is used for trim. Later on it is investigated, if there are benefits in differential front rear/rotor collective and rpm settings.

Figure 85 shows the power curves for both variable-pitch methods and the power savings compared to the baseline scenario. Whilst both methods reduce the forward flight power demand at high speeds and can lead to moderate increases in maximum flight speed (about 5%), there is a pronounced difference in their effect on power at moderate and medium flight speeds.

For the variable-pitch/fixed-rpm method the power-demand is increased over large parts of the velocity range. This is, because the rpm is fixed to its most efficient hover value and the rotors do not operate at their most efficient pitch/rpm operating conditions at any airspeed beyond hover. The reasons for the most efficient single rotor operations are governed by aerodynamic effects, as discussed in Chapter 5, and electric motor effects, as introduced in Chapter 6. Furthermore, a large collective pitch increases the angle of the TPP and requires a larger vehicle angle of attack for trim which further increases power demands. Whilst the rpm could be fixed at an optimum value for any particular flight speed, this would automatically result in an increased power demand for hover and any condition other than the design point.

The variable-pitch/variable-speed method, on the other hand, has neutral/beneficial effects on power at all flight speeds and results in significant power savings at high speed flight

from 80-100% of the maximum speed. This suggests that both, collective and rpm, must be varied for collective pitch quadrotors to have power benefits over conventional fixed-pitch/variable-speed quadrotors over the full velocity range.
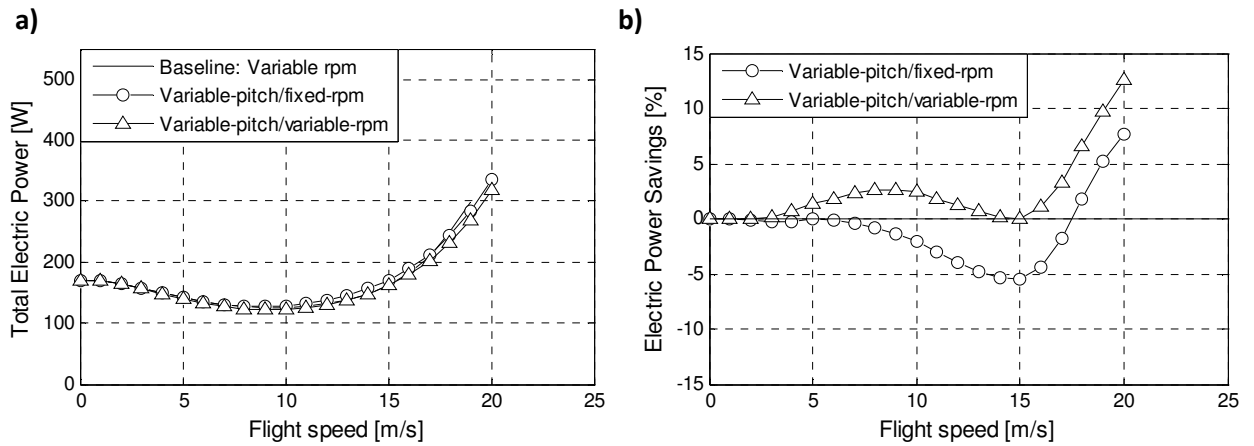
Figure 85: Effect of variable-pitch and variable-pitch/variable-rpm on power and power savings compared to the conventional fixed-pitch/variable-speed baseline case.

Next, attention is drawn to the differences in the pitch/rpm trim curves between a variable-pitch/fixed rpm (Figure 86 (a)), a fixed-pitch/variable rpm (Figure 86 (b)) and a variable-pitch/variable-rpm case (Figure 87). The first two cases share a similar trend that is coupled to the power curve, with both trim values rising at high speed. Because thrust behaves approximately linearly with pitch, whereas it is proportional to the square root of the rotational speed, more pronounced changes in the collective pitch are required for trim. If both, collective pitch and rpm, are changed (Figure 87) rpm variation and maximum rpm are significantly reduced compared to the fixed-pitch case (Figure 86 (b). This contributes towards aerodynamic power savings as well as electric power savings, because the rpm can be kept closer to the optimum efficiency conditions of the electric motors as discussed in Chapter 6.2.1.

a)

b)
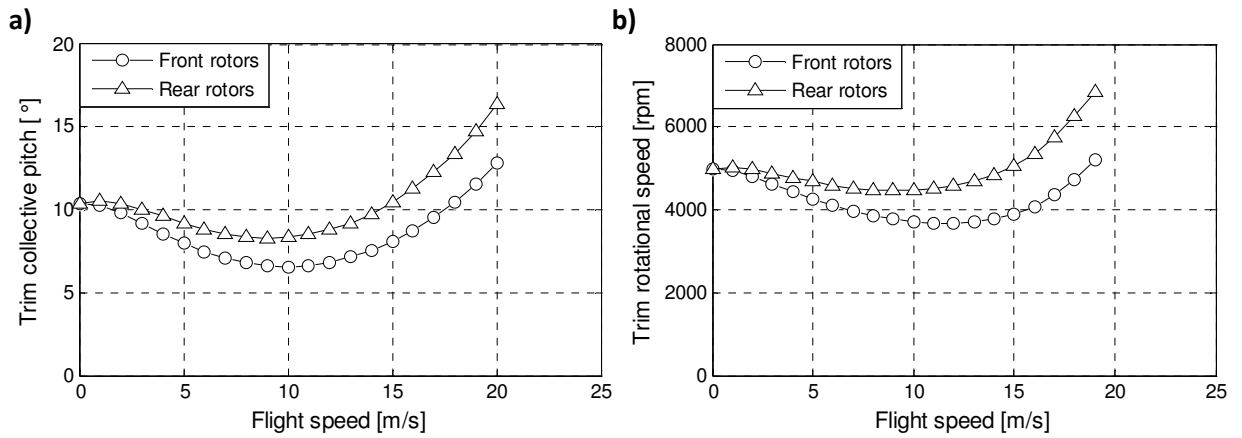
Figure 86: Trim curves for a variable-pitch/fixed-rpm (a) and a fixed-pitch/variable-rpm (b) configuration.

a)

b)
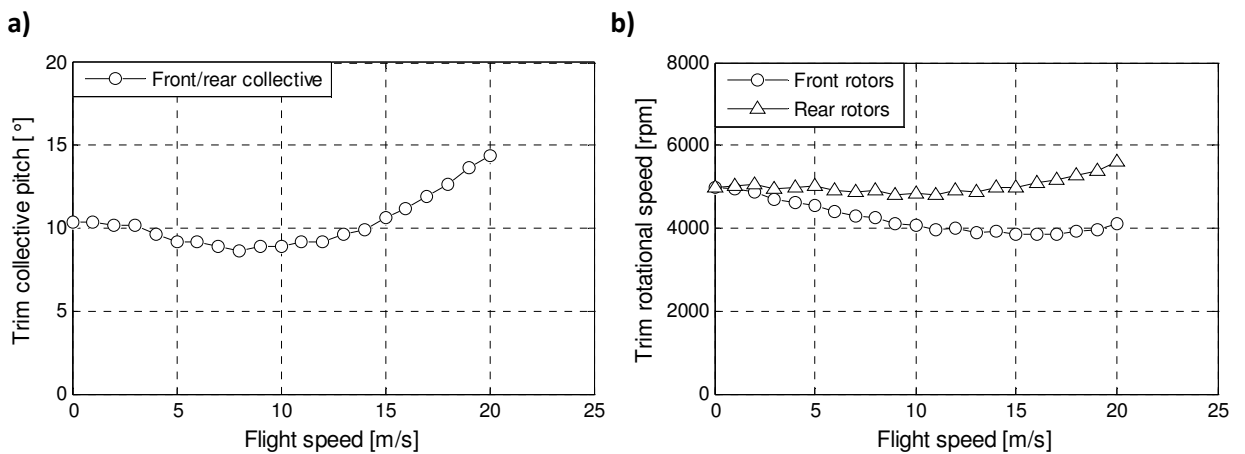
Figure 87: Global collective pitch (a) and front/rear rpm (b) for minimum power variable-pitch/variable-rpm

trim.

Next, the effects of a differential front/rear collective pitch and rpm are presented. Figure 88 shows the minimum power collective pitch settings for the combined front/rear collective as well as the ideal values for front and rear rotor collective. Because the rear rotor has the highest power demand in high-speed flight the combined collective almost coincides with the ideal rear-rotor solution, whilst the ideal collective for the front rotor is slightly increased. A look at the power savings compared to the fixed-pitch baseline case shows that there the difference between the "total electric power" savings, for a combined front/rear collective, and the savings that could be achieved with "differential front/rear collective" is small and additional power savings are negligible.
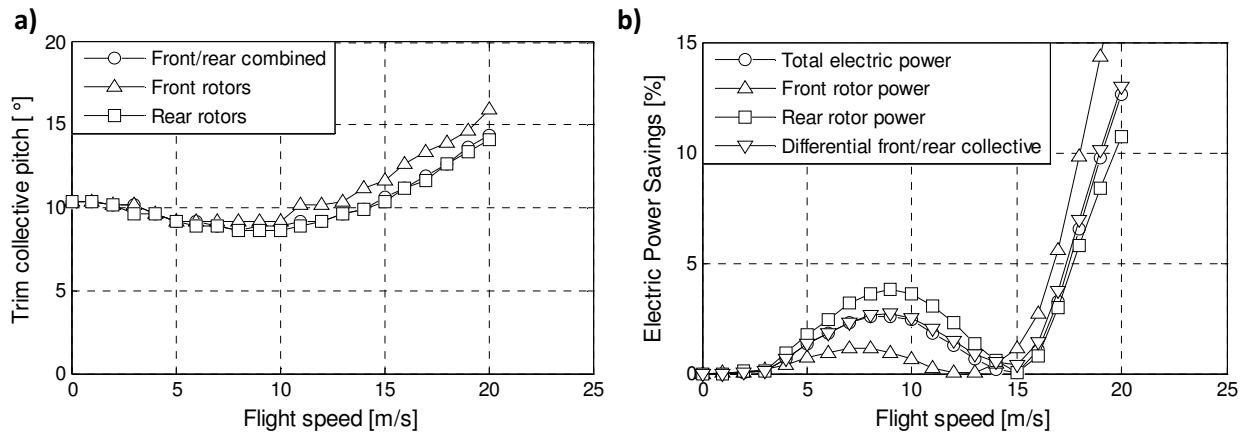
Figure 88: Ideal collective (a) and electric power savings (b) for different scenarios: a global front/rear

combined collective and differential collective on the front and rear rotors.

6.5.3 Limitations and balanced performance analysis

The introduction of collective pitch on quadrotors brings drawbacks in complexity, hub drag and mass. Whilst the first two are difficult to quantify without extensive statistical data and detailed design information, a first-order estimate of the effect of the mass penalty is presented here.

The mass penalty is highly design specific and mainly depends on added mass from the pitch actuation mechanism, the actuators themselves and their support structure. For a 1 kg prototype vehicle created as part of this research, the mass penalty is about 8 g per actuator and several grams for the rotor hub, which presents an overall mass penalty in the order of about 5% if currently available low-cost, commercial off-the-shelf components are used. Future optimised designs could have a smaller penalty and might exploit the reduced high-speed power demand to reduce the installed motor mass, hence a 5% mass penalty was considered a conservative estimate.

Figure 89 shows the effect of a mass penalty on the global collective pitch and the electric power savings compared to the fixed-pitch baseline design. Added mass has little effect on the collective setting, because the rpm is adjusted for most energy-efficient operation. However, the added mass results in a significant power penalty compared to the fixed-pitch baseline.

193

The power demand is increased from hover up to medium flight speeds and savings can only be realised for speeds close to the maximum flight speed at 80% of the maximum speed. Power savings at maximum flight speed remain significant and effects of mass on the maximum flight speed are very small.
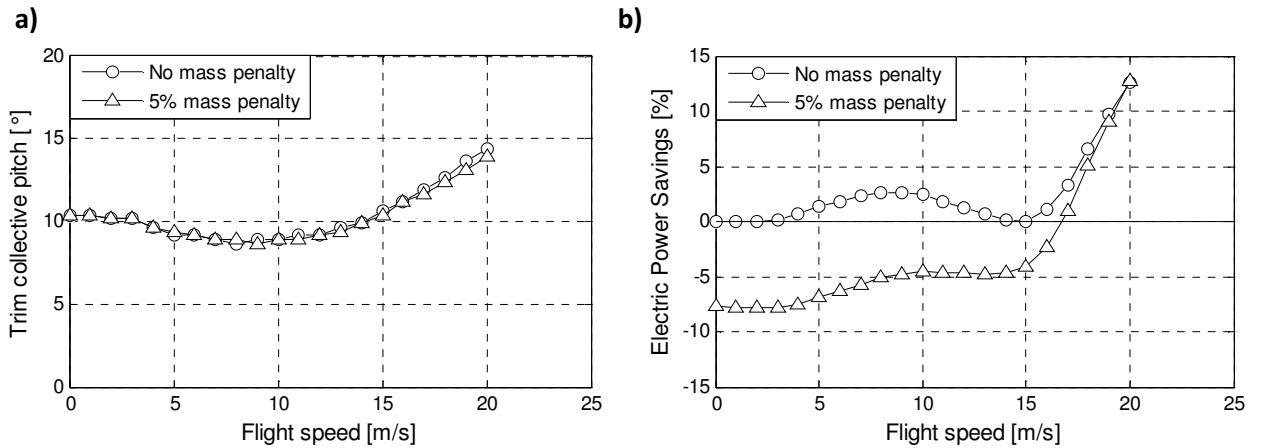
Figure 89: Effect of mass penalty on a variable-pitch/variable-rpm quadrotor global collective trim (a) and

power savings (b).

6.5.4 Summary of collective pitch effects on flight performance

- Introducing collective pitch capabilities brings theoretical improvements in maximum flight speed and reduces power demand for most of the flight envelope, especially at high speed.

- The full benefits can only be realised if both, global collective and individual rotor rpm, are varied in flight.

- There is little power benefit in differentially varying front/rear rotor collective pitch and rpm.

- The mass penalties associated with introducing collective pitch cause a power penalty in hover. There is, however, a power benefit above 80% of the top-speed.

Chapter 7: Conclusions

The aim of this thesis as defined in Chapter 1 is:

> *To develop improved understanding of the effects of configuration choice on the forward flight performance of quadrotors, in particular on endurance and maximum flight speed, through the development of low order vehicle simulation models and the use of wind tunnel experiments.*

7.1 Review of Contributions

This thesis provides four key contributions as described in Chapter 1: 1. It presents low-order simulation methods and experimental methods suitable for the study of quadrotor forward flight performance; 2. It presents unique experimental datasets useful for further research on the aerodynamics of small, hingeless rotors and further studies of quadrotor dynamics and performance; 3. It analyses the performance of current quadrotors, establishes the limits to their flight performance and analyses the effects of configuration design on the forward flight performance; 4. It evaluates the introduction of variable pitch rotors on quadrotor vehicles.

7.2 Quadrotor modelling and experimental methods

For a comprehensive study of quadrotor forward flight performance, a holistic model is required, that considers rotor aerodynamics in combination with fuselage aerodynamics and has at least a 1st order model for the key characteristics of the electric power systems

- A low order numerical blade element model using nonlinear 2-d airfoil data, a local-differential inflow model and a hingeless flapping model offers an acceptable agreement with the six-components of rotor forces/moments measured on a hingeless quadrotor rotor operating at flight conditions of practical interest; The method is

however limited in accuracy for very high local blade angles of attack and appears to offer a poor representation of the breakdown between the moments induced from lateral/longitudinal flapping.

- The addition of a multi-step over-relaxation matrix to the blade element method can provide an improvement by stabilising the iteration scheme over the advance ratio range of practical interest.

- Square-cube scaling laws increase the importance of fuselage aerodynamics for small vehicles. Fuselage aerodynamics have to be considered for forward flight and approximate models based on sine and cosine functions can successfully capture the important physics.

- The electric motors can be a source of significant losses, but their key characteristics can be captured by well-known first order models.

- The measured rotor-rotor interference for typical rotor spacings appears small and supports the current practice of ignoring rotor-rotor interference in quadrotor models

- The combination of aerodynamics and electrical systems modelling are transferable to other electric powered rotorcraft vehicles.

A wind tunnel method based on using a force-sensor feedback and trim loop provides a controlled environment for the study of quadrotor level flight which is an alternative to quadrotor flight tests.

- For outdoor test flights the ambient wind can be significant compared to the rotors' induced velocity whilst indoor tests can suffer from space restrictions hindering the exploration of the full flight envelope. For both the absolute airspeed and attitude have to be known and controlled precisely.

- A wind-tunnel based force-sensor feedback and trim loop has been successfully used to rapidly obtain steady state trim conditions and power curves for various

configurations; The method adds fidelity to experiments because it captures effects that cannot be replicated by isolated single rotor tests, such as fuselage aerodynamics and rotor-rotor interference.

7.3 Quadrotor forward flight performance and configuration

Previously, little work has been published on quadrotor forward flight performance and configuration design for forward flight. The present work makes a contribution to understanding the performance of current designs and the effects of configuration design on forward flight.

Quadrotor maximum flight speed can be limited by different mechanisms than on conventional helicopters.

- Experiments and simulations show that the airframe parasite power becomes the dominant power for quadrotors in high-speed flight, which is similar to conventional helicopters; Current quadrotor fuselages can, however, also experience a substantial amount of downforce in forward flight which requires additional power to overcome and restricts the maximum flight speed.

- As a result of large Drag/Weight ratios very large negative vehicle angles of attack are needed for forward flight trim. This leads to a steep rise in power due to increases in propulsive and induced power and restricts maximum flight speed.

- The maximum flight speed of current quadrotors is often restricted by a pitching moment trim limit before the total vehicle installed power has been reached: This limit arises as differential front/rear rotor thrust is needed to compensate the nose-up pitching moment which is primarily driven from hingeless flapping.

An x-configuration is favourable.

- For a given rotor-hub-CG spacing and motor system an x-configuration increases the available pitch and roll control authority compared to a +-configuration by over 40% and contributes towards equalising rotor loading and increasing maximum speed.

Endurance and range can be significantly improved by operational procedures

- The combined total power curve for quadrotors is similar to conventional helicopters and can exhibit a clear u-shaped profile with a minimum power and maximum range speed.

- The endurance of quadrotors can be significantly improved by simple operational procedures such as loitering at minimum power speed rather than hover and cruising at maximum range speed. This has not been considered in quadrotor literature and procedures for autonomous quadrotor operations.

To decrease power requirements, the fuselage aerodynamics should be optimized for the large negative vehicle angles of attack at high speed.

- A rotor-fuselage angle matched to the maximum vehicle angle of attack is highly effective at reducing power and increasing flight speed of conventional quadrotor fuselages; up to 20% power savings are predicted for an un-optimized research quadrotor near maximum speed.

- Endurance is mass driven at low speed and drag driven at high speed: External payloads for high speed missions should hence be optimised for drag rather than weight.

- An ideal quadrotor fuselage has minimum drag and downforce at the large negative fuselage angles of attack near maximum speed. It should contribute to achieving zero

net pitching moments about the CG to delay the onset of a trim saturation about the pitch axis.

Maximum flight speed can be increased by about 10% if the net pitching moment is minimised.

- Teetering rotors appear promising, as they do not allow a flapping-induced pitching moment to be transferred to the hub.

- A high CG above the fuselage centre of pressure and the rotor plane leads to a nose-down pitching moment from body and rotor drag that can be used to counteract the nose-up rotor pitching moment from hingeless rotors.

7.4 Evaluation of collective pitch quadrotors

Virtually all currently existing quadrotor designs use fixed-pitch rotors. **It is not expected that collective pitch will be required for small quadrotors, near-hover operations and non-gusty environments. However, collective pitch can enable the design of larger vehicles and add system level benefits and high speed power savings for applications in which the focus is on forward flight performance and manoeuvrability.**

- Introducing collective pitch adds complexity and a mass penalty, which was estimated to be about 5% of the take-off weight based on current commercial off-the-shelf components.

- Collective pitch increases control authority, allows setting collective pitch angles to reduce the thrust variation with airspeed and allows the realization of larger quadrotors, because it overcomes the reduced control response time of larger variable-speed rotors with larger inertia.

- The case study results in this thesis show that introducing collective pitch capabilities brings theoretical improvements in maximum flight speed of about 5% and reduces

power demand for most of the flight envelope, especially at high speed, where savings of about 14% were predicted for the case study vehicle

- The full benefits can only be realised if both, global collective pitch and individual rotor rotational speed, are tuned to the combination that gives minimum electric power at the given flight speed. There is little additional power benefit in using separate front/rear rotor power optimisations for the collective pitch and rpm.

- The mass penalties associated with introducing collective pitch cause a power penalty in hover and could outweigh most power benefits, expect for flight speeds within 80% of the top-speed. From 80-100% of the maximum speed, significant net power savings of up to 13% appear possible making the collective pitch an attractive design choice for high speed applications.

7.5 Recommendations for further research

- Inclusion of dynamic higher-order inflow models and an extended aeroelastic model into the blade element aerodynamics code to improve the quality of predictions at more extreme flight cases and in manoeuvres.

- Shape optimisation of quadrotor airframes to reduce the body drag and downforce, based on the suggestions made in this thesis.

- Further research into quadrotor acoustics – during an experiment an audible difference in noise level was experienced with changes in rotor spacing and collective pitch, but due to time and equipment constraints this could not be measured reliably – yet acoustics could play a dominate role in the observability of quadrotors in urban operations.

- Development of a dynamic model for the rotor behaviour, including structural dynamics and actuator dynamics to study ways to increase control bandwidth

References

1. Samad, T., *Network-centric systems for military operations in urban terrain: the role of UAVs.* Proceedings of the IEEE, 2007. **95**(1): p. 92.

2. Leishman, J.G., *Principles of Helicopter Aerodynamics 2nd edition*. 2006, Cambridge: Cambridge Aerospace Series.

3. Hoffmann, G., *Autonomy for sensor-rich vehicles: Interaction between sensing and control actions*. 2008, PhD thesis, Stanford University: Palo Alto.

4. Cowling, I.D., *Towards Autonomy of a Quadrotor UAV*, in *School of Engineering*. 2008, PhD thesis, Cranfield University.

5. Bresciani, T., *Modelling, Identification and Control of a Quadrotor Helicopter*, Master thesis, in *Department of Automatic Control* 2008, Lund University: Lund.

6. Prouty, R.W., *Helicopter Performance, Stability and Control*. 1990, Malabar: Krieger Publisihing Company.

7. Padfield, G.D., *Helicopter Flight Dynamics*. 1996, Oxford: Blackwell.

8. Filippone, A., *Flight Performance of Fixed and Rotary Wing Aircraft*. AIAA Educational Series, ed. J.A. Schetz. 2006, Oxford: AIAA.

9. Johnson, W., *Helicopter Theory*. Dover edition ed. 1994, Mineola: Dover Publications.

10. Bramwell, A.R.S., Done, G., Balmford, D., *Bramwell's Helicopter Dynamics*. 2nd edition ed. 2001, Oxford: Butterworth-Heinemann.

11. Newman, S., *The Foundations of Helicopter Flight*. 1994, London: Halsted Press.

12. Cooke, A.K., Fitzpatrick, E.W.H, *Helicopter test and evaluation*. 2002, Oxford: Blackwell Science.

13. Kroo, I., Prinz, F., et al. , *The Mesicopter: A Miniature Rotorcraft Concept - Phase II Interim Report*. 2000, Stanford University: Stanford.

14. Pounds, P., *Design, Construction and Control of a Large Quadrotor Micro Air Vehicle*. 2007, PhD thesis, Australian National University: Canberra.

15. Hoffmann, G., Huang, H., Waslander, S.L., Tomlin, C.J., *Precision flight control for a multi-vehicle quadrotor helicopter testbed.* Control Engineering Practice, 2011. **19**: p. 1023-1036.

16. Hoffmann, G.M., Huang, H., Waslander, S.L. ,Tomlin, C.J., *Quadrotor Helicopter Flight Dynamics and Control: Theory and Experiment*, in *AIAA Guidance, Navigation and Control Conference and Exhibit, 20-23 August 2007*. 2007, AIAA: Hilton Head, South Carolina.

17. Waslander, S., Hoffmann, G., Jang, J.S., Tomlin C. J., *Multi-Agent Quadrotor Testbed Control Design: Integral Sliding Mode. vs Reinforced Learning*, in *2005 IEEE/RSJ International Conference on Intelligent Robots and Systems*. 2005, IEEE.

18. Valavanis, K.P., *Advances in Unmanned Aerial Vehicles: State of the Art and the Road to Autonomy*. 2007: Springer.

19. Bouabdallah, S., P. Murrieri, and R. Siegwart, *Towards autonomous indoor micro VTOL.* Autonomous Robots, 2005. **18**(2): p. 171-183.

20. Fay, G., *Derivation of the Aerodynamic Forces for Mesicopter Simulations - unpublished paper*. 2001, Stanford

21. Martinez, V.M., *Modelling of the Flight Dynamics of a Quadrotor Helicopter*, Master thesis, in *School of Engineering - Department of Aerospace Science*. 2007, Cranfield University. p. 289.

22. Pounds, P., Mahony, R., *Design Principles of Large Quadrotors for Practical Applications*, in *IEEE International Conference on Robotics and Automation*. 2009: Kobe.

23. Pounds, P., Mahony, R., Corke, P.I., *Design of a Static Thruster for Microair Vehicle Rotorcraft.* Journal of Aerospace Engineering, 2009. **22**(1): p. 85-94.

24. Stepaniak, M.J., *A Quadrotor Sensor Platform*, PhD thesis, in *Russ College of Engineering and Technology*. 2008, Ohio University.

25. Stepaniak, M.J., van Graas, F., de Haag, M.U., *Design of an Electric Propulsion System for a Quadrotor Unmanned Aerial Vehicle.* Journal of Aircraft, 2009. **46**(3): p. 1050-1058.

26. Rong, P., Pedram, M., *An Analytical Model for Predicting the Remaining Battery Capacity of Lithium-Ion Batteries.* IEEE TRANSACTIONS ON VERY LARGE SCALE INTEGRATION (VLSI) SYSTEMS, 2006. **14**(5): p. 441-451.

27. Sudiyanto, T., Muljowidodo, *First Principle Approach to Modeling of Primitive Quad Rotor.* International Journal of Aeronautical & Space Science, 2009. **10**(2): p. 148-160.

28. Bristeau, P., Martin, P., Salauen, E., Petit, N., *The Role of Propeller Aerodynamics in the Model of a Quadrotor UAV*, in *Proceedings of the European Control Conference 2009*. 2009: Budapest.

29. Berry, A.J., *Continuous Local Motion Planning & Control for Unmanned Vehicle Operation within Complex Obstacle-Rich Environments* 2010, PhD thesis, University of Leicester Leicester

30. Bluteau, B., Briand, R.,Patrouix, O., *Design and Control of an Outdoor Autonomous Quadrotor powered by a four strokes RC engine* in *32nd Annual Conference on Industrial Electronics, IECON 2006*. 2006, IEEE: Paris.

31. Cutler, M., Ure, N., Michini, B., How,J. P., *Comparison of Fixed and Variable Pitch Actuators for Agile Quadrotors*, in *AIAA Guidance, Navigation, and Control Conference (GNC)*. 2011, AIAA: Portland.

32. Langkamp, D., Roberts, G. , Scillitoe, A. , Lunnon, I., Llopis-Pascual, A., Zamecnik, J., Proctor, S., Rodriguez-Frias, M., Turner, M. , Lanzon, A., Crowther, W.J, *An engineering development of a novel hexrotor vehicle for 3D applications*, in *IMAV 2011*. 2011: t'Harde.

33. Borenstein, J., *The Hoverbot, An Electrically Powered Flying Robot - unpublished paper*. 1992, The University of Michigan: Ann Arbor.

34. Roberts, J.F., Zufferey, J.-C., Floreano, D., *Energy management for indoor hovering robots* in *International Conference on Intelligent Robots and Systems, 2008. IROS 2008*. 2008, IEEE/RSJ Nice.

35. Althoff, S.L., Noonan, K.W., *Effect of Blade Planform Variation on a Small-Scale Hovering Rotor*, in *NASA Technical Memorandum 4146*. 1990, NASA.

36. Caradonna, F.X., Tung, C., *Experimental and Analytical Studies of a Model Helicopter Rotor in Hover*. in *NASA Technical Memorandum 81232*, 1981, NASA.

37. Meyer, J.R., Falabella, G., *An investigation of the experimental aerodynamic loading on a model helicopter rotor blade*. in *NACA TN 2953*, 1953, NACA.

38. Bohorquez, F., *Rotor Hover Performance and System Design of an Efficient Coaxial Rotary Wing Micro Air Vehicle*, PhD thesis, in *Deparment of Aerospace Engineering*. 2007, University of Maryland.

39. Young, L.A., Aiken, E.W., Johnson, J.L., Demblewski, R., Andrews, J., Klem, J. , *New Concepts and Perspectives on Micro-Rotorcraft and Small Autonomous Rotary-Wing Vehicles*, in *20th AIAA Applied Aerodynamics Conference*. 2002, AIAA: St. Louis.

40. Bermes, C., *Design and dynamic modeling of autonomous coaxial micro helicopters*. PhD thesis, 2010, ETH Zuerich: Zuerich.

41. Schafroth, D.M., *Aerodynamics, Modeling and Control of an Autonomous Micro Helicopter*. PhD thesis, 2010, ETH Zuerich: Zuerich.

42. Prior, S.D., Shen, S-T., Karamanoglu, M., Odedra, S., Erbil, M.A., Barlow, C., Lewis, D. *The Future of Battlefield Micro Air Vehicle Systems* in *Proceedings of the International*

Conference on Manufacturing Engineering Systems. 2009. National Formosa University, Huwei, Yunlin, Taiwan.

43. Bouabdallah, S., *Design and control of quadrotors with application to autonomous flying.* PhD thesis, 2007, ETH Zurich: Zurich.

44. *Capability Challenges Document*. January 2010, SEAS DTC.

45. Mettler, B., *Identification, Modeling and Characteristics of Miniature Rotorcraft*. 2003, Norwell: Kluwer Academic Publishers.

46. Gavrilets, V., *Autonomous Aerobatic Maneuvering of Miniature Helicopters*. PhD thesis, 2003, Massachusetts Institute of Technology: Boston.

47. Drela, M., *XFOIL: An Analysis and Design System for Low Reynolds Number Airfoils*, in *Low Reynolds Number Aerodynamics - Lec. Notes in Eng. 54*. 1989, Springer.

48. Oliveira, R. *XFOIL Matlab Interface*. 2001 01/07/2011]; Available from: http://www.mathworks.com/matlabcentral/fileexchange/30478-xfoil-matlab-interface.

49. Sheldahl, R.E., Klimas, P.C., *Aerodynamic Characteristics of Seven Symmetrical Airfoil Sections Through 180-Degree Angle of Attack for Use in Aerodynamic Analysis of Vertical Axis Wind Turbines*, in *Sandia National Laboratories energy reports*, Sandia National Laboratories: Albuquerque.

50. Filippone, A., *Airfoil inverse design and optimization by means of viscous-inviscid techniques.* Journal of Wind Engineering and Industrial Aerodynamics, 1995. **56**: p. 123-126.

51. Fuglsang, P., Antoniou, I., Sørensen, N.N., Madsen, H.A., *Validation of a Wind Tunnel Testing Facility for Blade Surface Pressure Measurements*. Risø-R-981(EN), 1998, Risø National Laboratory: Roskilde.

52. Johnson, W., *Comparison of Calculated and Measured Helicopter Rotor Lateral Flapping Angles*, in *NASA Technical Memorandum 81213*. 1980, Ames Research Centre: Moffett Field.

53. Young, M.I., *A simplified theory of hingeless rotors with application to tandem helicopters*, in *Proceedings of the 18th Annual National Forum of the AHS*. 1962, American Helicopter Society.

54. Chen, R.T.N., *A Survey of Nonuniform Inflow Models for Rotorcraft Flight Dynamics and Control Applications*, in *NASA Technical Memorandum 102219*. 1989, Ames Research Centre.

55. MathWorld, W. *Successive Overrelaxation Method*. 2011 10/10/2011]; Available from: http://mathworld.wolfram.com/SuccessiveOverrelaxationMethod.html.

56. Chen, R.T., Hindson,W.S., *Influence of Dynamic Inflow on the Helicopter Vertical Response*. in *NASA Technical Memorandum 88327*, 1986, NASA: Moffett Field.

57. Moriarty, P.J., Hansen, A.C., *AeroDyn Theory Manual*. 2005, National Renewable Energy Laboratory: Colorado.

58. Drela, M., *First-Order DC Electric Motor Model*, in *Qprop Manual*. 2007, MIT: Boston.

59. Langkamp, D., Crowther W., *Simulation methods for MAVs in Urban Operations* in *4th International UAV World Conference 2010* 2010, Airtec: Frankfurt.

60. MathWorks. *Product Documentation: Battery*. 2011 01/08/2011]; Available from: http://www.mathworks.co.uk/help/toolbox/physmod/powersys/ref/battery.html.

61. Potts, J., *Disc-Wing Aerodynamics*, in *School of Mechanical and Aerospace Engineering*. PhD thesis, 2005, University of Manchester: Manchester.

62. Dingeldein, R.C., *Wind-tunnel studies of the performance of multirotor configurations*, in *NACA Technical Note 3236*. 1954: Langley Field.

63. Halliday, A.S., Cox, D.K., *Wind Tunnel Experiments on a Model of a Tandem Rotor Helicopter*, in *ARC Technical Report C.P. No. 517*. 1961: London.

64. Barlow, J.B., Rae, W.H., Pope, A., *Low speed wind tunnel testing - 3rd edition*. 1999, New York: Wiley-Interscience.

65. Sumathi, S., Surekha, P., *LabView based Advanced Instrumentation Systems*. 2007, Berlin: Springer.

66. Langer, H., Peterson, R.L., Maier, T.H., *An experimental evaluation of wind tunnel wall correction methods for helicopter performance*, in *52nd Annual Forum of the American Helicopter Society*. 1996, AHS: Washington.

67. Theodorsen, T., Silverstein, A., *Experimental verification of the theory of wind-tunnel boundary interference*,in *Report No 478*, 1935, NACA.

68. Holeman, J.P., *Experimental Methods for Engineers*. 2007: McGraw-Hill.

69. Petricca, L., Ohlckers, P., Grinde, C., *Micro- and Nano-Air Vehicles: State of the Art.* International Journal of Aerospace Engineering, 2011. **2011**: p. 17.

70. Johnson, W., *Model for Vortex Ring State Influence on Rotorcraft Flight Dynamics*. in *NASA/TP-2005-213477*, 2005, Ames Research Centre: Moffett Field.

71. Griffiths, D.A., Leishman, J.G., *A Study of Dual-Rotor Interference and Ground Effect Using a Free-Vortex Wake Model*, in *58th Annual Forum of the American Helicopter Society*. 2002, AHS: Montreal.

72. Heyson, H.H., *Preliminary results from flow-field measurements around singel and tandem rotors in the Langley full-scale tunnel*, in *NACA Technical Note 3242*. 1954, NACA: Langley Field.

73. Pounds, P., Mahony, R., Corke, P.I., *Modelling and control of a large quadrotor robot.* Control Engineering Practice, 2010. **18**: p. 691-699.

Appendix 1: Mangler-Squire coefficients [Leishman]

The following equations and formulations were taken from Leishman [2]

The coefficients for the Mangler & Squire Fourier transform can be used as:

The variable v is introduced as: $v^2 = 1 - r^2$

For Type 1 loading:

$$c_0 = \frac{3}{4}v$$

$$c_1 = -\frac{3\pi}{16}\sqrt{1-v^2}\sqrt{\frac{1-\sin\alpha}{1+\sin\alpha}}$$

For even values of n:

$$c_n = (-1)^{\frac{n-2}{n}}\left(\frac{3}{4}\right)\left(\frac{v+n}{n^2-1}\right)\left(\frac{1-v}{1+v}\right)^{\frac{n}{2}}\left(\frac{1-\sin\alpha}{1+\sin\alpha}\right)^{\frac{n}{2}}$$

For odd values of $n \geq 3$ c is assumed to be 0.

For Type 3 loading:

$$c_0 = \frac{15}{8}v(1-v^2)$$

$$c_1 = -\frac{15\pi}{256}(5-9v^2)\sqrt{1-v^2}\sqrt{\frac{1-\sin\alpha}{1+\sin\alpha}}$$

$$c_3 = \frac{45\pi}{256}(1-v^2)^{1.5}\left(\frac{1-\sin\alpha}{1+\sin\alpha}\right)^{1.5}$$

For even values of n:

$$c_n = (-1)^{\frac{n-2}{n}}\left(\frac{15}{8}\right)\left[\left(\frac{v+n}{n^2-1}\right)\left(\frac{9n^2+n^2-6}{n^2-9}\right)+\left(\frac{3v}{n^2-9}\right)\right]\left(\frac{1-v}{1+v}\right)^{\frac{n}{2}}\left(\frac{1-\sin\alpha}{1+\sin\alpha}\right)^{\frac{n}{2}}$$

For odd values of $n \geq 5$ c is assumed to be 0.